CFDRC
Better Decisions, Better Products
Through Simulation & Innovation

COMBUSTION LES SOFTWARE FOR IMPROVED EMISSIONS PREDICTIONS OF HIGH PERFORMANCE GAS TURBINE COMBUSTORS

Final Report

by
David Lee Black
Karl V. Meredith
Sachin Khosla
Sarma L. Rani
Clifford E. Smith

DISTRIBUTION STATEMENT A
Approved for Public Release
Distribution Unlimited

CFD Research Corporation
215 Wynn Drive, Suite 501
Huntsville, AL 35805

September 2005 **CFDRC Project No.: 8503/8**

submitted to
NAWCAD
22195 Elmer Road
Unit 4, Bldg. 106
Patuxent River, MD 20670

Technical Monitors: Dr. John Spyropoulos – AIR 4.4.7.1
Contract Administrator: Ms. Angela Munro

Contract Number: N00421-04-C-0002

CLIN A001

TABLE OF CONTENTS

Page

LIST OF FIGURES ii

LIST OF TABLES vii

ABSTRACT 1

EXECUTIVE SUMMARY 2

1. INTRODUCTION 3

2. TECHNICAL OBJECTIVES 8

3. RESULTS 8

3.1 Improvements to Existing LES Models 9
3.2 Multi-Step PDF Turbulent Combustion Model 23
3.3 Improved LES Inflow Boundary Conditions 29
3.4 Global Mechanism Generation 35
3.5 Initial Code Validation 50
3.6 Final Code Validation 62
3.7 JSF Combustor Simulations 112

4. CONCLUSIONS 112

5. REFERENCES 114

LIST OF FIGURES

Page

Figure 1. LES and RANS Predictions of Velocity Magnitude at High Power Conditions 4
Figure 2. LES and RANS Predictions of Temperature and Spray Trajectories at High Power Conditions 4
Figure 3. Comparison of NO_x Predictions for LES and RANS at High Power Conditions 5
Figure 4. Comparison of CO Emissions Predictions for LES and RANS at Low Power Conditions 7
Figure 5. Predictions of Temperature and Variance in a Lean Premixed Bluff-Body Combustor Using Assumed PDF Model with LES 16
Figure 6. Baseline Geometry for SimVal Combustor 18
Figure 7. SimVal Geometry for Baseline Case 18
Figure 8. 3D LES Snapshot of Filtered NO_x Source Term and Vorticity Magnitude (ϕ=0.7) 19
Figure 9. Reaction Progress with the LDVM Model 20
Figure 10. Reaction Progress Variance with the LDVM Model 20
Figure 11. Temperature Plotted at a Reaction Progress of 0.9 21
Figure 12. Snapshots of Temperature Contours in the SimVal Combustor 22
Figure 13. Snapshots of NO_x Contours in the SimVal Combustor 22
Figure 14. Equilibrium Concentrations Versus Instantaneous Concentrations as a Function of Reaction Progress 25
Figure 15. Geometry and Grid for Channel Flow Between Two Parallel Plates 30
Figure 16. Turbulent Flow Structures for Axial Velocity in Channel Flow Between Two Parallel Plates Utilizing Periodic Inlet-Outlet Boundary Conditions 30
Figure 17. Inlet Axial-Velocity Profiles for Periodic Inlet-Outlet Simulation of Flow Between Two Parallel Plates 30
Figure 18. Inlet Axial-Velocity Profiles Showing Spatial Correlation for the Gaussian Random and SCI Boundaries 32
Figure 19. Turbulent Flow Structures for Axial Velocity in Channel Flow Between Two Parallel Plates Utilizing a Gaussian Random Method for Generation of Inflow Boundary Condition Data 33
Figure 20. Turbulent Flow Structures for Axial Velocity in Channel Flow Between Two Parallel Plates Utilizing an Auxiliary Upstream Solution for Generation of Inflow Boundary Condition Data 35
Figure 21. Flow Chart of the Process Used to Automatically Generate Reduced Global Mechanisms from Detailed Mechanisms 37
Figure 22. Diagram of PSR-PFR Combination Used in Chemical Reactor Modeling 37
Figure 23. Comparisons of Predictions in Net Species Productions for Detailed and Global Mechanisms 40
Figure 24. Comparison of Temperature and Species Profiles Computed via Global and Detailed Mechanisms for ϕ=0.6, T_{in}=600 K, P=1 atm, and a PSR Residence Time of 0.1 msec 40
Figure 25. Comparison of Species Profiles Computed via Global and Detailed Mechanisms for ϕ=0.6, T_{in}=600K, P=1 atm, and a PSR Residence Time of 0.1 msec 41
Figure 26. Species Net Production Comparisons for Detailed and Global Mechanism (Mechanism 1) Calculations 42

Figure 27. Species Net Production Comparisons for Detailed and Global Mechanism (Mechanism 2) Calculations 43
Figure 28. (a) Temperature and (b) Species Plots Showing Comparisons Between Detailed and Global Calculations 45
Figure 29. (a) Temperature and (b) Species Plots Showing Comparisons Between Detailed and Global Calculations 46
Figure 30. Schematic Of Opposed Diffusion Flame Configuration 46
Figure 31. Temperature Profile For 1-D Opposing Diffusion Flame Using Fitted Global Rate Parameters Compared To The Detailed GRI-3.0 Mechanism Temperature Profile 48
Figure 32. Species Profiles Of CH_4, O_2, And N_2 For 1-D Opposing Diffusion Flame Using Fitted Global Rate Parameters Compared To The Detailed GRI-3.0 Mechanism Species Profiles 48
Figure 33. Species Profiles Of CO, H_2O, And CO_2 For 1-D Opposing Diffusion Flame Using Fitted Global Rate Parameters Compared To The Detailed GRI-3.0 Mechanism Species Profiles 49
Figure 34. Species Profiles Of CO, H_2O, and CO_2 for 1-D Opposing Diffusion Flame Using Fitted Global Rate Parameters Compared to the Detailed GRI-3.0 Mechanism Species Profiles 50
Figure 35. Calculated Axial Velocity Distribution for Flame L 52
Figure 36. Calculated Flame Temperature Distribution for Flame L 52
Figure 37. Results for Diffusion Flame K with an Inlet Axial Velocity of 27m/s at an x/d = 20 53
Figure 38. Results for Diffusion Flame K with an Axial Inlet Velocity of 27m/s at an x/d = 50 54
Figure 39. Results for Diffusion Flame L with an Axial Inlet Velocity of 41m/s at an x/d = 20 55
Figure 40. Results for Diffusion Flame L with an Axial Inlet Velocity of 41m/s at an x/d = 50 56
Figure 41. Results for Diffusion Flame M with an Axial Inlet Velocity of 55m/s at an x/d = 20 57
Figure 42. Results for Diffusion Flame M with an Axial Inlet Velocity of 55m/s at an x/d = 50 58
Figure 43. Flame Front (Progress Variance) 59
Figure 44. Calculated Distributions of Temperature, CO, and CO_2 Mass Fraction 60
Figure 45. Comparison of Fuel Concentration Profile Normalized by N_2 Concentration 61
Figure 46. Comparison of the Flame Temperature Profile 62
Figure 47. Schematic and Turbulent Flame Structure of Bluff-Body-Stabilized Lean Premixed Combustor (Nandula et al., 1996) 63
Figure 48. Structured Grids for 3D Combustor Geometry 64
Figure 49. RANS Simulation Results Prior to Blowout Showing the Extinguishing of the Flame Downstream of the Bluff Body 65
Figure 50. Snapshot of Temperature in the Nandula Bluff-Body Combustor LES Simulation Using Multi-Step Chemistry 65
Figure 51. Snapshot of Axial Velocity in the Nandula Bluff-Body Combustor LES Simulation Using Multi-Step Chemistry 66

Figure 52. Snapshot of CO Mass Fraction in the Nandula Bluff-Body Combustor LES Simulation Using Multi-Step Chemistry 66
Figure 53. Plots of Instantaneous LES Results Compared to the Averaged Measured Data for CO, T, CO_2, and H_2O Downstream of the Bluff Body at an x/d of 0.1 67
Figure 54. Plots of Instantaneous LES Results Compared to the Averaged Measured Data for CO, T, CO_2, and H_2O Downstream of the Bluff Body at an x/d of 0.6 68
Figure 55. Plots of Instantaneous LES Results Compared to the Averaged Measured Data for CO, T, CO_2, and H_2O Downstream of the Bluff Body at an x/d of 1.0 69
Figure 56. SMA2 Burner Schematic 70
Figure 57. The SMA2 Flame 71
Figure 58. 2D Axi-Symmetric Grid for Non-Reacting SMA2 Case 72
Figure 59. Axial and Tangential Velocity Comparisons Between Experimental and 2D Axi-Symmetric CFD Results at 6.8 mm Downstream of Burner Exit 72
Figure 60. 3D RANS Grid, (a) Top Left: Front View, (b) Top Right: Close-Up of Front View and (c) Bottom: Side View 73
Figure 61. RANS Cold-Flow Axial Velocity 73
Figure 62. Axial and Tangential Velocity Comparisons Between Experimental and 3D CFD RANS Results at 6.8 mm Downstream of Burner Exit 74
Figure 63. Axial and Tangential Velocity Comparisons Between Experimental and 3D CFD RANS Results at 30.0 mm Downstream of Burner Exit 74
Figure 64. Axial and Tangential Velocity Comparisons Between Experimental and 3D CFD RANS Results at 100.0 mm Downstream of Burner Exit 74
Figure 65. RANS Axial Velocity – Reacting Flow 75
Figure 66. RANS Temperature – Reacting Flow 75
Figure 67. Axial and Tangential Velocity Comparisons (Top) and Temperature Comparisons (Bottom) Between Experimental and 3D CFD Results at 10.0 mm Downstream of Burner Exit 76
Figure 68. Axial and Tangential Velocity Comparisons (Top) and Temperature Comparisons (Bottom) Between Experimental and 3D CFD Results at 30.0 mm Downstream of Burner Exit 77
Figure 69. Axial and Tangential Velocity Comparisons (Top) and Temperature Comparisons (Bottom) Between Experimental and 3D CFD Results at 100.0 mm Downstream of Burner Exit 77
Figure 70. Snapshot of Temperature for the LES SMA2 Case 78
Figure 71. Axial Velocity (Top Left), Tangential Velocity (Top Right), CO_2 Mass Fraction (Bottom Left) and Temperature (Bottom Right) Comparisons Between Experimental and 3D CFD Results at 10.0 mm Downstream of Burner Exit 79
Figure 72. Axial Velocity (Top Left), Tangential Velocity (Top Right), CO_2 Mass Fraction (Bottom Left) and Temperature (Bottom Right) Comparisons Between Experimental and 3D CFD Results at 10.0 mm Downstream of Burner Exit 80
Figure 73. SMA2 Flame Axial (u-) Velocity Comparisons at Various Axial (x-) Locations Downstream of the Burner (a) x = 6.8mm (b) x = 30mm (c) = 100mm 81
Figure 74. SMA2 Flame Tangential (w-) Velocity Comparisons at Various Axial (x-) Locations Downstream of the Burner (a) x = 6.8mm (b) x = 30mm (c) = 100mm 82
Figure 75. SMA2 Flame Temperature Comparisons at Various Axial (x-) Locations Downstream of the Burner. (a) x = 10mm (b) x = 30mm (c) = 100mm 83

Figure 76. SMA2 Flame CO Mass Fraction Comparisons at Various Axial (x-) Locations Downstream of the Burner (a) x = 10mm (b) x = 30mm (c) = 100mm 84
Figure 77. SMA2 Flame CO_2 Mass Fraction Comparisons at Various Axial (x-) Locations Downstream of the Burner (a) x = 10mm (b) x = 30mm (c) = 100mm 85
Figure 78. The Sandia-D Flame 86
Figure 79. 3D RANS Grid, (a) Top Left: Front View, (b) Top Right: Close-Up of Front View and (c) Bottom: Side View 87
Figure 80. RANS Axial Velocity – Reacting Flow 88
Figure 81. RANS Temperature – Reacting Flow 88
Figure 82. Axial Velocity (Top Left), Temperature (Top Right), CH_4 Mass Fraction (Bottom Left) and CO Mass Fraction (Bottom Right) Comparisons Between Experimental and 3D CFD Results at x/d = 1 Downstream of Burner Exit 89
Figure 83. Axial Velocity (Top Left), Temperature (Top Right), CH_4 Mass Fraction (Bottom Left) and CO Mass Fraction (Bottom Right) Comparisons Between Experimental and 3D CFD Results at x/d = 3 Downstream of Burner Exit 90
Figure 84. Axial Velocity (Top Left), Temperature (Top Right), CH_4 Mass Fraction (Bottom Left) and CO Mass Fraction (Bottom Right) Comparisons Between Experimental and 3D CFD Results at x/d = 15 Downstream of Burner Exit 91
Figure 85. Axial Velocity (Top Left), Temperature (Top Right), and CO Mass Fraction (Bottom) Comparisons Between Experimental and 3D CFD Results at x/d = 30 Downstream of Burner Exit 92
Figure 86. Axial Velocity (Top Left), Temperature (Top Right), and CO Mass Fraction (Bottom) Comparisons Between Experimental and 3D CFD Results at x/d = 45 Downstream of Burner Exit 93
Figure 87. Grid for Both RANS and LES Simulations of the Sandia-D Flame 94
Figure 88. RANS Temperature Profiles for the Sandia-D Flame Using Multi-Step Chemistry 95
Figure 89. RANS Axial Velocity Profiles for the Sandia-D Flame Using Multi-Step Chemistry 95
Figure 90. RANS CO Mass Fraction Profiles for the Sandia-D Flame Using Multi-Step Chemistry 96
Figure 91. RANS CO_2 Mass Fraction Profiles for the Sandia-D Flame Using Multi-Step Chemistry 96
Figure 92. Sandia-D Flame Axial (u-) Velocity Comparisons at Various Axial (x-) Locations Downstream of the Burner (a) x/d = 1 (b) x/d = 15 (c) x/d = 30 (d) x/d = 45 97
Figure 93. Sandia-D Flame Temperature Comparisons at Various Axial (x-) Locations Downstream of the Burner. (a) x/d = 1 (b) x/d = 15 (c) x/d = 30 (d) x/d = 45 98
Figure 94. Sandia-D Flame CH_4 Mass Fraction Comparisons at Various Axial (x-) Locations Downstream of the Burner (a) x/d = 1 (b) x/d = 15 (c) x/d = 30 99
Figure 95. Sandia-D Flame CO Mass Fraction Comparisons at Various Axial (x-) Locations Downstream of the Burner (a) x/d = 1 (b) x/d = 15 (c) x/d = 30 (d) x/d = 45 100
Figure 96. Sandia-D Flame CO_2 Mass Fraction Comparisons at Various Axial (x-) Locations Downstream of the Burner (a) x/d = 1 (b) x/d = 15 (c) x/d = 30 (d) x/d = 45 101
Figure 97. Preliminary Snapshot of Temperature from the Sandia-D LES Combustor Simulations 102

Figure 98. Preliminary Snapshot of Axial Velocity from the Sandia-D LES Combustor Simulations 102
Figure 99. Preliminary Snapshot of Radial Velocity from the Sandia-D LES Combustor Simulations 103
Figure 100. Schematic of the TECFLAM Combustor (Meier et al., 2000) 103
Figure 101. TECFLAM Combustor 104
Figure 102. 3D RANS Grid, (a) Top Left: Angled View, (b) Top Right: Side View and (c) Bottom: Front View 105
Figure 103. Comparison of 3D RANS with Experimental Data at 10 mm Downstream of the Injector (a) Top Left: Axial Velocity, (b) Top Right: Tangential Velocity, (c) Bottom: Temperature 106
Figure 104. Comparison of 3D RANS with Experimental Data at 20 mm Downstream of the Injector (a) Top Left: Axial Velocity, (b) Top Right: Tangential Velocity, (c) Bottom: Temperature 106
Figure 105. Comparison of 3D RANS with Experimental Data at 30 mm Downstream of the Injector for Velocities and 40mm Downstream for Temperature, (a) Top Left: Axial Velocity, (b) Top Right: Tangential Velocity, (c) Bottom: Temperature 107
Figure 106. Comparison of 3D RANS with Experimental Data at 70 mm Downstream of the Injector for Velocities and 60mm downstream for Temperature. (a) Top Left: Axial Velocity, (b) Top Right: Tangential Velocity, (c) Bottom: Temperature 107
Figure 107. Snapshot of TECFLAM 3D Reacting Flow RANS Simulation 108
Figure 108. Comparison of 3D LES with Experimental Data at 10 mm Downstream of the Injector. (a) Top Left: Axial Velocity, (b) Top Right: Tangential Velocity, (c) Bottom: Temperature 109
Figure 109. Comparison of 3D LES with Experimental Data at 20 mm Downstream of the Injector. (a) Top Left: Axial Velocity, (b) Top Right: Tangential Velocity, (c) Bottom: Temperature 109
Figure 110. Comparison of 3D LES with Experimental Data at 30 mm Downstream of the Injector for Velocities and 40mm Downstream for Temperature. (a) Top Left: Axial Velocity, (b) Top Right: Tangential Velocity, (c) Bottom: Temperature 110
Figure 111. Comparison of 3D LES with Experimental Data at 70 mm Downstream of the Injector for Velocities and 60mm Downstream for Temperature. (a) Top Left: Axial Velocity, (b) Top Right: Tangential Velocity, (c) Bottom: Temperature 110
Figure 112. Snapshot of Initial TECFLAM 3D Reacting Flow LES Simulation 111

LIST OF TABLES

Page

Table 1. Predicted and Measured CO, NO_x, and Temperature for AE3007 High Power Conditions 6
Table 2. Predicted and Measured CO, NO_x, and Temperature for AE3007 Low Power Conditions 7
Table 3. Work Schedule 9
Table 4. The Nichol (1995) Mechanism for CH_4 36
Table 5. Optimized Arrhenius Rate Parameters for a Global 3-step Methane Oxidation Mechanism 39
Table 6. Global 5-Step Mechanism for $C_{12}H_{23}$ Combustion Using a Water-Gas Shift Reaction 41
Table 7. Global 5-Step Mechanism for $C_{12}H_{23}$ Combustion Using a CO Oxidation Step 42
Table 8. Global 3-Step Mechanism for Methane Combustion at ϕ=1.0, T=300 K, and P=1 atm 44
Table 9. Global 3-Step Mechanism for Methane Combustion at ϕ=1.0, T=300 K, and P=1 atm 45
Table 10. Intermediate Arrhenius Parameters Optimized On Species Net Production Rates 47
Table 11. Arrhenius Parameters Optimized On Temperature and Species Profiles 47
Table 12. Global Mechanism Containing 5 Steps and 7 Species that Includes NO_x Chemistry 49
Table 13. Investigated Pilot-Stabilized Diffusion Flames of CH_4 51
Table 14. Uncertainty in Chemical Species Measurements and Temperature Measurements from Nandula et al (1996) 63
Table 15. Optimized Arrhenius Rate Parameters Nandula 3-Step Methane Oxidation Mechanism (Phi = 0.586, T=300 K) 64
Table 16. SMA2 Operating Conditions 71
Table 17. Five-Step Methane Mechanism Accounting for CO and H_2 94

ABSTRACT

Low emissions of CO, NO_x, and unburned hydrocarbons (UHC) are a difficult challenge in the design of new military gas turbine combustors. Simulation tools that can predict emissions are needed to reduce the cost of producing improved, low emissions combustor designs. In this SBIR, CFD Research Corporation (CFDRC) continued to develop combustion Large Eddy Simulation (LES) techniques to create a high fidelity tool for predicting emissions. The LES code was improved by the development and implementation of a new multi-step assumed PDF method that accounts for more detailed kinetics with turbulent chemistry interactions. This new method enables efficient turbulent combustion CFD calculations for both steady state Reynolds Averaged Navier Stokes (RANS) and LES with multi-step global mechanisms. Tabulation methods were implemented and tested for improved computational efficiency. Improvements to the existing combustion models and inlet boundary conditions for LES were also performed. In addition to the new turbulent combustion models, the capability to generate the necessary global mechanisms from detailed reaction mechanisms was developed. The final code was validated against benchmark experimental data, and applied to the Rolls-Royce JSF combustor. Validation cases included both premixed and diffusion flames covering a broad range of flame conditions.

Although much progress was made in this Phase II effort, continued work is needed to make the new multi-step assumed PDF model robust and practical. In particular, a new solver for the species transport equations needs to be implemented to reduce run times by a factor of two or more.

EXECUTIVE SUMMARY

Low emissions of pollutants, including CO, NO_x, UHC, and smoke, are becoming a requirement for today's and future military gas turbine engines. Advanced, high performance gas turbines will feature higher inlet temperatures and pressures, and will require new fuel injector and combustor designs if lower emissions are to be realized. These low emissions gas turbine combustors will operate at near stoichiometric overall fuel-air ratios at full power, and will have many emission design challenges.

To meet these challenges in a cost- and time-effective manner, improved combustor design systems are needed that include accurate models of chemical kinetics, turbulent mixing, and their interaction. In this SBIR program, CFDRC continued to develop 3D combustion Large Eddy Simulation (LES) capabilities to help meet these design challenges. Newly developed capabilities for capturing turbulence-chemistry interactions with complex chemistry, improved multi-step reactions mechanisms for JP-8, and algorithms to improve computational speed greatly enhance the ability to predict emissions in high performance military combustors.

The primary focus of the program was on the development of a new multi-step, assumed PDF model for turbulent combustion. The newly developed model is generally applicable to multi-step global mechanisms and results in a minimal increase in the overall computational expense. The effect of turbulence is accounted for by integrating the instantaneous reaction rate over a PDF to get the resulting mean rates. The PDF used is based on the mixture fraction and reaction progress variables to allow for the characterization of both premixed and diffusion flames. With the two-variable PDF formulation, only two additional transport equations must be solved for, regardless of the number of species of steps in the mechanism. This capability represents a significant improvement in the state-of-the-art for practical turbulent combustion modeling.

Although the PDF model was successfully developed and tested, improvements in the solution of the transport equations will be essential for the model to find wide-spread application. The existing method for solving the species transport equations utilizes a cell-by-cell point solver. Specifically, the solver 'sweeps' over all of the computational cells in the domain solving the coupled species equations at each cell. While adequate for small problems, large problems require a large number of iterations in order to assure global convergence. Steady-state problems can usually afford a large number of global iterations to achieve ample convergence. However, transient cases such as LES need to keep the number of global iteration per time step to a minimum if practical run times are to be realized. Practical simulations will require the implementation of a "whole-field" solver for the coupled species transport equations.

In addition to the new turbulent combustion models, the ability to generated global mechanisms from detailed reaction mechanisms was also developed. Multi-step kinetics are essential to accurately capture behavior of real reactions, such as the conversion of CH_4 to CO and then to CO_2. The ability to generate these mechanisms, commonly termed Chemical Reactor Modeling (CRM), was shown to an effective method of determining global Arrhenius rate parameters. The global mechanisms generated can be fine tuned to combustor operating conditions including inlet temperature, equivalence ratio range, and operating pressure.

1. INTRODUCTION

Low emissions of pollutants, including CO, NO_x, UHC, and smoke, are becoming a requirement for today's and future military gas turbine engines. Advanced, high performance gas turbines will feature higher inlet temperatures and pressures, and will require new fuel injector and combustor designs if lower emissions are to be realized. These low emissions gas turbine combustors will operate at near stoichiometric overall fuel-air ratios at full power, and will have many emission design challenges, some of which are:

1. How to effectively dilute fuel-rich, high CO regions before the hot gas enters the turbine;
2. How to minimize residence times for high-temperature, thermal NO_x producing regions; and,
3. How to oxidize CO and reduce UHC at low power conditions.

To meet these challenges in a cost- and time-effective manner, improved combustor design systems are needed that include accurate models of chemical kinetics, turbulent mixing, and their interaction. Current steady-state RANS (Reynolds Averaged Navier Stokes) CFD combustion codes lack the quantitative accuracy needed for reliable predictions of emissions. The limitations of the current CFD codes are mainly due to deficiencies in the treatment of the turbulent fluid motion and its interaction with chemical kinetics, i.e., turbulence-combustion interaction. This is because turbulent combustion is inherently unsteady (including vortex shedding, shear layer mixing, and acoustic wave propagation), and RANS codes cannot capture counter-gradient diffusion and other unsteady phenomena seen in gas turbine combustors. The accuracy of emissions predictions is especially vulnerable to RANS limitations. In this SBIR program, CFDRC is continuing to develop 3D combustion LES capabilities to help meet these design challenges. Newly developed capabilities for capturing turbulence-chemistry interactions with complex chemistry, improved multi-step reactions mechanisms for JP-8, and algorithms to improve computational speed will greatly enhance the ability to predict emissions in high performance military combustors, including the accurate prediction of NO_x, CO, and UHC.

In Phase I, the feasibility of improved emissions predictions for CO and NO_x using combustion LES modeling of an aero gas turbine combustor was demonstrated. The combustion LES analysis utilized a local subgrid turbulent kinetic energy model (called the localized dynamic kinetic energy model, LDKM) to predict local viscosities as a function of the grid size and velocity gradients. The turbulent kinetic energy provided a source term for the subgrid turbulence-chemistry assumed PDF model. LES filtered reaction rates for the fuel, CO, and NO_x transport equations included turbulent fluctuations in the mixture fraction and reaction progress variables. A 2-step chemical reaction model that provides a finite rate of fuel oxidation to CO and then CO oxidation to equilibrium products was used. Also, a de-coupled NO_x transport method, accounting for thermal NO_x reactions, was included.

Both combustion LES and steady-state RANS calculations of the Rolls-Royce AE3007 combustor were performed. The 2.3 million cell computational domain consisted of the entire combustor internal flowfield (from the swirl vane exit planes to the combustor exit), as well as the outer annuli surrounding the combustor. Estimated flowsplits were provided by Rolls-Royce. Comparisons of predictions to available experimental data at the combustor exit plane were

made. Figures 1 and 2 show snapshots and time-averaged predictions of velocity magnitude and temperature (high-power conditions). The velocity predictions indicate stronger penetration of the primary jets using LES. This stronger penetration closes off the central recirculation zone, making it more compact for the LES predictions. The temperature predictions show the effect of stronger mixing with LES. The peak temperature is reduced using LES and the hot temperatures spread out over a greater area in the intermediate zone. This higher mixing in the intermediate zone is due to the strong primary jets that create stronger wakes and mixing behind the jets.

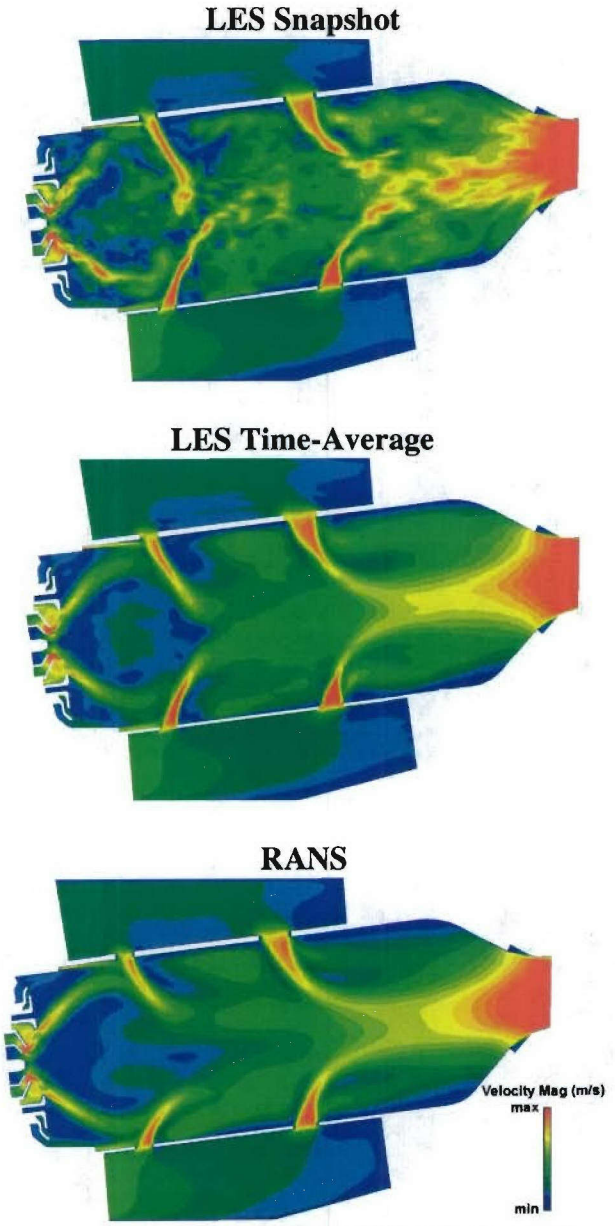

Figure 1. LES and RANS Predictions of Velocity Magnitude at High Power Conditions

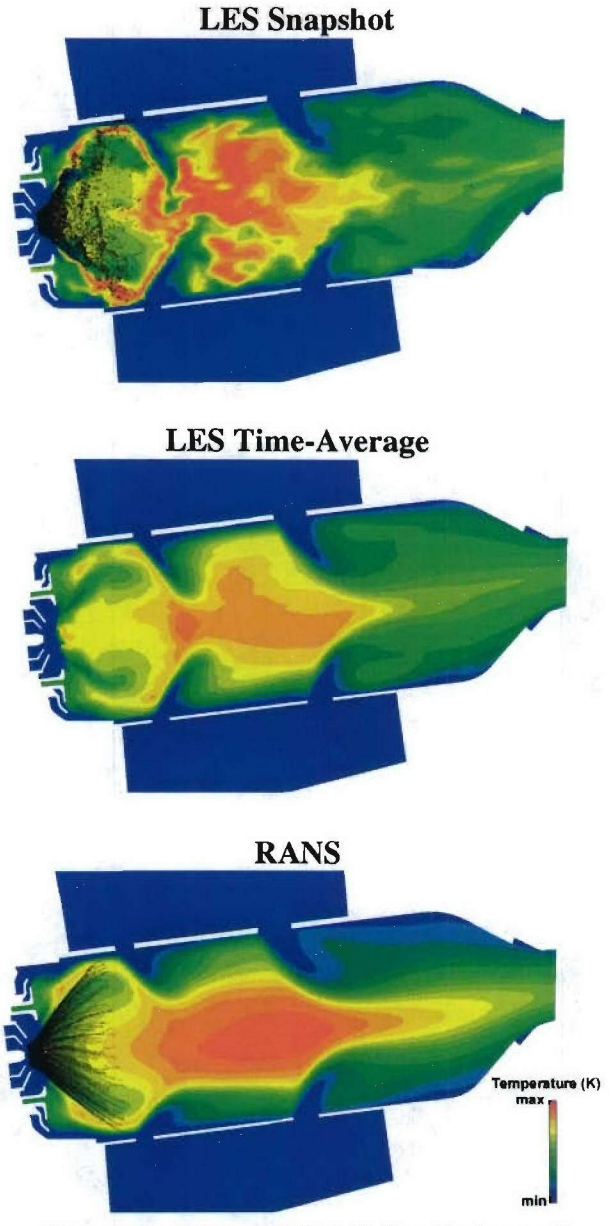

Figure 2. LES and RANS Predictions of Temperature and Spray Trajectories at High Power Conditions

Figure 3 shows the NO_x emissions predictions at high power where most NO_x is formed. NO_x is formed at high temperature locations when there is excessive oxygen, typically at local equivalence ratios around 0.8 – 0.9. The NO_x emissions results show that NO_x is formed sooner and over a larger volume for the LES, particularly out towards the inner and outer liner of the intermediate zone. However, higher peak values are predicted for the RANS along the centerline of the dilution zone, most likely due to the higher peak temperatures in this region. Overall, more NO_x is predicted for RANS at the combustor exit.

Table 1 shows comparisons of the predictions and measurements at the high power conditions. Overall, LES provides a better prediction of emissions compared to the RANS. The improved results can be largely attributed to the stronger mixing of primary and dilution air with the combustor core flow for the LES and the mixing produced by combustor unsteadiness. The RANS did not capture the higher jet penetration as observed in the LES. The CO emissions show the largest differences between the two predictions and measurements. However, the absolute magnitude of the CO is small, making quantitative predictions difficult.

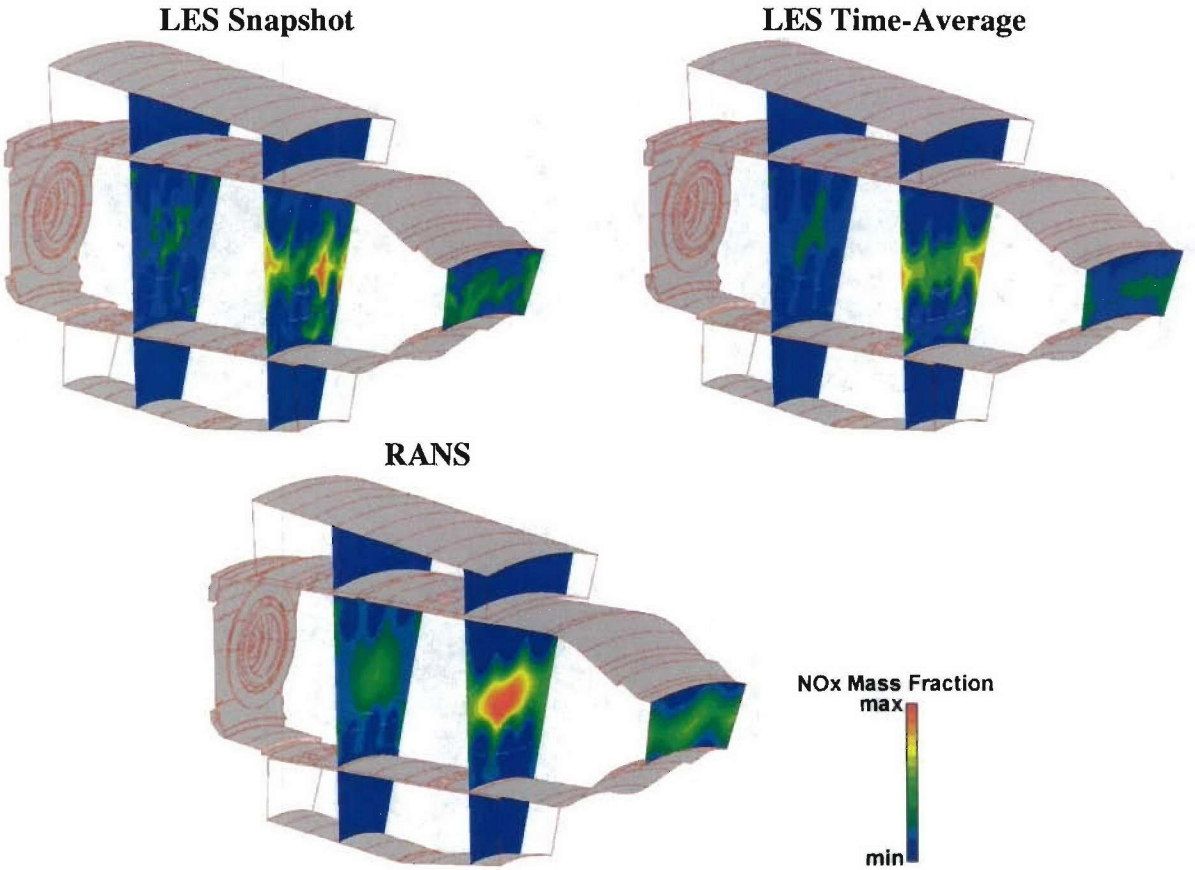

Figure 3. Comparison of NO_x Predictions for LES and RANS at High Power Conditions

Table 1. Predicted and Measured CO, NO_x, and Temperature for AE3007 High Power Conditions

	Experimental	RANS	LES
$T/T_{measured}$	1	0.98	1.00
$CO/CO_{measured}$	1	10.73	0.42
$NO_x/NO_{x,measured}$	1	1.31	1.15

Computations were next carried out for low power conditions. The CO emissions predictions for this calculation are shown in Figure 4. The CO emissions at low power conditions can be significant, since quenching for CO oxidation reactions can occur at the lower combustor temperatures. Rolls-Royce combustor exit measurements indicated ~30 times more CO at low power compared to high power conditions, but still at relatively low levels. In the CFD predictions, a large amount of CO is predicted in the primary zone, and some oxidation occurs in the intermediate zone. However, complete oxidation does not occur in the intermediate zone, and the dilution air quenches the CO at nonequilibrium values in the dilution zone. The expected cause of high CO at lower power, i.e., liner cooling quenching, is not evident in these calculations, probably because the high CO in the mainstream masks any quenching that may occur along the liner. The CO predictions results seem to indicate that the LES with stronger mixing reduces the CO emissions at the combustor exit compared to RANS. This is most likely due to the shortened slightly fuel-rich primary zone predicted in the LES case. The exit CO emissions for LES are ~20% less than the RANS predictions. Table 2 shows comparisons of the predictions with experimental data. Despite the improvement for LES, both RANS and LES over predict the combustor exit CO emissions by substantial amounts. It is expected that improvements to the chemical kinetics mechanism will help the low power CO predictions. The current CO oxidation model assumes equilibrium levels of OH and does not include finite-rate kinetics of other minor species.

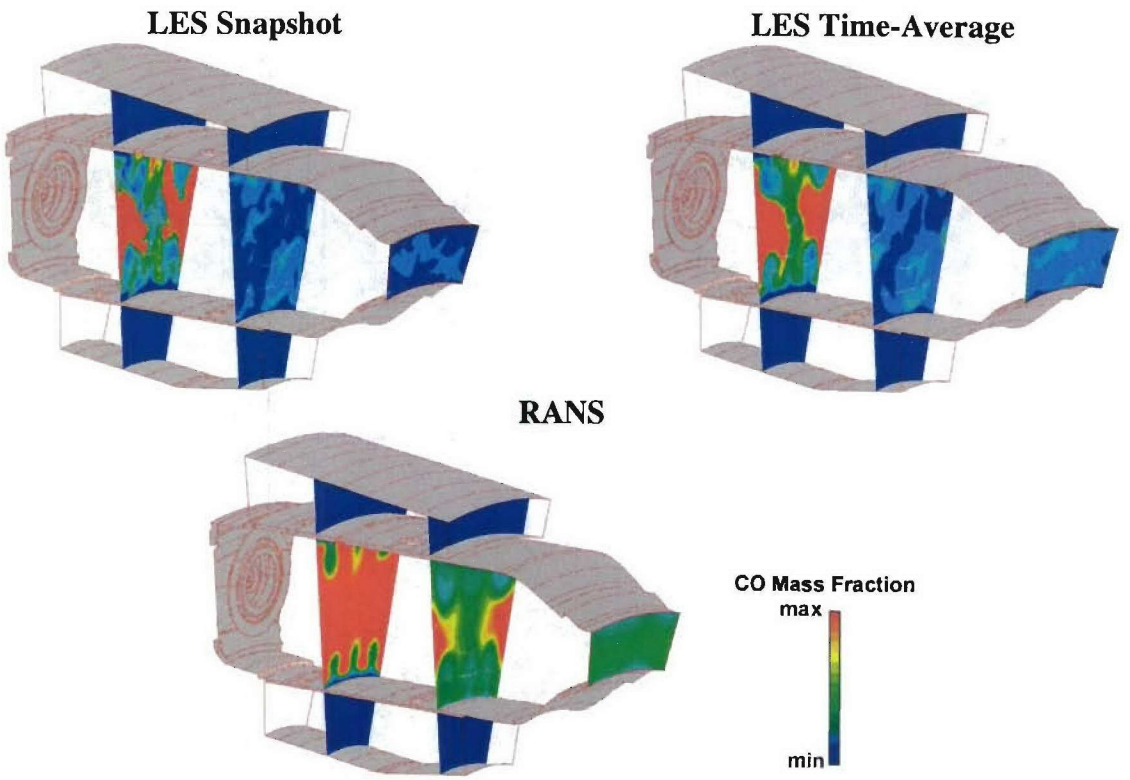

Figure 4. Comparison of CO Emissions Predictions for LES and RANS at Low Power Conditions

Table 2. Predicted and Measured CO, NO_x, and Temperature for AE3007 Low Power Conditions

	Experimental	**RANS**	**LES**
$T/T_{measured}$	1	0.94	0.96
$CO/CO_{measured}$	1	9.27	7.5
$NO_x/NO_{x,measured}$	1	1.12	0.85

The difference between the LES and RANS NO_x emissions at low power was relatively small. It can be seen that the NO_x is less at the combustor exit for the LES. The lower predicted NO_x for LES is due to the better mixing and reduction in peak temperature for the LES. The comparison with data in Table 2 indicates that the RANS is ~12% higher than data and the LES is ~15% lower than the measurements. Since the measured NO_x is quite low, these small discrepancies are not too serious and both LES and RANS essentially provide equally good predictive capabilities for low power NO_x.

The Phase I research demonstrated the combustion LES has significant potential to provide improved capabilities to accurately predict emissions. Needed capabilities with respect to combustion modeling were identified. Specific areas identified during Phase I where improvements in modeling capability are needed include turbulence chemistry interactions with multi-step chemical mechanisms, relevant multi-step mechanisms for JP-8, and algorithms to improve the speed of the complex chemistry calculations. Work performed in Phase II addresses needs related to turbulence-chemistry interaction and multi-step chemistry. Tasks include development and validation of the new capabilities, along with application to the Rolls Royce JSF combustor.

2. TECHNICAL OBJECTIVES

The overall goal of this SBIR project was to develop an analysis tool that captures the fundamental physics of NO_x, CO, and UHC emissions in high performance gas turbine combustors. In Phase I, the feasibility of the proposed analysis to predict emissions was demonstrated by predicting CO and NO_x emissions in a production Rolls-Royce aeroengine gas turbine combustor. In Phase II, the development of the LES combustion models continued. A significant amount of validation took place and the capability was applied to the JSF combustor. Specific objectives of the current Phase II program were:

1. Incorporate multi-step assumed PDF method into combustion LES code.
2. Develop and apply reduced (10-12 species) JP-8 chemical kinetic mechanism for JSF combustor conditions.
3. Validate the combustion LES code against benchmark DOE SimVal combustor data for predicting combustion dynamics and emissions at lean conditions using gaseous fuels.
4. Validate the combustion LES code against published validation data for premixed and diffusion flames.
5. Apply combustion LES code to the Rolls-Royce JSF combustor design.

Objectives one through five were achieved during the completion of the program. However, the validation and application of the combustion model were more limited than originally planned, due to difficulties in solving the coupled enthalpy and species equations. The technical challenge associated with the solution procedure was discovered late in the Phase II effort and the solution of the problem was beyond the scope of the Phase II effort. Sufficient simulations were performed to demonstrate the feasibility of the multi-step PDF combustion model, but application of the capability to transient LES simulations will be limited until the inadequacies of the solution procedure is addressed.

3. RESULTS

The following section contains a complete description of the work performed during this Phase II SBIR project. Table 3 shows a graph of the project schedule and marks the completion of the project milestones.

Table 3. Work Schedule

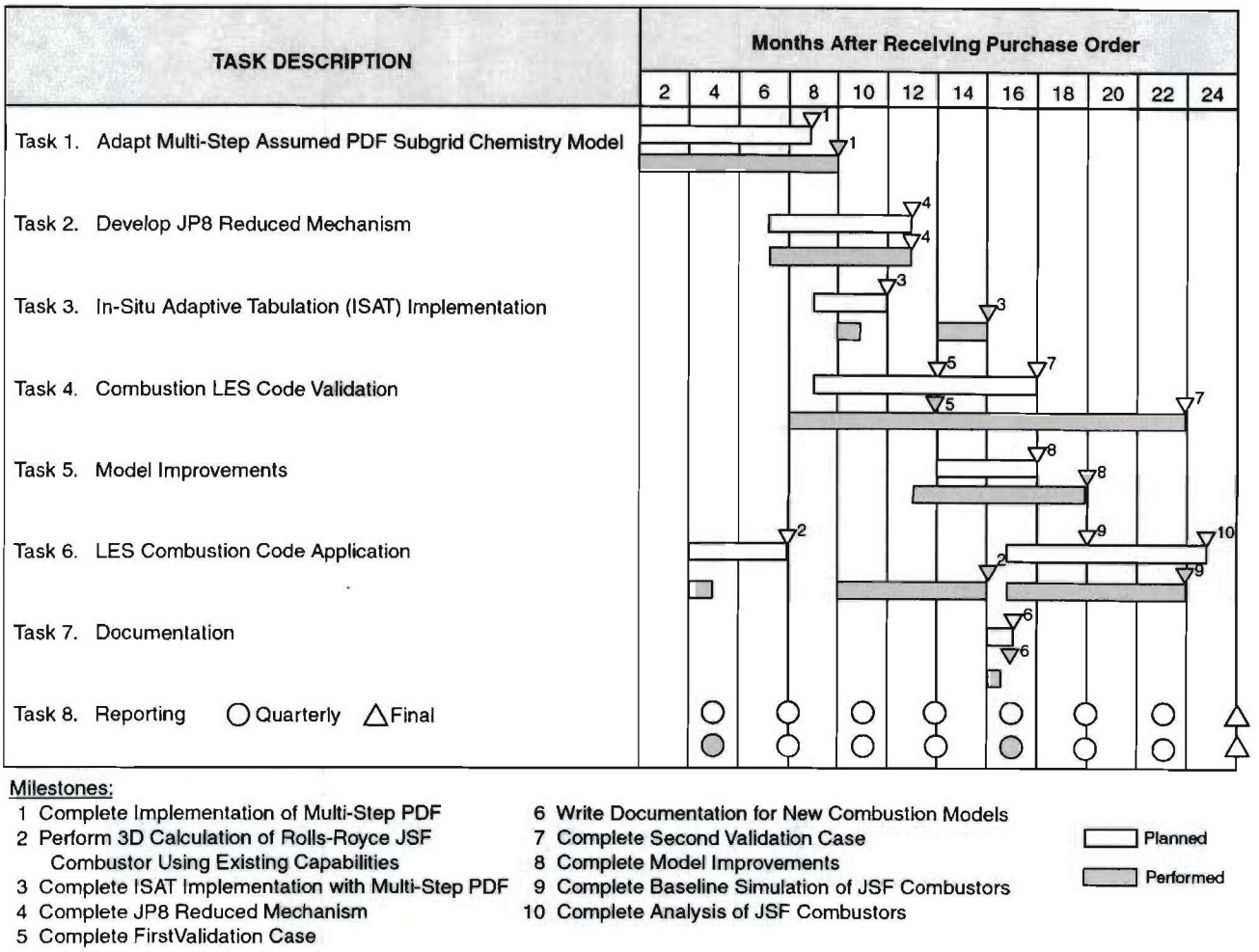

Extensive improvements in the combustion modeling capabilities were performed in CFD-ACE+ during this Phase II SBIR program. All the efforts were focused on capabilities applicable to Large Eddy Simulation (LES), or that can be used for both RANS and LES calculations. Section 3.1 describes the improvements and models added to the existing LES capabilities, and also provides an overview the LES modeling capabilities in CFD-ACE+. The new multi-step PDF combustion model developed under this SBIR program is described in Sections 3.2. Improvements in LES boundary conditions are discussed in Section 3.3. Generation of multi-step mechanisms is discussed in Section 3.4, followed by the discussion of the validation results in Section 3.5. The results of the JSF simulations are briefly described in Section 3.6, and the results of these analyses are included in an export-controlled and proprietary addendum report.

3.1 Improvements to Existing LES Models

LES Overview: LES is a time-accurate solution to the Navier Stokes equations with grid sizes and time steps that are small enough to resolve the energy-containing scales of a turbulent flow. Subgrid models for turbulent mixing and chemical reaction are needed to resolve the small-scale effects that are more universal and easier to approximate. Each variable in a LES is decomposed

into a large-scale component (indicated by an overbar) and a residual component (indicated by a prime),

$$f = \bar{f} + f' \tag{1}$$

The large-scale component is obtained by spatially averaging f with a filter function G,

$$\bar{f} = \int f(x')G(x,x')dx' \tag{2}$$

The filter effectively eliminates fluctuations on scales smaller than a specified size. The large scale, or resolved components are time dependent, in contrast to the average components in conventional (Reynolds averaged) turbulence modeling. For variable density flows, CFDRC uses Favre (density weighted) filtering:

$$\tilde{f} = \frac{\overline{\rho f}}{\bar{\rho}} \tag{3}$$

With the application of an LES Favre averaging procedure to the governing transport equations (mass, momentum, energy, species mass fractions, respectively), we obtain:

$$\begin{aligned}
&\frac{\partial \bar{\rho}}{\partial t} + \frac{\partial \bar{\rho}\tilde{u}_i}{\partial x_i} = 0 \\
&\frac{\partial \bar{\rho}\tilde{u}_j}{\partial t} + \frac{\partial \bar{\rho}\tilde{u}_i\tilde{u}_j}{\partial x_i} = \frac{\partial \tilde{\tau}_{ij}}{\partial x_i} - \frac{\partial T_{ij}}{\partial x_i} \\
&\frac{\partial \bar{\rho}\tilde{E}}{\partial t} + \frac{\partial \bar{\rho}\tilde{u}_i\tilde{E}}{\partial x_i} = \frac{\partial \tau_{ij}u_j}{\partial x_i} - \frac{\partial Q_i}{\partial x_i} \\
&\frac{\partial \bar{\rho}\tilde{\phi}_\alpha}{\partial t} + \frac{\partial \bar{\rho}\tilde{u}_i\tilde{\phi}_\alpha}{\partial x_i} = -\frac{\partial \tilde{J}_i^\alpha}{\partial x_i} - \frac{\partial M_i^\alpha}{\partial x_i} - \tilde{\omega}_\alpha
\end{aligned} \tag{4}$$

The filtered equations contain unknown terms such as τ_{ij} (velocity-velocity correlation) arising from the filtering of nonlinear terms and are known as subgrid scale (SGS) stresses. The closure problem of turbulent flows using LES is handled by providing models for the various subgrid scale correlations.

Subgrid Turbulence: Unlike typical steady-state turbulence models, the turbulence models for LES compute an eddy viscosity that is a function of the grid (or filter) size. The larger the size of the computational cells the higher the value of the subgrid turbulent viscosity. Thus, as the grid is made finer, the modeled effect of subgrid turbulent mixing becomes less important and more large-scale phenomena are then directly computed. The Smagorinsky model (Smagorinsky, 1963) computes the turbulent viscosity from the magnitude of the resolved strain tensor S_{ij}, the grid filter width Δ, and the Smagorinsky constant C_s according to:

$$\nu_t = (C_s\Delta)^2|S|, \text{ where } \bar{S}_{ij} = \frac{1}{2}\left(\frac{\partial \bar{u}_i}{\partial x_j} + \frac{\partial \bar{u}_j}{\partial x_i}\right) \tag{5}$$

where the grid filter width is computed as the cube root of the grid cell volume. This implementation allows LES calculations with arbitrary grid types, including hybrid grid schemes. Various studies have shown that the tunable parameter C_s in the Smagorinsky model is not a universal constant (Avva and Sundaram, 1998). It has been suggested that the C_s parameter should be flow dependent and should vary from region to region in complex flows.

A LES model which provides a flow dependent subgrid viscosity parameter is Localized Dynamic subgrid Kinetic energy model (LDKM) and is the basis for the newly developed model for the scalar dissipation coefficient. The LDKM model was developed by Kim and Menon (1997) to provide subgrid stresses without a priori specification of any constants. The LDKM uses scale similarity and the subgrid-scale kinetic energy

$$k_{sgs} = \frac{1}{2}\left(\overline{u_k u_k} - \bar{u}_k \bar{u}_k\right) \tag{6}$$

to model the unresolved scales. Using k_{sgs} the subgrid stress tensor is modeled as

$$\tau_{ij} = -2C_\tau \bar{\Delta} k_{sgs}^{1/2} \bar{S}_{ij} + \frac{2}{3}\delta_{ij} k_{sgs} \tag{7}$$

with the resolved-scale strain tensor defined as

$$\bar{S}_{ij} = \frac{1}{2}\left(\frac{\partial \bar{u}_i}{\partial x_j} + \frac{\partial \bar{u}_i}{\partial x_i}\right). \tag{8}$$

In the modeling of the SGS stresses, implicitly the eddy viscosity is parameterized as

$$\nu_T = C_\tau \bar{\Delta} k_{sgs}^{1/2}. \tag{9}$$

The subgrid-scale kinetic energy is obtained by solving the transport equation

$$\frac{\partial k_{sgs}}{\partial t} + \bar{u}_i \frac{\partial k_{sgs}}{\partial x_i} = -\tau_{ij}\frac{\partial \bar{u}_i}{\partial x_j} - \varepsilon_{sgs} + \frac{\partial}{\partial x_i}\left(\nu_T \frac{\partial k_{sgs}}{\partial x_i}\right) \tag{10}$$

which is closed by providing a model for the subgrid dissipation rate term, ε_{sgs}, based on simple scaling arguments

$$\varepsilon_{sgs} = C_\varepsilon \frac{k_{sgs}^{3/2}}{\bar{\Delta}} \tag{11}$$

In these models, C_τ and C_ε are adjustable coefficients determined dynamically using the information from a resolved test-scale field. The test-scale field is constructed from the large-scale field by applying a test filter, which is characterized by $\ddot{\Delta}$, the test filter width. In the LES code, with arbitrary grids, we are using a test filter consisting of a weighted average of the cells sharing a node with the current cell. This average is biased towards the current cell, with a weight equal to the number of vertices of the cell. The cells that share a face with a current cell have a weight of two.

The application of the test filter on any variable is denoted by the top hat. By definition, the Leonard stress tensor at the test-scale level is

$$L_{ij} = \widehat{\bar{u}_i \bar{u}_j} - \hat{\bar{u}}_i \hat{\bar{u}}_j \tag{12}$$

The Leonard stress tensor and the SGS tensor are known to have high degrees of correlation, which justifies the use of similarity in the derivation of the dynamic model coefficients. The resolved kinetic energy at the test filter level is defined from the trace of the Leonard stress tensor

$$k_{test} = \frac{1}{2}\left(\widehat{\bar{u}_k \bar{u}_k} - \hat{\bar{u}}_k \hat{\bar{u}}_k\right). \tag{13}$$

This test scale kinetic energy is dissipated at small scales by

$$e = (\nu + \nu_T)\left(\widehat{\frac{\partial \bar{u}_i}{\partial x_j}\frac{\partial \bar{u}_i}{\partial x_j}} - \frac{\partial \hat{\bar{u}}_i}{\partial x_j}\frac{\partial \hat{\bar{u}}_i}{\partial x_j}\right) \tag{14}$$

Based on a similarity assumption and using appropriately defined parameters, the Leonard stress tensor has a representation analogous to the SGS stress tensor

$$L_{ij} = -2C_\tau \hat{\Delta} k_{test}^{1/2} \hat{\bar{S}}_{ij} + \frac{1}{3}\delta_{ij} L_{kk} \tag{15}$$

The least square method is applied to obtain the model constant

$$C_\tau = \frac{1}{2}\frac{L_{ij}\sigma_{ij}}{\sigma_{ij}\sigma_{ij}} \tag{16}$$

where

$$\sigma_{ij} = -\hat{\Delta} k_{test}^{1/2} \hat{\bar{S}}_{ij} \tag{17}$$

Finally, a corresponding approach is used to determine the dissipation rate constant. By invoking similarity between the dissipation rates at the subgrid level and at the test scale level C_ε is determined to be

$$C_\varepsilon = \frac{\widehat{\left(\partial \bar{u}_i/\partial x_j\right)\left(\partial \bar{u}_i/\partial x_j\right)} - \left(\partial \hat{\bar{u}}_i/\partial x_j\right)\left(\partial \hat{\bar{u}}_i/\partial x_j\right)}{\left[(\nu + \nu_T)\hat{\Delta}\right]^{-1} k_{test}^{3/2}} \tag{18}$$

The coefficients of the LDKM model are Galilean invariable and realizable. This model is also quite simple and efficient, does not rely on any *ad hoc* procedures, and it is applicable to various flow fields without adjustment of the model. The subgrid turbulence kinetic energy k_{sgs} from the LDKM is the required input for several subgrid chemistry models such as the assumed PDF and the Linear Eddy Model.

3.1.2 Development of LDVM for the PDF Combustion Model

The equations solved by CFD-ACE+ for LES of turbulent reacting flows are transport equations for filtered density-weighted values. The effect of turbulence on chemical reaction and on composition dependent variables, such as density or temperature, must be accounted for. The filtered values of density and temperature cannot be calculated from the filtered value of the mass fractions since they are nonlinear functions of the composition. These variables can be calculated more accurately by integrating the product of the variable of interest and the filtered density-weighted joint composition probability density function (PDF) over the range of composition values. In order to have a simpler model to work with and to increase computational efficiency, we have decided to focus on the assumed PDF approach.

The filtered joint composition PDF is a complete statistical description of the composition of the fluid at a single point in space and time. If the PDF is known, then the filtered value of any function of composition can be evaluated by multiplying that function by the PDF and integrating over the range of possible compositions.

$$\overline{\omega(Y_1,\ldots,Y_N;x,t)} = \int \omega(Y_1,\ldots,Y_N)$$

$$\left(P(Y_1,\ldots,Y_N;x,t)dY_1\ldots dY_N\right) \tag{19}$$

where $P(Y_1,..,Y_N;x,t)$ is the filtered joint PDF of the N mass fractions at the position x and time t and $\omega(Y_1,...,Y_N)$ is an arbitrary function of the mass fractions. Favre-filtered quantities can be calculated by defining a filtered density-weighted PDF.

$$\tilde{P}(Y_1,\ldots,Y_n) = \frac{\Sigma\rho(Y_1,\ldots,Y_N)P(Y_1,\ldots,Y_N)}{\overline{\rho(Y_1,\ldots,Y_N)}} \tag{20}$$

A parametric form of the PDF is assumed and the parameters in the model are related to variables governed by transport equations. The parametric form of the PDF assumes the composition can be specified by a single mixture fraction and a single reaction progress variable. This assumption limits the reaction models available when the prescribed PDF model is used. The mass diffusivities of all species must be equal and no more than two mixtures can be defined. In the following sections, determination of the PDF and the filtered variables will be described.

Determination of PDF: The joint composition PDF is a function of a mixture fraction and a reaction progress variable. The reaction progress is defined as

$$\theta = \frac{\left(Y_{f,max} - Y_f\right)}{\left(Y_{f,max} - Y_{f,min}\right)} \tag{21}$$

where Y_f is the mass fraction of the fuel in the one step reaction and the minimum and maximum values are functions of the mixture fraction. The mixture fraction and reaction progress are assumed to be independent, so the two-dimensional PDF is a product of the two one-dimensional PDF's.

$$P(f,\theta) = P(f)P(\theta) \tag{22}$$

The one-dimensional PDF's both have two parameters that are related to the filtered mean and the subgrid variance of the mixture fraction or reaction progress.

In the present approach, transport equations are solved for both the filtered mean and variance of the corresponding variable. The transport equations for the variances of the mixture fraction and reaction progress include production terms caused by gradients in the filtered values, dissipation terms, and (for the reaction progress) a term due to chemical reaction.

$$\frac{\partial}{\partial t}\bar{\rho}\sigma_{\tilde{f}}^2 + \frac{\partial}{\partial x_j}\bar{\rho}\tilde{u}_j\sigma_{\tilde{f}}^2 = \frac{\partial}{\partial x_j}\left\{\Gamma_t\frac{\partial\sigma_{\tilde{f}}^2}{\partial x_j}\right\} + 2\Gamma\left(\frac{\partial\tilde{f}}{\partial x_j}\right)^2 - C_\chi\frac{\bar{\rho}\varepsilon}{k}\sigma_{\tilde{f}}^2 \tag{23}$$

$$\frac{\partial}{\partial t}\bar{\rho}\sigma_{\tilde{\theta}}^2 + \frac{\partial}{\partial x_j}\bar{\rho}\tilde{u}_j\sigma_{\tilde{\theta}}^2 = \frac{\partial}{\partial x_j}\left\{\Gamma_t\frac{\partial\sigma_{\tilde{\theta}}^2}{\partial x_j}\right\} + 2\Gamma\left(\frac{\partial\tilde{\theta}}{\partial x_j}\right)^2 - C_\chi\frac{\bar{\rho}\varepsilon}{k}\sigma_{\tilde{\theta}}^2 + S_\omega \tag{24}$$

In the preceding equations, C_χ has the value of 2 in RANS methodology. To improve the predictions in LES we have derived a Localized Dynamic Subgrid Variance model (LDVM). This new closure follows the logic behind the derivation the Localized Dynamic Subgrid Kinetic energy model (LDKM). Furthermore, computationally the new subgrid variance model relies on information provided by the LDKM with quantities such as subgrid kinetic energy and subgrid kinetic energy dissipation.

In the new model, C_χ is an adjustable coefficient determined dynamically using the information from a resolved test-scale field. The derivation starts from the definition of the variance of scalar Z (representing either the mixture fraction or the reaction progress variable). The subgrid scalar variance is defined as $V_{sgs} = \overline{Z^2} - \overline{Z}^2$, whereas the scalar variance at the test level is $V_{test} = \hat{\bar{Z}}^2 - \hat{\bar{Z}}^2$. From dimensional analysis the subgrid scalar dissipation is modeled by

$$\chi_{sgs} \equiv 2D\left(\overline{\frac{\partial Z}{\partial x_i}\frac{\partial Z}{\partial x_i}} - \frac{\partial \bar{Z}}{\partial x_i}\frac{\partial \bar{Z}}{\partial x_i}\right) = C_\chi \frac{\varepsilon_{sgs}}{k_{sgs}} V_{sgs} \tag{25}$$

and by invoking the principle of similarity between the test level and the subgrid level quantities, the scalar dissipation at the test level is

$$\chi_{test} \equiv 2(D + D_T)\left(\widehat{\frac{\partial \bar{Z}}{\partial x_i}\frac{\partial \bar{Z}}{\partial x_i}} - \frac{\partial \hat{\bar{Z}}}{\partial x_i}\frac{\partial \hat{\bar{Z}}}{\partial x_i}\right) \tag{26}$$

where D_T is the turbulent diffusivity. Since χ_{test} is fully resolved at every point in the computational domain, it will be used to calculate the unknown parameter C_χ. The turbulent dissipation at the test level is expressed as

$$\varepsilon_{test} = C_\varepsilon \frac{k_{test}^{3/2}}{\hat{\Delta}} \tag{27}$$

Using equation (27), from equation (26) the final expression for the dynamic coefficient C_χ is obtained as

$$C_\chi = \frac{2(D + D_T)\hat{\Delta}\left(\widehat{\frac{\partial \bar{Z}}{\partial x_i}\frac{\partial \bar{Z}}{\partial x_i}} - \frac{\partial \hat{\bar{Z}}}{\partial x_i}\frac{\partial \hat{\bar{Z}}}{\partial x_i}\right)}{C_\varepsilon \sqrt{k_{test} V_{test}}} \tag{28}$$

This generic expression is used in the transport equations of the mixture fraction variance and reaction progress variance to compute the model coefficient of the dissipation term. In the next section we detail the results obtained with this new model for a bluff-body combustor.

3.1.3 Testing of LDVM Model

The LES calculations shown here have utilized the localized dynamic subgrid kinetic energy model (LDKM) for subgrid turbulence with 1-step chemistry and assumed PDF with LDVM model for subgrid chemistry. Figure 5 shows a comparison between the predictions of the assumed PDF model without (*i.e.* by using a constant C_χ=2) and with LDVM, for instantaneous temperature and the reaction progress variance.

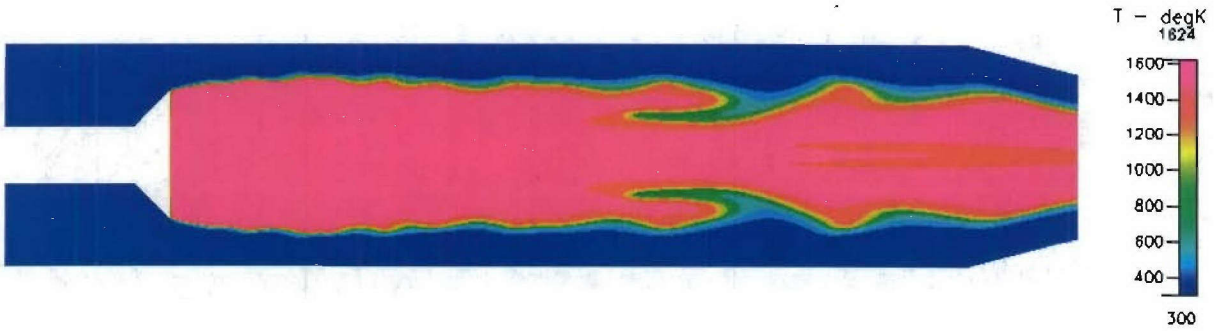

Instantaneous Temperature

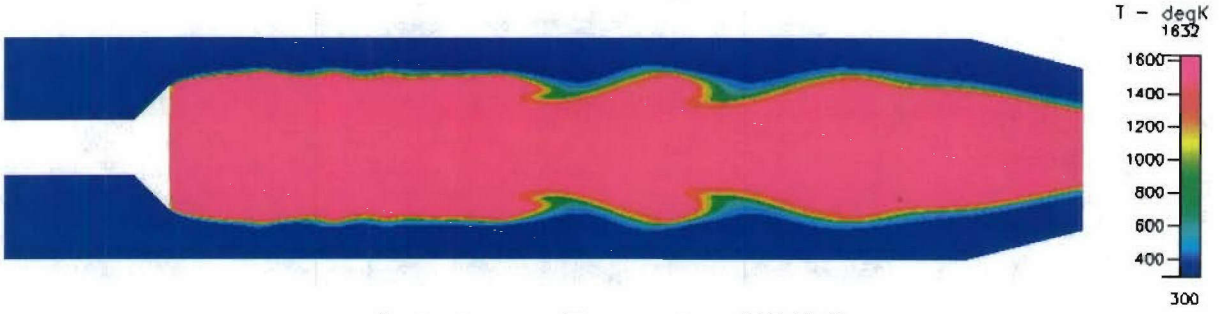

Instantaneous Temperature (LDVM)

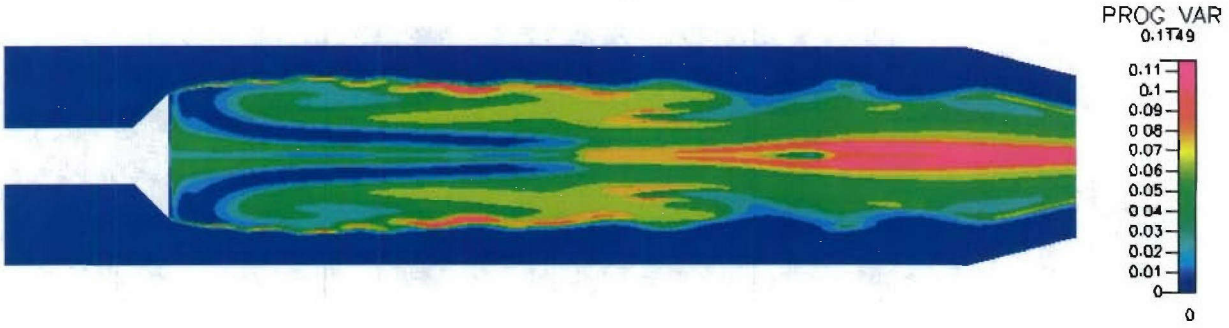

Progress Variable Variance

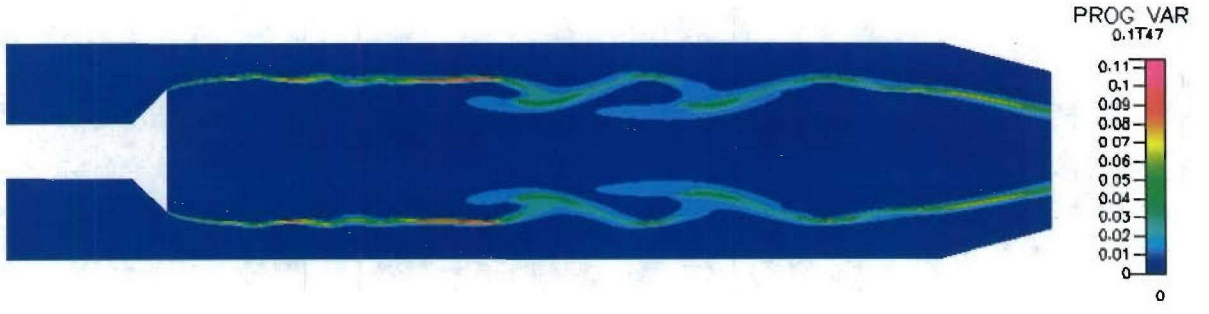

Progress Variable Variance (LDVM)

Figure 5. Predictions of Temperature and Variance in a Lean Premixed Bluff-Body Combustor Using Assumed PDF Model with LES

The most striking difference between the two models is apparent in the progress variable variance field snapshots. The LDVM model is tracking the flame front very closely, which is the ideal behavior for such chemistry models. Peak magnitudes are also similar to those seen in the flame location between the two simulations. The 2D calculations demonstrated that the LDVM technique was providing reasonable results, both in terms of location and magnitude.

The LDVM model has also been applied to the 3D DOE SimVal combustor. Work with the SimVal combustor at DOE is designed to provide experimental data that can be used to validate combustion CFD codes, with particular emphasis on understanding combustion instability, emissions, and variable fuel effects at actual gas turbine combustor conditions. Detailed experimental data are being obtained, including emission images, velocity, temperature, and species maps, and dynamic wall pressure.

The baseline geometry of the SimVal combustor includes well-defined acoustic boundaries with a choke plate immediately upstream of the swirl vanes and a choked nozzle at the downstream end of a resonant section. Figure 6 shows the baseline geometry. The corresponding CFD model is shown in Figure 7. The baseline operating conditions included:

Air Mass Flow-Rate 0.26 kg/sec
Inlet Air Temperature 600 K (620 F)
Equivalence Ratio 0.47 - 0.7
Pressure ~ 4.5 atm (varied with equivalence ratio)

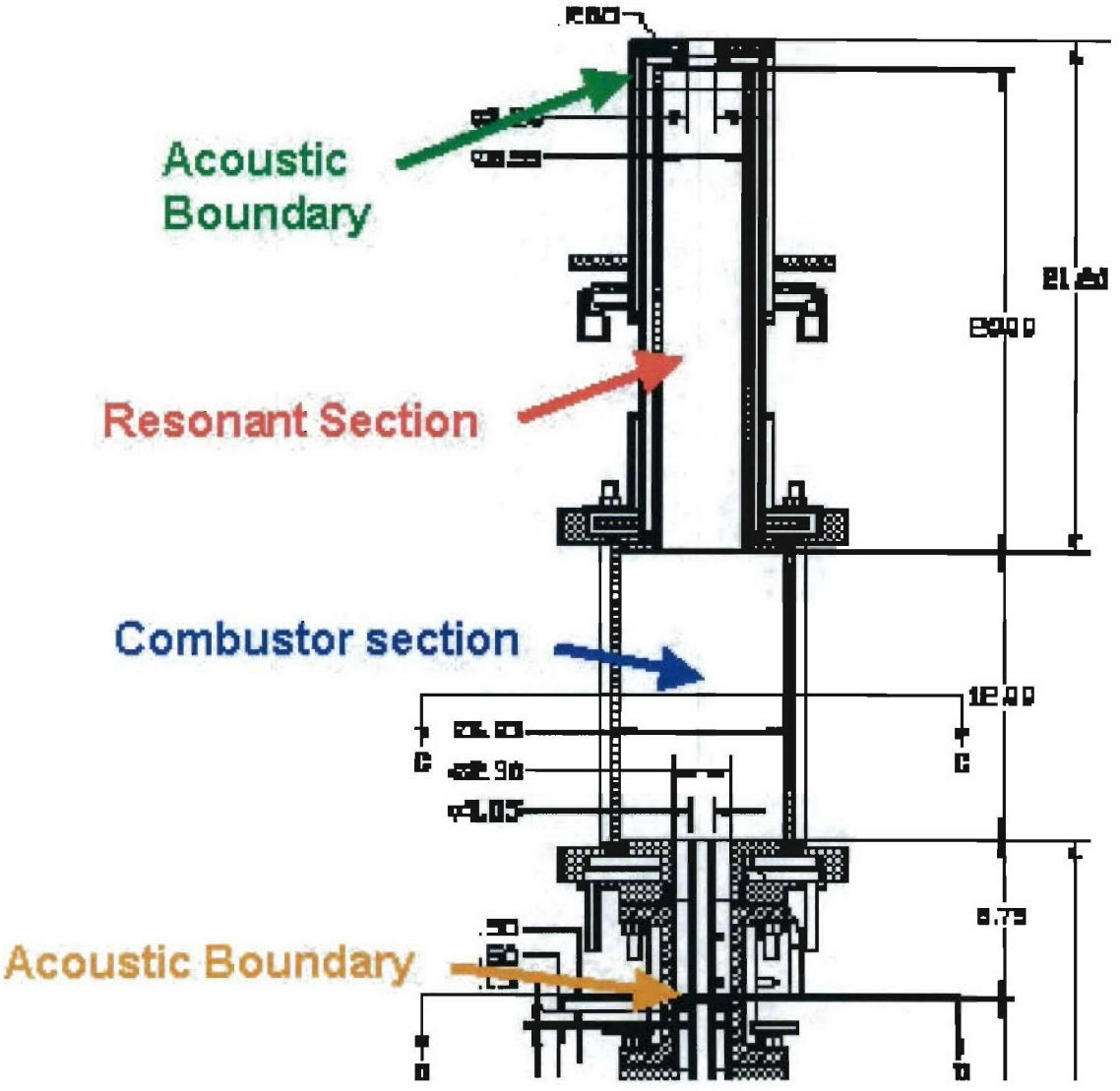

Figure 6. Baseline Geometry for SimVal Combustor

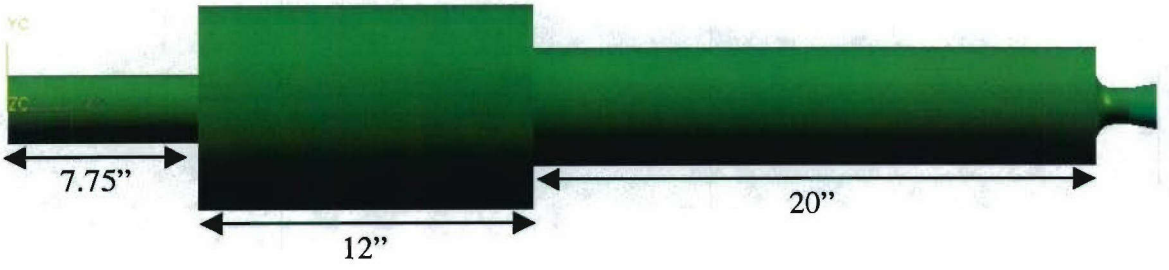

Figure 7. SimVal Geometry for Baseline Case

Figure 8 shows the preliminary results of the vorticity magnitude and NO_x source term at an equivalence ratio of 0.7, obtained prior to the development of the LDVM model. The NO_x rate increases in the shear layer where vorticity is high and then decreases near the cool walls.

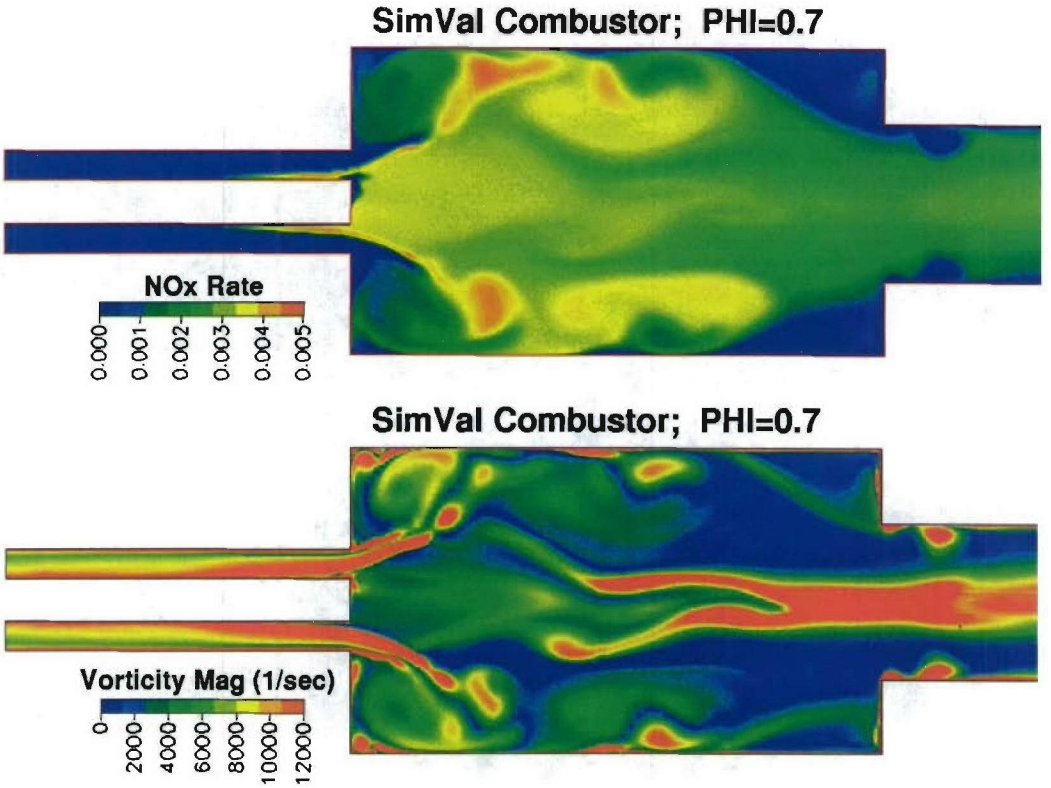

Figure 8. 3D LES Snapshot of Filtered NO_x Source Term and Vorticity Magnitude (ϕ=0.7)

The NO_x and CO emissions were over predicted, possibly due to improper estimated wall temperatures. At higher fuel-air ratios the LES predictions also predicted flashback into the premix barrel, while the experiments did not.

Simulations of the SimVal combustor were completed using the LDVM model with the two-variable PDF (single-step rate). Figure 9 and 10 show the progress and progress variance in the combustor. The progress variable tracks the flame location in the premixed combustor. Both plots show reasonable characteristics using the LDVM model. Also, the tendency of the flame to propagate along the inside diameter of the premix barrel has been eliminated. The flame now stabilizes at a location just inside in the barrel. This is shown in Figure 11 where temperature is plotted on an isosurface of progress (0.9 – corresponding to nearly complete reaction).

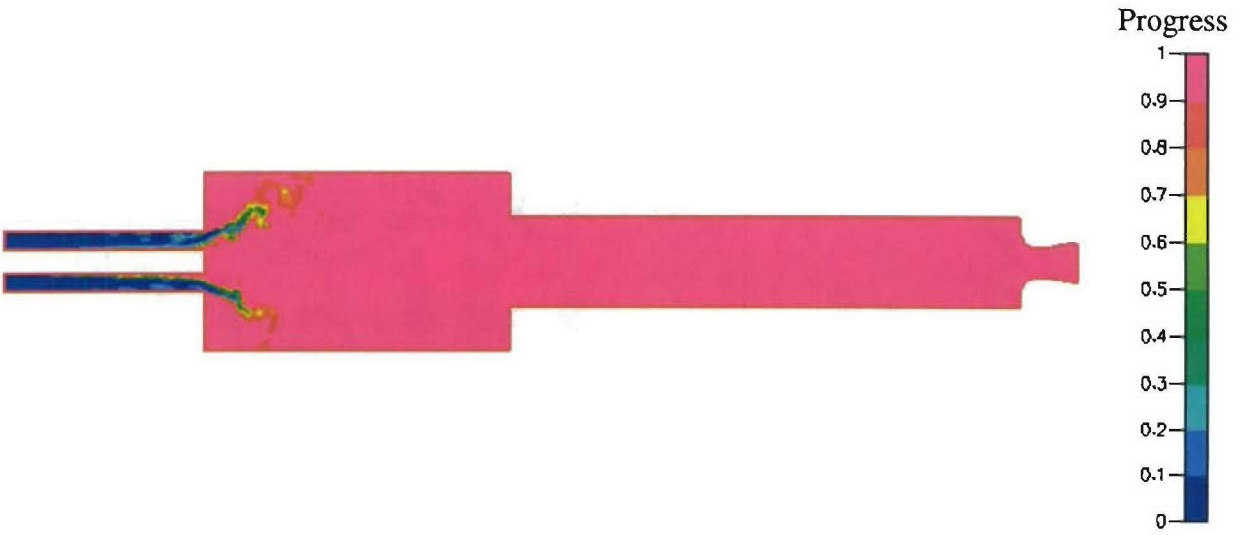

Figure 9. Reaction Progress with the LDVM Model

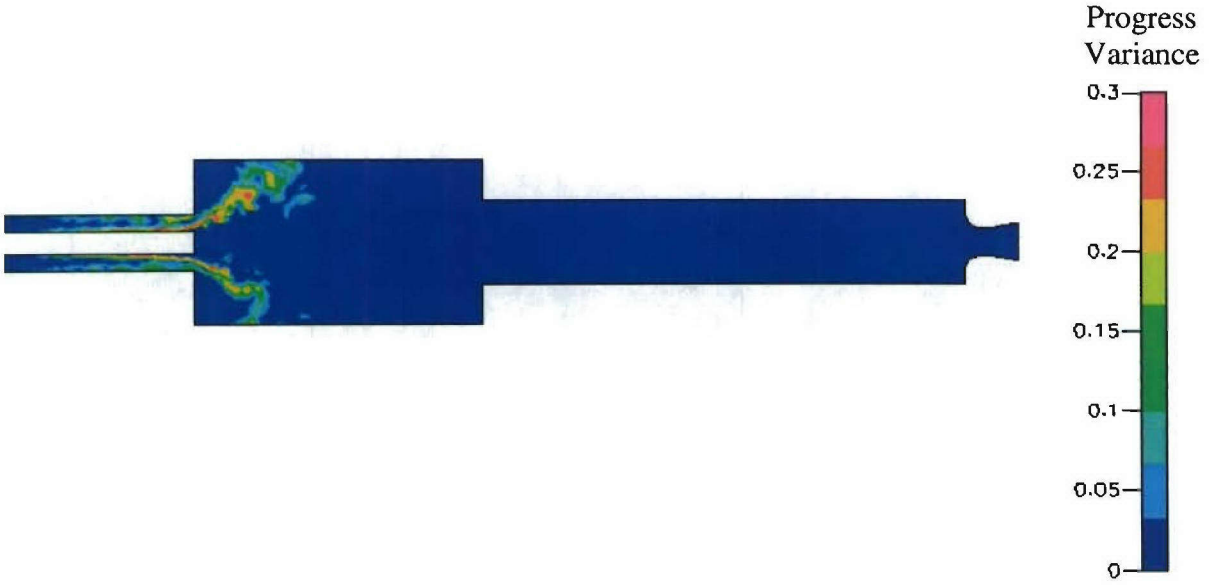

Figure 10. Reaction Progress Variance with the LDVM Model

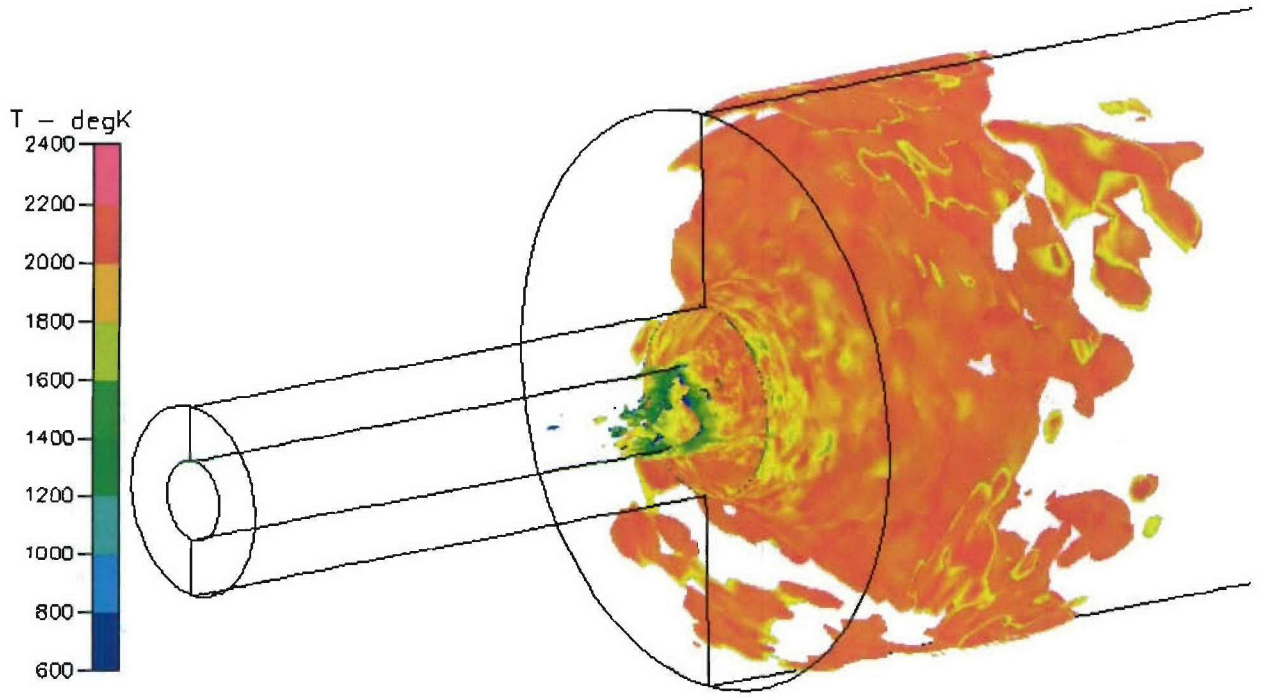

Figure 11. Temperature Plotted at a Reaction Progress of 0.9

Snapshots of temperature contours at various times using the LDVM model are shown in Figure 12. Similar to the results shown in Figure 11, it can be seen that the flame anchors on the centerbody, a short distance upstream of the exit. This location of flame anchoring closely mimics the experiment based on observations of the experimentalists. Another feature seen in Figure 11 is the fine-scale structure of the flame, which is more in-line with what is expected in LES calculations. This is the result of inlet turbulence, which was not captured in previous LES runs. The improved boundary conditions (described in Section 3.3) effectively introduce reasonable length scales in the turbulent flow structure that propagate through the premix tube.

Snapshots of NO_x contours at various times are shown in Figure 13. NO_x at the exit is approximately 80 ppm, much higher than extrapolated from the measurements. Unfortunately, the wall heat losses were not correctly accounted for, so the LES calculation had higher bulk temperatures in the combustor and exhaust duct than the experiment. Capturing heat loss with LES is highly dependant on the wall function models and near wall grid distribution. In an ongoing SBIR program with the Navy, CFDRC is improving near wall heat transfer and velocity models for LES simulations to provide accurate heat transfer characteristics.

The combustor computational model was very quiet in terms of pressure dynamics. Pressure rms values of ~0.3 psi were predicted. This was in-line with extrapolated pressure rms measurements.

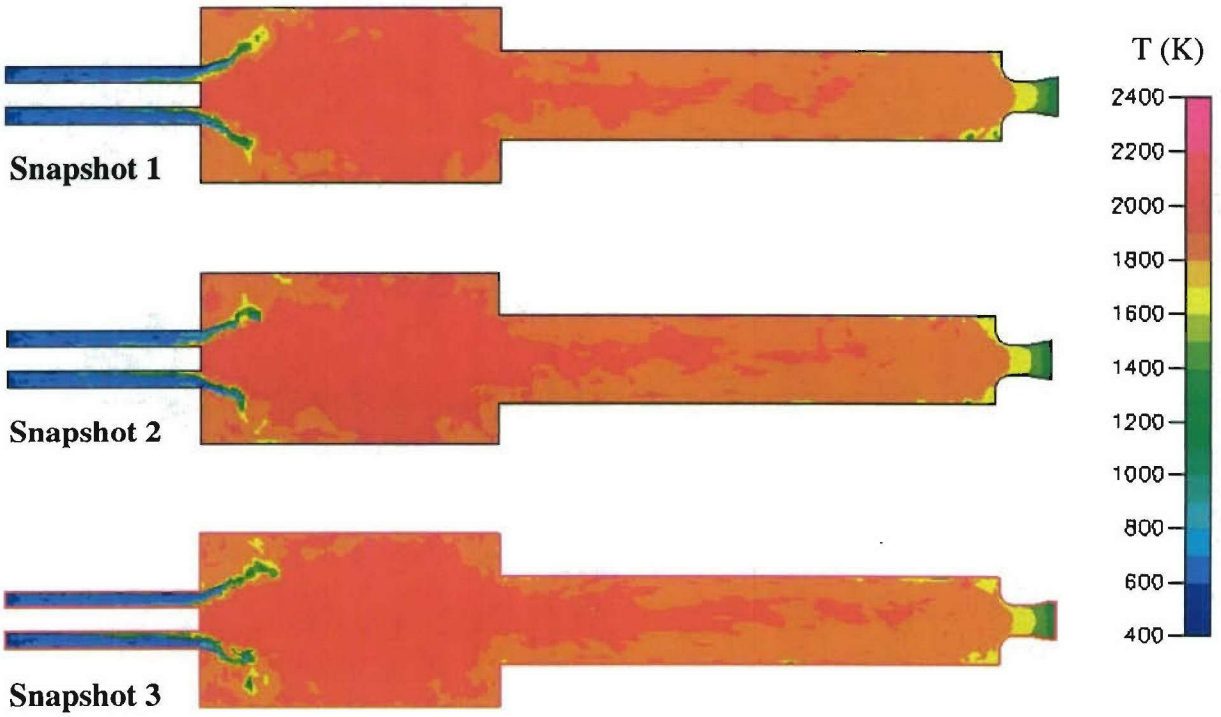

Figure 12. Snapshots of Temperature Contours in the SimVal Combustor

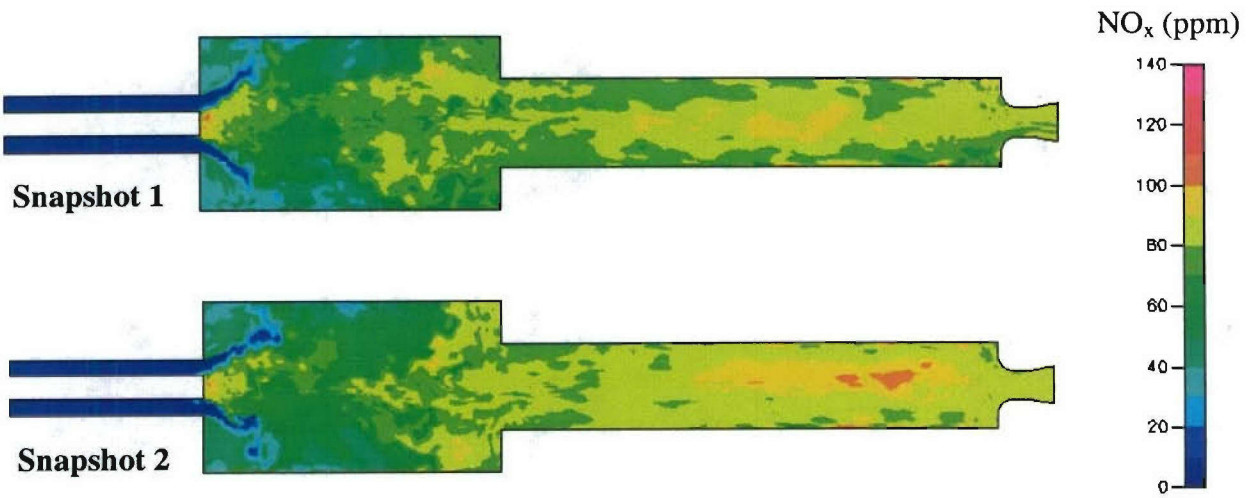

Figure 13. Snapshots of NO_x Contours in the SimVal Combustor

3.2 Multi-Step PDF Turbulent Combustion Model

Particularly for gas turbine combustion modeling, there is a pressing need for a practical, computationally efficient turbulent combustion model that is applicable to all types of flames, accounts for finite rate effects, and can be used with multi-step chemical mechanisms. To meet this need, a new assumed, two-variable, joint-PDF combustion model for multi-step reaction mechanisms has been developed in this SBIR. The model allows detailed chemistry for species and combustion predictions, with turbulence-chemistry interaction modeled by a joint PDF of two independent variables: the mixture fraction and reaction progress. A similar approach has been successfully used by Bohn and Lepers (1999). However, they used temperature instead of reaction progress as the second variable. The model described here can be used for simulations of premixed, diffusion, and partially premixed turbulent combustion with high prediction accuracy and minimal computational cost.

3.2.1 Model Description

The multi-step chemistry model consists of solving the fuel mixture fraction variance, fuel reaction progress variance, and species transport equations.

$$\frac{\partial}{\partial t}\left(\bar{\rho}\sigma_{\xi}^{2}\right)+\frac{\partial}{\partial x_j}\left(\bar{\rho}\tilde{u}_j\sigma_{\xi}^{2}\right)=\frac{\partial}{\partial x_j}\left(\Gamma\frac{\partial\sigma_{\xi}^{2}}{\partial x_j}\right)+2\Gamma\left(\frac{\partial\tilde{\xi}}{\partial x_j}\right)^{2}-C_D\frac{\bar{\rho}\varepsilon}{k}\sigma_{\xi}^{2} \tag{29}$$

$$\frac{\partial}{\partial t}\left(\bar{\rho}\sigma_{\theta}^{2}\right)+\frac{\partial}{\partial x_j}\left(\bar{\rho}\tilde{u}_j\sigma_{\theta}^{2}\right)=\frac{\partial}{\partial x_j}\left(\Gamma\frac{\partial\sigma_{\theta}^{2}}{\partial x_j}\right)+2\Gamma\left(\frac{\partial\tilde{\theta}}{\partial x_j}\right)^{2}-C_D\frac{\bar{\rho}\varepsilon}{k}\sigma_{\theta}^{2}+S_{\omega} \tag{30}$$

$$\frac{\partial\left(\bar{\rho}\tilde{Y}_i\right)}{\partial t}+\frac{\partial\left(\bar{\rho}\tilde{u}_j\tilde{Y}_i\right)}{\partial x_j}=\frac{\partial}{\partial x_j}\left[\left(\Gamma+\frac{\mu_t}{Sc_t}\right)\frac{\partial\tilde{Y}_i}{\partial x_j}\right]+M_i\tilde{\omega}_i+\left(\dot{m}_i\right)_{evap} \tag{11}$$

The fuel mixture fraction is defined by

$$\xi=\frac{Z-Z_{ox}}{Z_f-Z_{ox}} \tag{32}$$

where Z_k is defined as an atom that is present in the oxidizer and not the fuel (or vice-versa). Atomic nitrogen is currently being used.

The fuel reaction progress is defined by

$$\theta=\frac{Y_{f,\max}-Y_f}{Y_{f,\max}-Y_{f,\min}} \tag{33}$$

where $Y_{f,\max}$ and $Y_{f,\min}$ are strictly functions of the fuel mixture fraction, and Y_f is the fuel mass fraction.

The variables ξ, θ, σ_ξ, and σ_θ are needed to define the probability density function (PDF) that is used in determining PDF-averaged quantities of temperature, specific volume, and reaction rate. These averaged quantities are determined by integrating the instantaneous values over the PDF.

$$\tilde{\alpha} = \iint \alpha(\theta,\xi)\ p(\theta,\xi) d\theta\ d\xi \tag{34}$$

where α is the quantity being averaged and $p(\theta,\xi)$ is the PDF as a function of fuel mixture fraction and fuel reaction progress, which are assumed to be independent and to be represented as $p(\theta)p(\xi)$. The shape of the PDF is user-specified. For ξ, the shape can be a beta function or a top-hat function. For θ, the shape can be one of top-hat or tri-delta. The variances determine the spread of the PDF and are known from solving the two variance transport equations (Eq. 29 and 30).

The instantaneous reaction rate for step k is obtained from the equation

$$r_k = A T^{\beta} P^{\gamma} e^{\left(-\frac{E_a}{RT}\right)} \prod_j c_j^{\alpha_j} \tag{35}$$

where A is the pre-exponential factor, β is the temperature exponent, γ is the pressure exponent, E_a is the activation energy, R is the universal gas constant, c_j is the concentration of reactant j, and α_j is the concentration exponent for reactant j. The PDF-averaged reaction rate for step k is

$$\tilde{r}_k = \iint r_k\, p(\theta)p(\xi) d\theta\, d\xi \tag{36}$$

The PDF-averaged species net production rate is determined from

$$\tilde{\dot{\omega}}_i = \sum_k \nu_{i(k)} \tilde{r}_k \tag{37}$$

where $\nu_{i(k)}$ is the stoichiometric coefficient for species i in reaction k.

The derivative of $\tilde{\dot{\omega}}_i$ with respect to c_j is needed for the linearized portion of the species transport equation source term. This derivative is obtained as

$$\frac{d\tilde{\dot{\omega}}_i}{dc_j} = \sum_k \nu_{i(k)} \frac{d\tilde{r}_k}{dc_j} \tag{38}$$

where

$$\frac{d\tilde{r}_k}{dc_j} = \iint \frac{dr_k}{dc_j} p(\theta)p(\xi) d\theta\, d\xi \tag{39}$$

and

$$\frac{dr_k}{dc_j} = \begin{cases} \alpha_j \dfrac{r_k}{c_j} \text{ where } c_j \text{ is a reactant in step } k \\ 0 \text{ where } c_j \text{ is not a reactant in step } k \end{cases} \tag{40}$$

The determination of the functionality of the $\alpha(\theta,\xi)$ term in Equation 6 has not yet been defined. Equilibrium, at constant enthalpy and pressure, is used to define this functionality. The equilibrium values for temperature, specific volume, and reaction rate all vary strongly as a function of fuel reaction progress and fuel mixture fraction. The underlying assumption in using this approach is that the equilibrium profile shape of $\alpha(\theta,\xi)$ is the same as the instantaneous profile shape of α away from equilibrium. Figure 14 shows a sketch of what these corresponding profiles might look like over fuel reaction progress space.

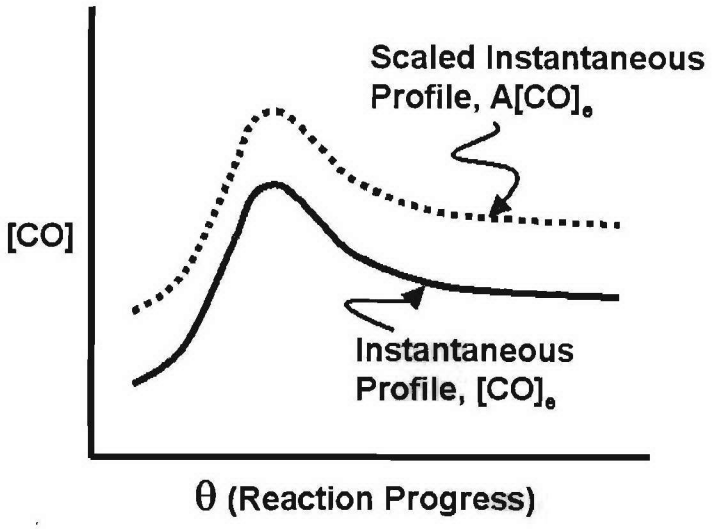

Figure 14. Equilibrium Concentrations Versus Instantaneous Concentrations as a Function of Reaction Progress

A difficulty arises in the solution of the transport equations when treating the PDF-averaged quantities in this manner. The averaged quantity in Equation 6, namely $\tilde{\alpha}$, is computed as if only a function of fuel mixture fraction and fuel reaction progress. Fuel mixture fraction and fuel reaction progress are both functions of the fuel reaction step but are not functions of the other steps in the multi-step global mechanism. For example, if the CO step is far from equilibrium, then the PDF-averaged quantity would be based on the equilibrium CO concentration but the CO would actually be far from equilibrium. Thus, $\alpha(\theta,\xi)$ used in Equation 6 would not be dependent on the solved-for species concentrations. A correction is needed to account for this error in the PDF-averaging approach. This correction consists of using scaling parameters to correct for non-equilibrium states. Corrections need to be made for PDF-averaged temperature and reaction rates. Specific volume corrections are implicitly made due to the temperature correction. The scaling parameter consists of the ratio of the solved for value to the equilibrium value at the mean values of θ and ξ.

$$\vartheta_j = \frac{Y_j}{(Y_j)_{eq}} \tag{41}$$

This ϑ_j is then used in correcting the reaction rate $\tilde{r}_k$ by

$$\tilde{r}_k' = \prod_j (\vartheta_j)^{\alpha_j} \tilde{r}_k \tag{42}$$

The derivative rates are corrected using this same ratio in this manner

$$\frac{d\tilde{r}_k}{dc_j}' = \prod_j (\vartheta_j)^{\alpha_j - 1} \frac{d\tilde{r}_k}{dc_j} \tag{43}$$

The temperature is corrected in a similar manner

$$\tilde{T}' = \eta \tilde{T}_{eq} \tag{44}$$

where

$$\eta = 1 - \Delta T / \tilde{T}_{eq} \tag{45}$$

where

$$\Delta T = T\left(\left(\tilde{Y}_{j=1\ldots N}\right)_{eq}\right) - T\left(\left(\tilde{Y}_{j=1\ldots N}\right)\right) \tag{46}$$

The two temperatures in Equation 46 are computed as a function of enthalpy and PDF-averaged species mass fractions and solved for mass fractions respectively.

Having determined the corrected PDF-averaged temperature, specific volume, and species net production rates, the solution then focuses on solving the species transport equations. These transport equations are very sensitive to large source terms for the consumption and/or production of species. The species net production rate is lagged one iteration to prevent undesired oscillations in the solution. Lagging the species source term creates the drawback that overshoot might occur. This overshoot can cause species fractions to become negative if not somehow limited or relaxed in the solution. The current implementation limits the reaction rates, not the species net production rate. Therefore, if negative species concentrations are being solved for, then all of the destruction steps for that species are reduced by 20%. This is continued until the species concentration is no more than half of its original value. This limiting technique works remarkably well. Typically, after just a few iterations the need for limiting vanishes for most of the computational cells if not for all of them. In some instances in the post flame region, the fuel fraction is very near zero. In these regions, limiting factors may still be required in order to keep the solution well behaved. However, this type of limiting only affects the fuel species well downstream of the flame and does not affect the integrity of the overall solution.

Because the PDF-averaged reaction rates are averaged over fuel mixture fraction and fuel reaction progress space, errors can arise in the PDF-averaging near the limit of $\theta = 1$. This is because of the equilibrium profile assumed for the PDF-integration. For fuel-rich conditions, $Y_{oxidizer\,eq} \approx 0$ and for fuel-lean conditions $Y_{fuel_{eq}} \approx 0$. Thus, the fuel reaction rate can prematurely approach zero. These same errors occur near $\theta = 0$ but don't pose nearly the same problem due to the fact that before the fuel has reacted the other species in the global mechanism are typically dormant. The PDF-averaged fuel reaction rate should never dip below the laminar reaction rate in the post-flame region. Therefore, in the solution procedure, when $\theta > 0.5$ then the fuel-step reaction rate is treated as such:

$$\tilde{r}_f = (1-\beta)\,\tilde{r}_{PDF} + \beta\,\tilde{r}_{la\,\min ar} \tag{47}$$

where

$$\beta = \max\left(\min\left(\left(\frac{\theta - 0.5}{1.0 - 0.5}\right),1\right),0\right) \tag{48}$$

This causes the PDF-averaged fuel rate to slowly transition to the laminar rates as fuel reaction progress approaches one. Doing so greatly enhances convergence.

For pure diffusion flame problems, the reaction progress is sometimes not well defined. This fact leads to difficulty in the implementation of Equation 47. Instead, to overcome the non-realistically low fuel PDF rates the following equation is used:

$$\tilde{r}_f = \max\left(\tilde{r}_{PDF}, \tilde{r}_{la\,\min ar}\right) \tag{49}$$

The species transport equations are solved via an implicit, linear point-solver method. The coupled species equations are solved at each computational cell. This technique leads to slow convergence but provides for a robust solution procedure.

The current species transport equation solution method employed by the multi-step PDF module in CFD-ACE+ is inadequate for large-scale simulations of combustion phenomena. As previously mentioned, the existing method for solving the species transport equations utilizes a cell-by-cell point solver. Specifically, the solver 'sweeps' over all of the computational cells in the domain solving the coupled species equations at each cell. In a sense, this method holds the solution values at all other cells constant while solving for the species fractions at a given cell. While adequate for small problems, large problems require a large number of iterations in order to assure global convergence. Steady-state problems can usually afford a large number of global iterations to achieve ample convergence. However, transient cases such as LES need to keep the number of global iteration per time step to a minimum if practical run times are to be realized.

The other variables in the CFD calculations are solved for sequentially using a field solution procedure. This method propagates boundary conditions through the solution domain very efficiently and is the standard approach for most CFD calculations. Enthalpy is solved for in this fashion and significant problems have been seen with the coupling of the species (solved for using the point solver) and enthalpy. Adopting this same strategy for the species solution is a plausible approach to achieve good coupling of the enthalpy and species and was tested. In this

approach, a given species was solved over the entire computational domain while holding all the other species constant. The remaining species were then solved for in turn in a likewise manner. This procedure has the benefit of fast propagation of boundary information. However, species are highly coupled and exhibit nonlinear behavior and solutions using this methodology rarely converge.

The solution to this problem would be to modify the solver to allow for a field solution of the coupled species equations. Instead of solving for species 1 while holding species 2, 3, 4, etc. constant, all of the species would be solved simultaneously over the entire field. In the CFD-ACE+ solver, this would necessitate that the field solver handle more than current limitation of solving for only one dependent variable at a time. Using such a coupled field solution, better coupling to other flow variables, such as enthalpy, is possible. This occurs because the species information will propagate at the same rate as the enthalpy information. Also, the species will remain implicitly coupled at each cell. This solution procedure will implicitly will require more CPU time per iteration, but will converge in a fewer number of iterations. However, the implementing this in CFD-ACE+ was beyond the scope of the present Phase II effort.

3.2.2 Table Look-Up

The calculation of PDF averaged species' chemical source terms with multi-step chemistry is extremely expensive. A table allows the integrated specific volume, temperature, and reaction rates to be stored as a function of θ, ξ, σ_θ, σ_ξ, enthalpy, and η. To improve computational efficiency, this data is first calculated and stored for subsequent table look-up. CFDRC has evaluated several table lookup schemes for applicability with the implemented multi-step PDF combustion model. Originally the in-situ tabulation method (ISAT), based on the work of Pope (1997), was proposed to represent compositions that are accessed during the simulation without requiring storage for unneeded compositions. For laminar flames, as chemical species evolve through composition space along low-dimensional manifolds, table values are needed for only a fraction of the allowed composition space. Thus, a lot of storage space is not required. However, for turbulent combustion calculations, the PDF averaged chemical source terms have a huge memory requirement. The PDF for turbulent combustion calculations is defined by the mixture fraction, mixture fraction variance, reaction progress variable, reaction progress variable variance, enthalpy and ratio of dynamic to equilibrium CO composition. Problems with ISAT were also encountered during LES calculations, due to the resolution of the large-scale fluctuations. The fluctuations created a large number of potential points in the ISAT table and prevented a high level of table retrievals versus direct integrations. For the assumed PDF approach developed in the SBIR for turbulent combustion calculations using both RANS and LES, the ISAT approach did not provide significant benefits as far as memory requirements and computational speedup are concerned. Instead, the relative expensive data search and extrapolation during the data retrieval process made ISAT time consuming.

In this project, an alternative table look-up approach using an in-situ procedure has been implemented. A table outline is created in a pre-processing stage with grid points covering the entire composition space. The interval spacing can be either even or variable. Data at the needed table points is then computed and stored as needed during the simulation. In this way, only chemistry data pertinent to the simulation is calculated. Initial iterations are slow, but retrieval rates approach 100% as convergence is achieved. During the simulation process, chemical

reaction information for each species at each cell can be obtained by checking the information corresponding to the cell and its neighboring cells in the table. This procedure is simpler than the ISAT framework and achieves similar results in speeding computation times. LES calculations especially benefit from this table approach, with retrieval rates approaching 100% after a limit-cycle condition has been reached.

3.3 Improved LES Inflow Boundary Conditions

One significant problem encountered in LES modeling of turbulent flow is the specification of the inflow boundary conditions. For simulations that inherently generate a great deal of turbulence, specification of the inflow boundary condition turbulence levels is not that critical, as the flow will generate its own turbulence. However, to capture flow features that depend on the free-stream turbulence, such as flow separation and boundary layer transition, improved boundary conditions are needed. Research has shown that application of random turbulence at the inlet does not capture the relevant length and time scales of the flow (Schlüter, 2002). The standard approach is to specify a random inlet condition for each time to give the right values of turbulent fluctuations based on some estimated turbulent kinetic energy. This is the traditional, and simplest way, to handle specification of turbulent energy at the inlet boundary condition. However, the structures introduced with this approach are small scale (on the order of the grid size) and tend to dissipate very quickly, with the end result being nearly identical to a laminar flow boundary. Several improvements to the LES modeling capabilities with respect to inlet boundary conditions in CFD-ACE+ were completed. Two new approaches have been implement to provide inlets with a more representative turbulent flow.

The first approach generates a random inlet correlated to a specified length scale using an approach similar to that of Klein et al (2003). This method gives the user control of the eddy size at the boundary but does not allow for a range of sizes. Therefore, some development length is still needed to allow the flow to generate the full length of length and time scales. The second method is to simulate the inlet turbulence via an auxiliary solution of the upstream region, utilizing periodic boundary conditions. The resulting periodic outflow boundary condition profile can then be read into the downstream simulation as an inflow boundary condition. This approach provides the full range of length and time scales at the inlet boundary, but only works in cases where a simple channel flow can be defined to characterize the inlet and is not valid for complex geometries or for inlets with swirl.

The boundary conditions were tested using a channel flow between two parallel plates. Figure 15 shows the geometry used for the simulations, along with the corresponding grid. The top and bottom boundary conditions are that of walls, while the sides are simulated as periodic.

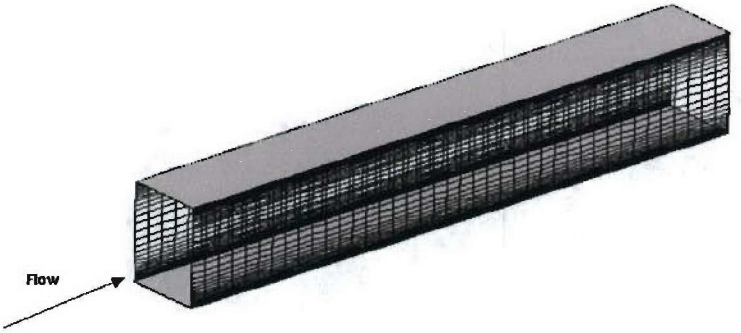

Figure 15. Geometry and Grid for Channel Flow Between Two Parallel Plates

If the inlet and outlet boundaries are taken to be periodic, then the fully developed turbulent flow structure shown in Figure 16 results. The contours shown in Figure 16 are of axial velocity in the center of the channel in between the top and bottom walls. Figure 17 shows the axial velocity at an instant in time at the periodic inflow plane. The inlet velocity fluctuations tend to be distributed randomly in space, but there is a definite range of eddy sizes in the simulations. Also, the approximate eddy length scales at the inlet can be determined. The largest eddy is no larger than ~ 1/3 of the channel height.

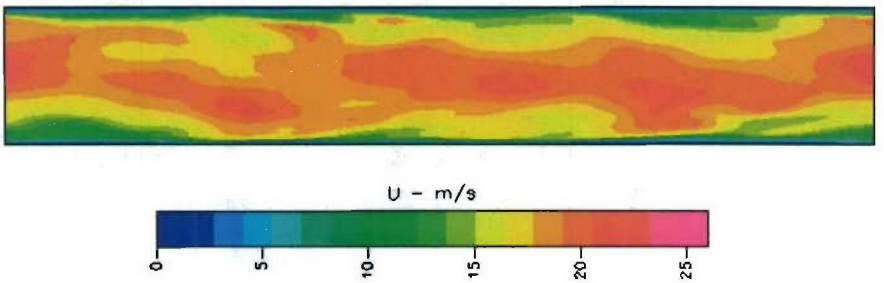

Figure 16. Turbulent Flow Structures for Axial Velocity in Channel Flow Between Two Parallel Plates Utilizing Periodic Inlet-Outlet Boundary Conditions

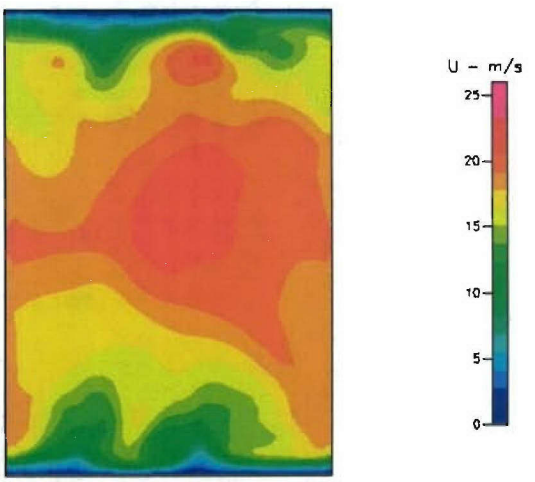

Figure 17. Inlet Axial-Velocity Profiles for Periodic Inlet-Outlet Simulation of Flow Between Two Parallel Plates

3.3.1 Correlated Random Inlet (CRI)

Turbulence has always been characterized with randomness in the flow, so historically most of the Large Eddy Simulations were performed by specifying a mean flow and a random fluctuation over the mean. In this approach (referred to as Gaussian random), no correlation between adjacent cells is assumed. Although the turbulent flows have a degree of randomness associated with them, it has been observed that the fluctuations are not completely random and that a three-dimensional correlation exists between the fluctuations. The difference between the spatially correlated boundary and a Gaussian random boundary is that the random number set used to characterize the velocity fluctuations are related to their neighboring cell values and also to their neighboring temporal values.

To enhance the existing capabilities of CFD-ACE+, three-dimensional correlations between the velocity fluctuations were specified at the inlet boundary for Large Eddy Simulations. For simplicity and low computational cost, a simple auto-correlation function derived from the assumption of homogenous turbulence (Batchelor, 1953) was used. The shape of this auto-correlation function is:

$$R_{uu}(r) = \exp\left(-\frac{\pi r^2}{4L^2}\right) \tag{50}$$

This functional dependence fulfills some basic properties like $R_{uu}(0) = 1$ and $\lim_{r\to\infty} R_{uu}(r) = 0$. The Length scale '$L$' for the turbulent flow has to be specified at the inlet boundary. This scale determines the eddy size observed at the inlet of the computational domain.

In order to specify three-dimensional velocity correlations at a two-dimensional inlet boundary, the flow velocities were time-correlated based on the fluctuation magnitude and eddy size specified at the inlet, as follows:

$$t_{eddy} = \frac{L_{eddy}}{u'} \tag{51}$$

Here, t_{eddy} represents the time for which the fluctuations are correlated at the inlet, L_{eddy} is the eddy size at the inlet and u' is the fluctuation magnitude at the inlet.

The computational procedure involved generating a set of random numbers for the whole inlet boundary faces and specifying the random velocity fluctuation for every computational face by averaging over the random numbers of adjacent faces lying within the range determined by the eddy size. The averaging was done by taking the convolution of the auto-correlation function and the random numbers. As the specified eddy size becomes small (less then the grid cell dimension) the method defaults to the Gaussian random inlet.

Profiles showing inflow data determined via a Gaussian random and three different specified length scales are shown in Figure 18. For the correlated random inlet (CRI), the user specified eddy length scales are 0.1, 0.3, and 2.0 m. The channel height is 2.0 m and the width is 1.0m.

The correlation between neighboring cells needed to produce coherent fluctuations at the eddy size are immediately apparent. In the Gaussian random approach, the velocity fluctuations at each boundary cell are independent and the largest eddy sizes are very small. Equally important, these fluctuations randomly vary at each time step and are not correlated from one time step to another. This results in very high frequency fluctuations at the inlet, which decay very rapidly.

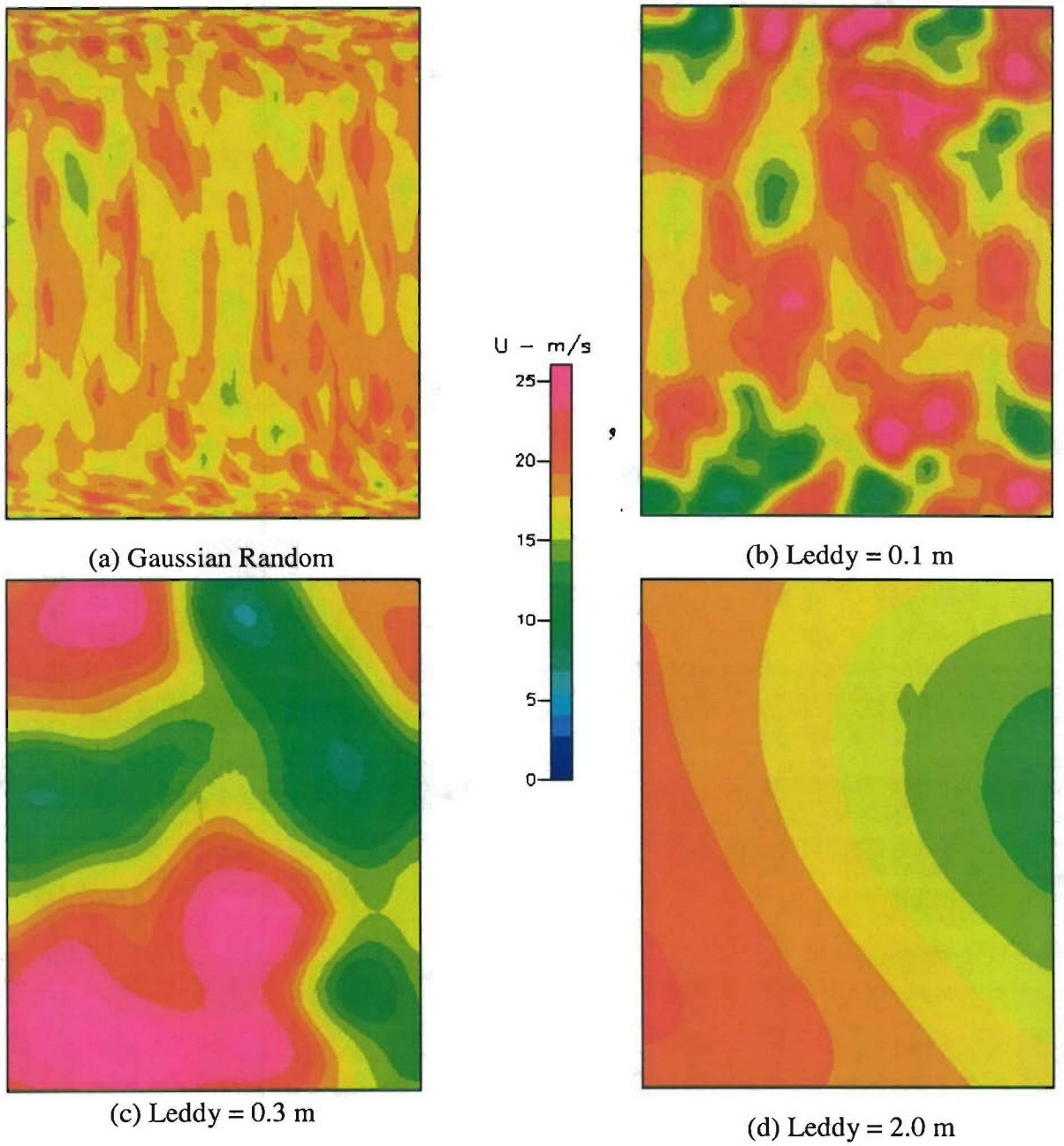

Figure 18. Inlet Axial-Velocity Profiles Showing Spatial Correlation for the Gaussian Random and SCI Boundaries

As shown in Figure 18, as the user specified eddy size increases, the eddy size at the inlet increases. Comparing the images to that shown in Figure 17 for the periodic case, an eddy size of 0.3 m seems to most resemble the inlet profiles. An eddy size of 0.1 m yields too many small scale eddies and no large scale eddies. With an eddy size of 2.0 m, the size of the channel height, the entire inlet is one eddy and the result is similar to RANS. In addition to being spatially correlated, the inlet profiles of Figure 18 are also temporally correlated. Temporal correlation is accomplished through the application of Taylor's hypothesis to relate the length and time scales. The time scale is equal to the specified length scale divided by the mean velocity.

The developed flow along the length of the channel was computed for the Gaussian random and CRI eddy sizes of 0.1 and 0.3 m. These results are shown in Figure 19. In the Gaussian random case fluctuations at the inlet quickly die out. The flow further downstream is nearly void of any turbulent flow structure and rapidly laminarizing.

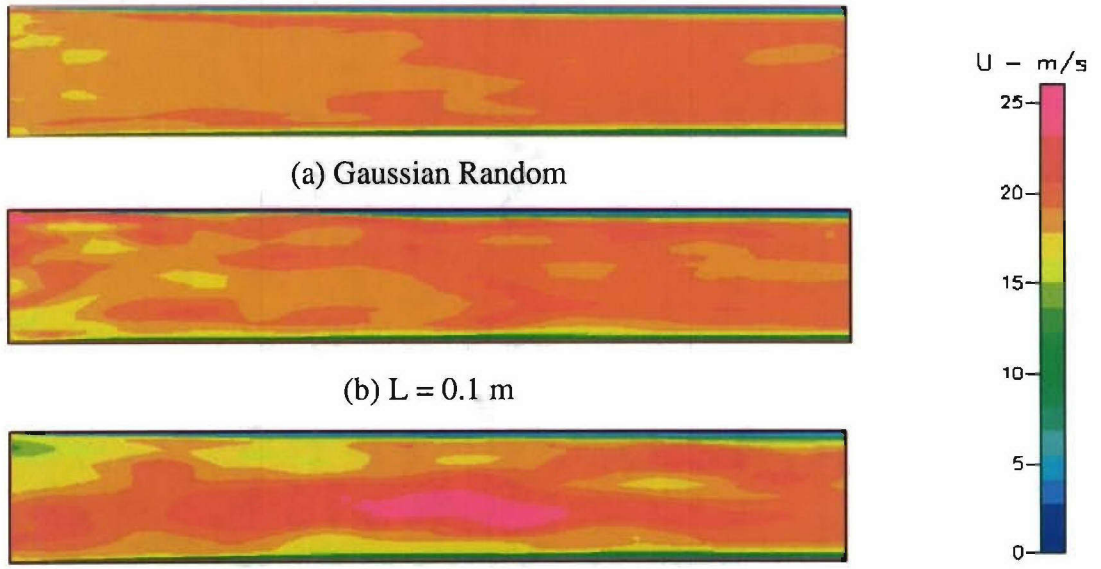

Figure 19. Turbulent Flow Structures for Axial Velocity in Channel Flow Between Two Parallel Plates Utilizing a Gaussian Random Method for Generation of Inflow Boundary Condition Data

With a specified eddy size of 0.1, there is a significant development region near the inlet where the small eddies dissipate. However it appears that larger eddies are forming downstream and that with a sufficiently long development length, a fully turbulent flow profile would result. A long development length is necessary because the specified size of 0.1 m was too small in comparison to the fully developed flow modeled by the periodic inlet-outlet simulation. With a specified inlet eddy size of 0.3 m, the development region near the inlet is much smaller than that for an eddy size of 0.1 m. The flow appears to be rapidly approaching the results shown in Figure 10 for the periodic inlet-outlet simulation.

In summary, the Gaussian random inlet is very easy to implement and has traditionally been used as the inflow method of choice. The main problem with the Gaussian random inlet is that the fluctuations generated are not correlated in spatially. The eddy sizes are determined by the grid and thus, the fluctuations do not represent true turbulent flow. These small scale fluctuations rapidly dissipate downstream of the inlet, basically resulting in laminar inlet flow.

The correlated random inlet method's strength is that the inlet eddies are not just random, but are correlated in both time and space to provide more realistic turbulent profiles. The method is also a very inexpensive calculation, and can be used for swirl inlets and inlets with complex geometry. A disadvantage of this method is that the user needs to know the eddy length scales at the inlet *a priori*. In addition, there will exist a development region downstream of the inlet as the flow develops the full range of eddy sizes.

3.3.2 Auxiliary Simulation

The second method for defining an LES boundary is to read in the boundary condition profile at each time step from an upstream, auxiliary solution using periodic boundary conditions. In the generation of inflow data from an auxiliary upstream periodic inlet-outlet solution, there are two elements that make it possible to use these results as downstream inflow boundary conditions. The first is interpolation. This allows the auxiliary solution grid to be different from the grid that the generated inflow boundary condition information is to be applied to. In the CFD-ACE+ algorithm, the interpolation scheme consists of locating the four closest nodes and computing a weighting factor based on how far away the nodes are from the desired location. The weighting factor is the inverse of the distance away from the desired location, normalized by the inverse of the sum of all four distances. The weighting factors sum to one. The value of the dependent variable at the desired location is computed as the sum of the product of the weighting factor and the dependent variable for the four closest nodes.

The second element that makes it possible to use an auxiliary upstream periodic inlet-outlet solution for a downstream inflow boundary condition is windowing. Windowing makes it possible to use a data set consisting of a limited number of frames (velocity profiles at each time step) over and over at the inlet without discontinuities occurring when the cycle repeats itself. For example, the auxiliary solution might generate two flow through times worth of data. The downstream simulation then needs to be able to use these results to simulate ten flow through times in the actual simulation. The inflow data will then be repeated five times. The modified velocity at each time step is computed as

$$U(t) = U_0 + (U(t) - U_0)\sin\left(\pi \frac{f_n}{f_{tot}}\right) \tag{52}$$

where U(t) is the windowing modified velocity, U_0 is the velocity at the first frame of the inflow data, U(t) is the velocity at the nth frame of the inflow data, f_n is the number of frames used, and f_{tot} is the total number of frames in the data set. Using this relationship leads to a smooth transition of the velocities from the end of the windowing frames to the beginning of the next repeat of inflow data while preserving the length and time scales associated with the original data set.

Figure 20 shows the channel flow simulations using inlet and outlet boundaries, with the inlet boundary mapped from the periodic channel flow simulations. The velocities plotted in Figure 20 show a very similar turbulent flow structures as those shown in Figure 16. It is interesting to note that there is no development region for the flow near the inlet. This is as expected, since the inlet boundary condition information was obtained from a similar simulation performed with periodic inlet-outlet boundary conditions.

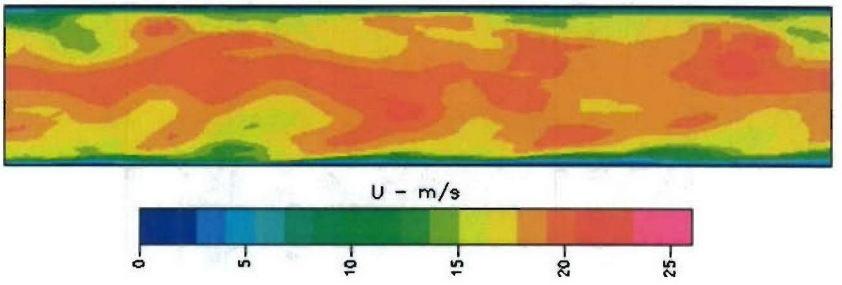

Figure 20. Turbulent Flow Structures for Axial Velocity in Channel Flow Between Two Parallel Plates Utilizing an Auxiliary Upstream Solution for Generation of Inflow Boundary Condition Data

The approach of using an auxiliary upstream simulation with periodic inflow-outflow boundary conditions to generate turbulent inlet profiles is a good way to get realistic turbulence at the inlet where the inlet geometry is such that a channel flow can be specified. There is no development region at the inlet because the turbulence provided is representative of fully developed turbulent flow. The full range of eddy length scales are determined as part of the solution, thus requiring no *a priori* determination of the eddy size. In addition, the boundary solution can be interpolated onto different inlet meshes and still retain the turbulent flow structure. In theory it would be possible to use a generic upstream inflow boundary condition generator and then apply it to multiple different downstream geometries. A disadvantage of this approach is that it has the potential to be very expensive. A separate simulation must be preformed simply to get the boundary condition information for the real simulation of interest.

3.4 Global Mechanism Generation

An accurate reduced chemical kinetic mechanism is needed to adequately predict flame stabilization and pollutant formation in advanced combustors. Detailed chemical kinetic mechanisms for JP-8-type aviation fuels have been under development for some time (Dagaut *et al.*, 1994; Violi *et al.*, 2002; Mawid and Sekar, 2001) but are limited in their validation and application at high pressure (20-50 atm). The above cited mechanisms by Dagaut, Mawid and co-workers have been validated for ignition delay at atmospheric or low pressure conditions. Further work needs to be done to develop simplified reaction mechanisms that are valid at high pressure.

The use of these detailed chemical kinetic mechanisms for military fuels such as JP-8 is not practical in three-dimensional CFD codes at the present time. The impractical nature of using detailed mechanisms is largely due to the extremely high computational expense required to

integrate the stiff set of chemical kinetic equations. Development of computational procedures involving realistic kinetic mechanisms is needed, especially when accurate prediction of emissions is needed.

For practical CFD calculations, including those performed with the multi-step PDF model, a reduced set of global reactions (~ 5-10 steps for JP-8, including NO_x) that use simple Arrhenius expressions for each reaction rate is needed. In this SBIR program, CFDRC has developed a global multi-step mechanism for JP-8 applicable to gas turbine combustion simulations. Examples of the global mechanisms similar to what has been developed for JP-8 include the reaction mechanisms of Nichol *et al.* (1997), Dryer and Glassman (1973), Westbrook and Dryer (1984), and Jones and Lindstedt (1988). The Nichol 3-step mechanism for methane-air combustion is shown in Table 4.

Table 4. The Nichol (1995) Mechanism for CH_4

$CH_4 + \frac{3}{2}O_2 \Rightarrow CO + 2H_2O$	$R = 10^{11.61} \exp\left(\frac{-15866}{T}\right)[CH_4]^{0.95}[O_2]^{0.72}$
$CO + \frac{1}{2}O_2 \Rightarrow CO_2$	$R = 10^{14.00} \exp\left(\frac{-16811}{T}\right)[CO]^{1.61}[O_2]^{1.0}$
$CO_2 \Rightarrow CO + \frac{1}{2}O_2$	$R = 10^{4.69} \exp\left(\frac{-20773}{T}\right)[CO_2]^{1.09}$

The global mechanisms are very easy to use and cost effective, due to the simple Arrhenius rate expressions (see equation 25). However, the mechanisms are often only applicable at or near the conditions where the experimental data used in determining the Arrhenius rates were collected In order to more accurately predict species and temperature profiles in practical CFD simulations, global multi-step mechanisms with Arrhenius rates have been developed in this Phase II effort. CFDRC has implemented a computational tool to automatically generate the multi-step global mechanism and Arrhenius rates specifically for each simulated flow condition.

$$r = A \cdot T^n P^m e^{\frac{-E_a}{RT}} [C_1]^{a_1} [C_2]^{a_2} \tag{53}$$

Global mechanisms using standard Arrhenius rates have several significant advantages. With Arrhenius rates, the source terms can be directly evaluated and the solution of a separate set of equations is not required. Also, linearization of reaction rate source terms for CFD codes is very simple with Arrhenius rates (shown in Equation 4), since an analytic derivation of the reaction rate is easily formed. In multi-step mechanisms, steps include the fuel oxidation step to CO, along with one more CO oxidation step. Other steps accounting for NO_x, or other minor species, can be added if needed. Also, if unburned hydrocarbons or smoke calculations are required, fuel intermediates may be included. The coefficients in the Arrhenius rate expressions are determined through curve fitting to experimental data.

3.4.1 Approach

The approach that CFDRC is following in this SBIR program utilizes zero- and one-dimensional flow calculations with a detailed kinetic mechanism. Examples are Perfectly Stirred Reactor (PSR), Plug Flow Reactor (PFR), and laminar one-dimensional premixed flame calculations. Detailed kinetics are used in these models to determine temperature and species profiles as a function of either residence time or distance. An optimization routine (Steepest Descent method) is then used to fit global kinetic parameters that will match these profiles. Use of these approach to determine global kinetic parameters is commonly referred to as Chemical Reactor Modeling (CRM). Figure 21 shows a flow chart of this process. Under this SBIR, CFDRC has developed the capability to efficiently generate a reduced global mechanism with optimum Arrhenius rates, similar to that shown in Table 7, for a given set of conditions. The software is designed to automatically determine the optimum coefficients in the Arrhenius reaction rates based on CRM calculations using the full detailed mechanism. Nicol and Malte (1996) successfully used this type of approach on a limited basis

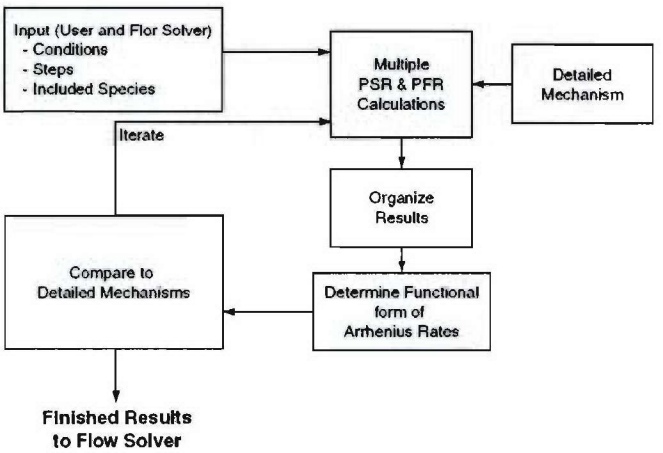

Figure 21. Flow Chart of the Process Used to Automatically Generate Reduced Global Mechanisms from Detailed Mechanisms

3.4.2 PSR-PFR Combinations

A gas turbine combustor can be represented by various combinations of perfectly-stirred reactors (PSR) and plug-flow reactors (PFR). This type of approach is frequently used to model complex combustion systems (Turns, 2000) and has been coined "chemical reactor modeling", or CRM. One possible configuration is a PSR followed by a PFR, as was used by Nicol (1995). Figure 22 shows this configuration.

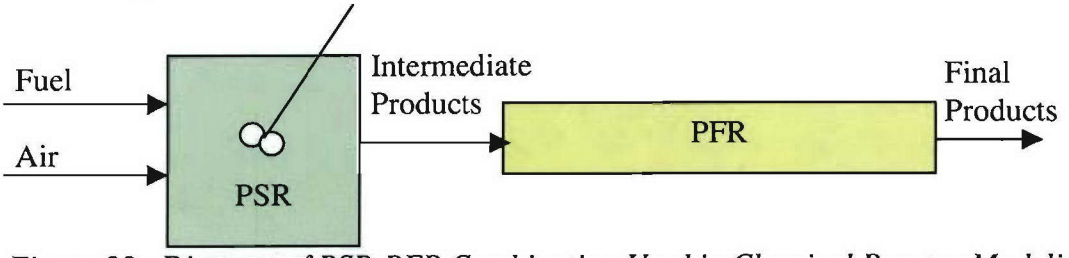

Figure 22. Diagram of PSR-PFR Combination Used in Chemical Reactor Modeling

The PSR is well mixed, and has not yet approached equilibrium. This stage represents the primary zone of the combustor, where good recirculation enhances the mixed-ness. The PFR is

representative of the secondary and dilution zones where mixing is not as strong and the kinetics approach equilibrium. In the PSR, the fuel reacts mainly to CO; while in the PFR section, the CO is slowly oxidized to CO_2. Although this type of PSR-PFR combination is a simplistic representation of the complexities of gas turbine combustion, it is very amenable to detailed kinetic modeling. Multidimensional, high fidelity CFD models, while accurately capturing the relevant flow patterns, are not equipped to handle the coupling of detailed kinetic calculations.

One use for CRM is to generate rate parameters for simple multi-step global mechanisms with Arrhenius rates that can then be used in CFD models for gas turbines. The first step in the approach for obtaining global Arrhenius rate parameters is to perform CRM using a detailed mechanism. The detailed calculations were performed in the PSR and PFR combination, and the species net production rates are generated as a function of reactor residence time. The generation of these production rates can be performed for single or multiple equivalence ratios, at a given inlet temperature, and for a given operating pressure.

Cantera, an open source code for modeling chemical reactions developed by David Goodwin (2004), was used as the method of choice for obtaining the PSR-PFR results. The PSR calculations were performed at a residence time just above the blow-out residence time. This was determined in Cantera by systematically reducing the residence time to the point where if lowered any further, reactions cease to occur. This is known as the blow-out residence time. The blow-out residence time is used for the PSR for two reasons. First, running the PSR just above the blow-out condition allows for the largest possible temperature range and thus makes the global mechanism valid over this temperature range. Secondly, at the blow-out residence time the CO fraction is near its peak value, thus providing a good range of CO concentration over which to fit the global mechanism.

The PFR calculations were initiated using the exit conditions of the PSR calculation. The PFR was then allowed to react over a range of residence times that approached equilibrium. Results, consisting of temperature, species net production rates, and species concentrations, are recorded over the range of residence times and again over the range of equivalence ratios involved.

Next, the temperature and species concentrations at each residence time are used with the global mechanism to determine the net production rates predicted by the global mechanism. Throughout the PSR-PFR combination, temperature and species concentrations are varying, thus providing a wide range of parameters over which the global net production rates are calculated.

The goal is then to match the globally computed production rates with the production rates predicted by the detailed mechanism. Therefore, the difference between the global rates and the detailed rates needs to be minimized. Standard optimization techniques (namely the steepest descent method) are used to minimize the error by varying the global Arrhenius rate parameters. This optimization routine has been embedded in the routines for computing the PSR-PFR results.

Although the rates may match very well, what is of real interest is the match between the species concentrations and temperature computed from the global mechanism for the same conditions used for the detailed mechanism calculations. To demonstrate applicability, the global

mechanism is then used to compute temperature and species profiles for the same PSR-PFR configuration.

In order to facilitate the computations of the global mechanism based PSR-PFR combination, a separate code was required that could deal with global mechanisms. This code was written using the PETSc solvers (Balay et al., 2001). The PSR equations were solved using a Newton-Raphson non-linear solve with pseudo time stepping. The PFR equations were solved also using a Newton-Raphson non-linear solve using the implicit backwards Euler method for time stepping. Cantera was used for the property calculations: enthalpy, density, mean molecular weight, etc.

Some examples of the types of mechanisms that can be generated are shown below, both for methane and JP-8. These examples aim to show the flexibility of the CRM approach and are not intended to be the only or even the best multi-step global mechanisms possible for these conditions. Using the newly developed CRM capabilities, mechanisms can easily be generated for any conditions of interest for both methane and kerosene fuels.

Methane 3-Step

A 3-step global mechanism was generated for methane oxidation. The GRI-3.0 mechanism, consisting of 53 species and 325 reactions, was used for the detailed kinetic calculations. The 3-step global mechanism is of the same form as that of Westbrook and Dryer (1984). The optimized Arrhenius parameters are shown in Table 5. These parameters are valid over the equivalence ratio range of 0.6-1.0, an inlet temperature of 600 K, and an operating pressure of 1 atm.

Table 5. Optimized Arrhenius Rate Parameters for a Global 3-step Methane Oxidation Mechanism

$CH_4 + \frac{3}{2}O_2 \Rightarrow CO + 2H_2O$	$R_1 = 7.2\times10^{10} T^{0.177} \exp\left(\frac{-19172}{T}\right)[CH_4]^{0.6662}[O_2]^{0.74463}$
$CO + \frac{1}{2}O_2 \Rightarrow CO_2$	$R_2 = 3.9\times10^{11} T^{0.063} \exp\left(\frac{-9771}{T}\right)[CO]^{1.6023}[O_2]^{0.8870}$
$CO_2 \Rightarrow CO + \frac{1}{2}O_2$	$R_3 = 1.8\times10^{6} T^{-0.121} \exp\left(\frac{-15852}{T}\right)[CO_2]^{1.1192}$

The comparison of the detailed net production and global net production at the equivalence ratio of 0.6 is shown below, Figure 23, as a function of reactor residence time. The initial point is determined from the PSR calculation. The remaining points are from the PFR simulation. The global mechanism does a remarkably good job in approximating the net production rates for the species involved.

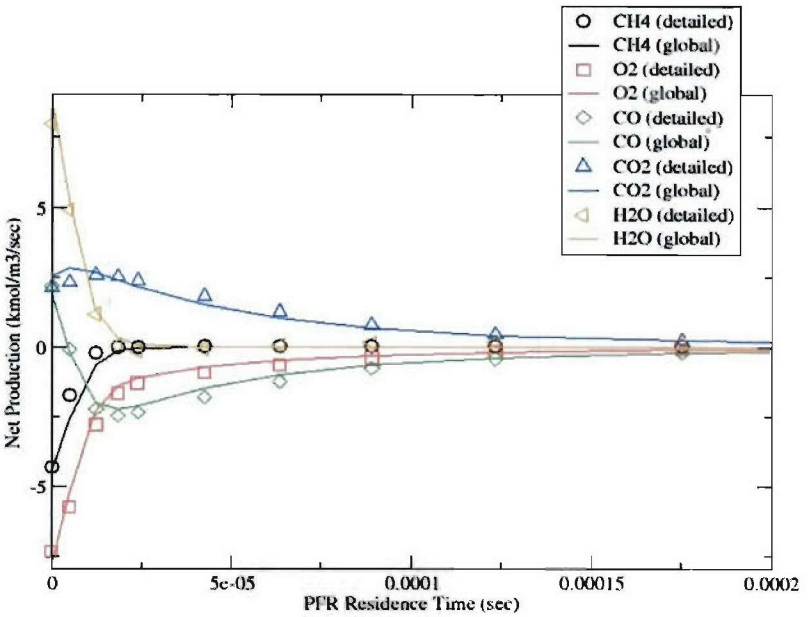

Figure 23. Comparisons of Predictions in Net Species Productions for Detailed and Global Mechanisms

Additionally, the temperature and species mole fractions predicted by the global mechanism are compared to those calculated via the detailed mechanism. Figures 24 and 25 show these comparisons. It can be seen that initially, the temperature is slightly higher for the global mechanism at the exit of the PSR. However, the temperature quickly approaches that of the detailed mechanism. The species concentrations are captured fairly accurately except for a slight offset, which is most likely due to the limited amount of species contained in the global mechanism. Water, in particular, seems to deviate from the detailed calculation. Most likely a global mechanism involving more steps would be needed to accurately predict the water mole fraction.

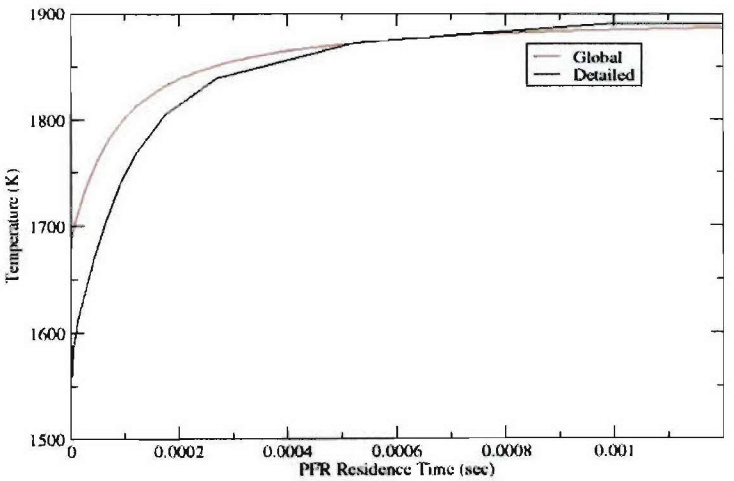

Figure 24. Comparison of Temperature and Species Profiles Computed via Global and Detailed Mechanisms for ϕ=0.6, T_{in}=600 K, P=1 atm, and a PSR Residence Time of 0.1 msec

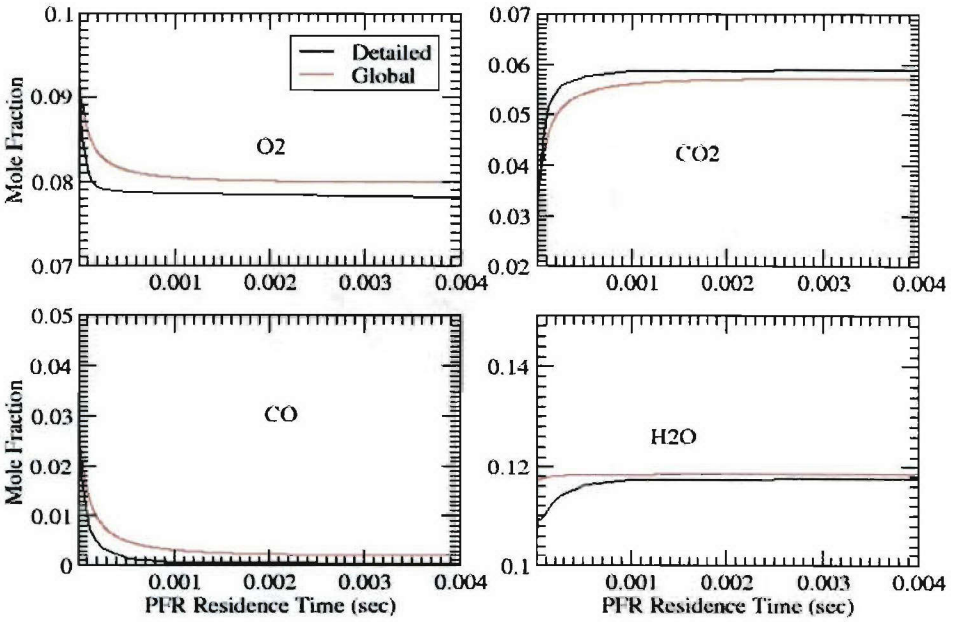

Figure 25. Comparison of Species Profiles Computed via Global and Detailed Mechanisms for ϕ=0.6, T_{in}=600K, P=1 atm, and a PSR Residence Time of 0.1 msec

JP-8 5-Step

A detailed mechanism for JP-8 combustion which consisted of 200 species and 1345 reactions was used for the detailed kinetic calculations. From this detailed mechanism, two 5-step global mechanisms were generated for JP-8 combustion (Tables 6 and 7). Both involve an intermediary step containing H_2. The first mechanism (Table 6) utilizes the water-gas shift reaction. The second mechanism (Table 7) involves $C_{12}H_{23}$ being oxidized to CO and H_2. CO and H_2 then are further oxidized by O_2 in steps 2 and 3. The rate parameters for both mechanisms are shown below in the table.

Table 6. Global 5-Step Mechanism for $C_{12}H_{23}$ Combustion Using a Water-Gas Shift Reaction

$C_{12}H_{23} + 6O_2 \Rightarrow 12CO + 11.5H_2$	$R_1 = 3.24\times10^{12} T^{0.100} \exp\left(\frac{-14798}{T}\right)[CH_4]^{1.043}[O_2]^{0.872}$
$CO + H_2O \Rightarrow CO_2 + H_2$	$R_2 = 3.3\times10^{6} T^{0.-0.09} \exp\left(\frac{-4242}{T}\right)[CO]^{0.666}[O_2]^{0.730}$
$CO_2 + H_2 \Rightarrow CO + H_2O$	$R_3 = 7.01\times10^{7} T^{0.148} \exp\left(\frac{-15641}{T}\right)[CO_2]^{0.774}[H_2]^{0.542}$
$H_2 + \frac{1}{2}O_2 \Rightarrow H_2O$	$R_4 = 7.08\times10^{12} T^{-0.039} \exp\left(\frac{-4446}{T}\right)[H_2]^{1.462}[O_2]^{1.401}$
$H_2O \Rightarrow H_2 + \frac{1}{2}O_2$	$R_5 = 1.57\times10^{6} T^{-0.132} \exp\left(\frac{-15470}{T}\right)[H_2O]^{1.119}$

Table 7. Global 5-Step Mechanism for $C_{12}H_{23}$ Combustion Using a CO Oxidation Step

$C_{12}H_{23} + 6O_2 \Rightarrow 12CO + 11.5H_2$	$R_1 = 6.44\times10^{11} T^{0.075} \exp\left(\frac{-13593}{T}\right)[CH_4]^{0.941}[O_2]^{0.930}$
$CO + \frac{1}{2}O_2 \Rightarrow CO_2$	$R_2 = 3.76\times10^{11} T^{-0.040} \exp\left(\frac{-7955}{T}\right)[CO]^{1.392}[O_2]^{1.240}$
$CO_2 \Rightarrow CO + \frac{1}{2}O_2$	$R_3 = 1.72\times10^{6} T^{-0.136} \exp\left(\frac{-15236}{T}\right)[CO_2]^{1.117}$
$H_2 + \frac{1}{2}O_2 \Rightarrow H_2O$	$R_4 = 5.75\times10^{13} T^{-0.065} \exp\left(\frac{750}{T}\right)[H_2]^{1.903}[O_2]^{1.505}$
$H_2O \Rightarrow H_2 + \frac{1}{2}O_2$	$R_5 = 5.00\times10^{5} T^{-0.172} \exp\left(\frac{-15564}{T}\right)[H_2O]^{1.154}$

Both mechanisms were curve fit over the equivalence ratio range of 0.6-1.0, a pressure of 1 atm, and an inlet temperature of 600 K. Comparisons between the net species production rates predicted by the two mechanisms at an equivalence ratio of 0.6 are shown in Figures 26 and 27. From these figures, it can be seen that the second mechanism, the one not involving the water-gas shift reaction, seems to better approximate the rates computed from the detailed mechanisms. However, the first mechanism approximates the formation of water more accurately. Overall, good agreement is shown between the detailed and global mechanisms.

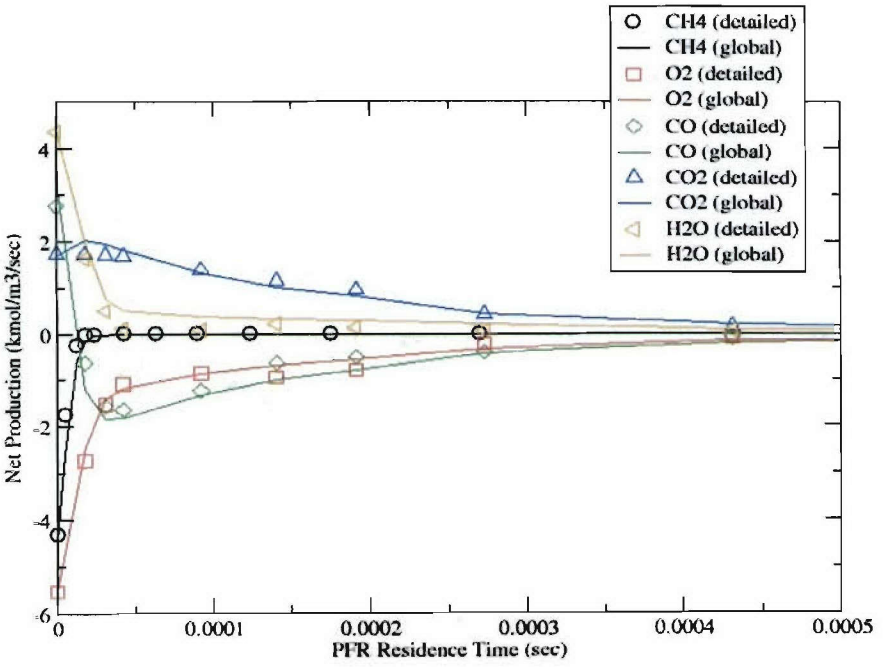

Figure 26. Species Net Production Comparisons for Detailed and Global Mechanism (Mechanism 1) Calculations

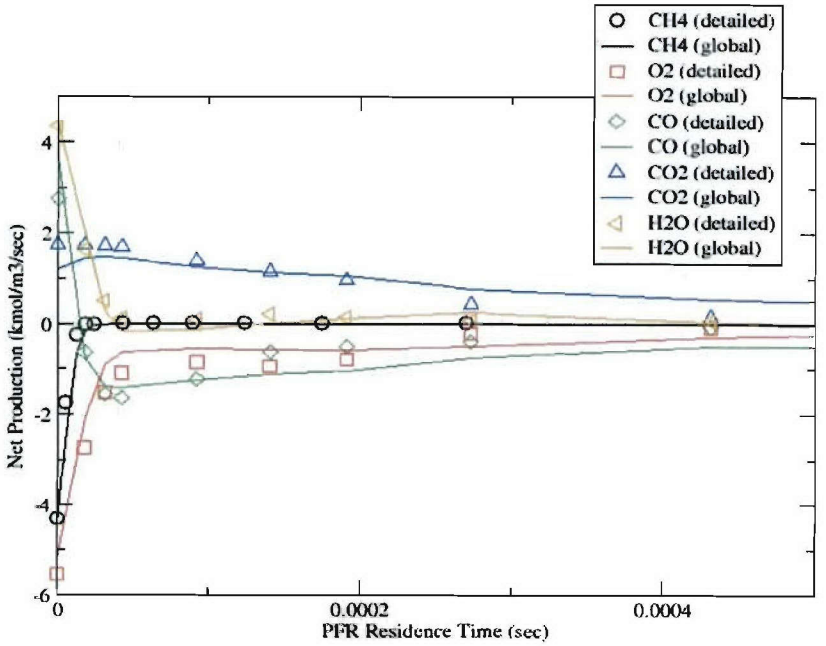

Figure 27. Species Net Production Comparisons for Detailed and Global Mechanism (Mechanism 2) Calculations

One drawback of this approach for determining the Arrhenius parameters is that matching the species net production rates does not necessarily mean that the temperature profile, nor the species concentrations will match. An improvement on this algorithm would be to minimize the difference between the temperature and species concentrations computed from the detailed and global mechanisms. Thus, the net production rates would not match, but the quantities of interest would. This type of optimization is much more involved however, as it requires performing PSR-PFR calculations with the global mechanism at each iteration of the optimization solver.

3.4.3 Laminar One-Dimensional Flame Calculations

Another approach to obtaining global rate parameters is to use detailed, laminar, one-dimensional, freely-propagating flame calculations. This approach avoids several drawbacks of the PSR-PFR approach. Namely, the PSR-PFR approach 'ignores' the temperature range from the inlet temperature to the PSR temperature. Typically, this is a temperature range in excess of 1000 K. Secondly, the PSR-PFR approach doesn't guarantee that the laminar flame speed will be accurately predicted. The laminar 1-D calculations cover the entire temperature range (i.e. inlet to equilibrium). Also, the laminar flame speed is inherent in the calculation.

There are several steps involved in obtaining global rates from detailed 1-D laminar calculations. These are (1) solve the 1-D freely propagating flame using the detailed kinetic mechanism, (2) select and assemble data that is to be fit against, and (3) perform optimization of Arrhenius parameters using the global mechanism in the 1-D calculation. Each of these steps will be discussed in detail.

First, the 1-D freely propagating flame is solved with Cantera. The detailed mechanism is used in this calculation. This involves an iterative process of finding the inlet velocity at which the

flame detaches from the inlet and moves downstream and sets up a stable flame with zero temperature gradients on either side.

Second, the data (really the detailed mechanism results) desired to fit the global mechanism against needs to be assembled. This can be temperature, species (those that exist in the global mechanism) fractions, or species net production rates. Any combination of these can be used. For the PSR-PFR model discussed earlier, only species net production rates were used. For the current laminar 1-D calculations, temperature and species are used. However, any combination of temperature, species fractions, and/or species net production rates could be used.

Finally, the optimization is performed using initial guesses for the global rate parameters. A 1-D flame is computed via Cantera using these global kinetics. The 'wellness' of the fit is then calculated. For example, this could be the difference between the temperature profile calculated by the detailed mechanism and the global mechanism. The derivatives of this 'function' with respect to the Arrhenius parameters are then computed. This involves multiple 1-D flame calculations and can become very expensive for a large number of iterations. At each iteration, a new set of parameters that give a lower value of the fitting function are found. This procedure continues until the local minimum is reached, and at this point the optimum Arrhenius kinetic parameters for the global mechanism are found.

Methane 3-Step

To demonstrate this approach, a three-step global mechanism was developed for premixed methane combustion. The GRI-Mech 3.0 was used for the detailed mechanism. This mechanism consists of 53 species and 325 reactions. The global mechanism consisted of 5 species and 3 reaction steps. This mechanism was fit at the operating conditions of ϕ=1.0, T=300 K, and P=1.0 atm. The curve fit parameters are shown below.

Table 8. Global 3-Step Mechanism for Methane Combustion at ϕ=1.0, T=300 K, and P=1 atm

$2CH_4 + 3O_2 \Rightarrow 2CO + 4H_2O$	$R_1 = 4.57\times10^{9} T^{-0.119} \exp\left(\frac{-13226}{T}\right)[CH_4]^{0.5088}[O_2]^{0.9221}$
$2CO + O_2 \Rightarrow 2CO_2$	$R_2 = 3.73\times10^{11} T^{0.166} \exp\left(\frac{-12127}{T}\right)[CO]^{1.843}[O_2]^{0.9345}$
$2CO_2 \Rightarrow 2CO + O_2$	$R_3 = 6.12\times10^{5} T^{-0.352} \exp\left(\frac{-15519}{T}\right)[CO_2]^{0.9961}$

Plots of temperature and species comparisons are shown in Figures 28a and 28b, respectively. The global mechanism optimized via the laminar 1-D calculation matched the laminar flame speed almost exactly. The fitness of the optimization for this mechanism was based on the temperature profile only. Therefore, as shown in Figure 28a, the temperature profile fit is extremely good. As for the species profiles, the general trend is captured, but the dynamics of the species profiles are not captured very well.

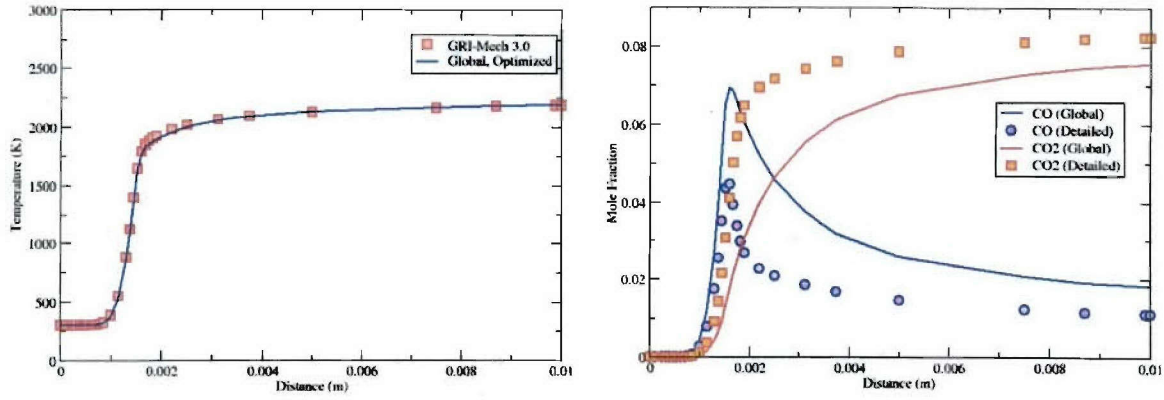

(a) (b)

Figure 28. (a) Temperature and (b) Species Plots Showing Comparisons Between Detailed and Global Calculations

In order to obtain a more accurate fit of the species profiles, another mechanism was generated. This time, the species profiles were included in the optimization. Weighting factors were applied to each fitted profile. Temperature had a weight of 1, CO had a weight of 0.2, and CO_2 had a weight of 0.02. The resulting mechanism is shown below in Table 9. It is worth noting that this mechanism and the previous mechanism only differ slightly. This illustrates how sensitive the solution is to the kinetic parameters.

Table 9. Global 3-Step Mechanism for Methane Combustion at ϕ=1.0, T=300 K, and P=1 atm

$2CH_4 + 3O_2 \Rightarrow 2CO + 4H_2O$	$R_1 = 4.56\times10^{9} T^{-0.0711} \exp\left(\frac{-14014}{T}\right)[CH_4]^{0.5819}[O_2]^{0.9223}$
$2CO + O_2 \Rightarrow 2CO_2$	$R_2 = 3.78\times10^{11} T^{0.221} \exp\left(\frac{-9231}{T}\right)[CO]^{1.822}[O_2]^{0.9280}$
$2CO_2 \Rightarrow 2CO + O_2$	$R_3 = 6.07\times10^{5} T^{-0.108} \exp\left(\frac{-15702}{T}\right)[CO_2]^{1.073}$

Comparisons of temperature and species profiles are shown below in Figures 29a and 29b, respectively. The improvement in the species fit is dramatic. Now, the species profiles not only match the general trend, but also match the peaks and curvature. The sacrifice for this match is shown in the temperature profile. Whereas before the temperature profile matched almost perfectly, now there is a slight deviation downstream of the initial flame-front. Weighting allows the user to focus the profiles on the ones of most interest.

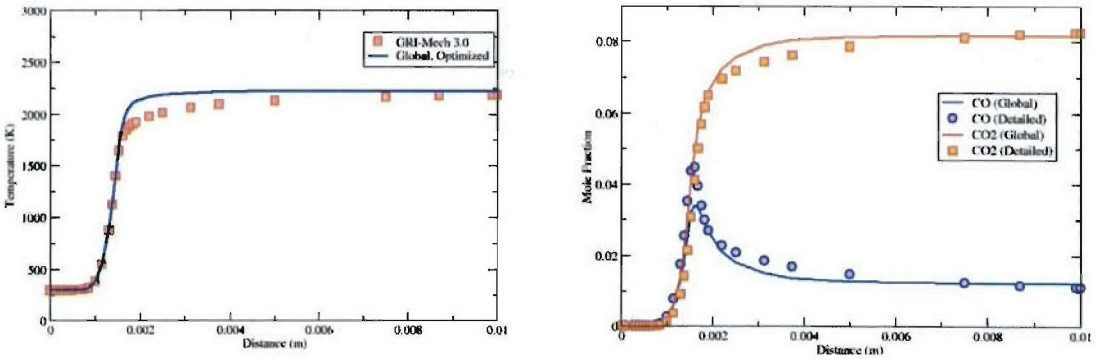

(a) (b)

Figure 29. (a) Temperature and (b) Species Plots Showing Comparisons Between DetaileD and Global Calculations

In addition to the mechanisms described above, any extension can be made. For example, if a global NO_x step is desired, it can be included and the mechanism can be re-optimized while applying the appropriate weighting factor for the NO_x profile. If intermediates, like OH or H, are desired then steps for these species can be included as well.

3.4.4 Opposed Diffusion Flame Calculations

The capability to compute global rate parameters from 1-D, laminar, opposed diffusion flame calculations has been implemented. This technique is similar to that for the 1-D laminar adiabatic flame. However, in this flame fuel enters from one side and oxidizer enters from the other. Figure 30 shows the general configuration of an opposed diffusion flame. The drawback of the freely propagating, laminar, adiabatic flame is that only one equivalence ratio is taken into account. This drawback is eliminated in the opposed diffusion flame. In this flame, the equivalence ratio goes from zero at the oxidizer inlet all the way to infinity at the fuel inlet. Thus, the entire range from fuel rich to fuel lean is covered.

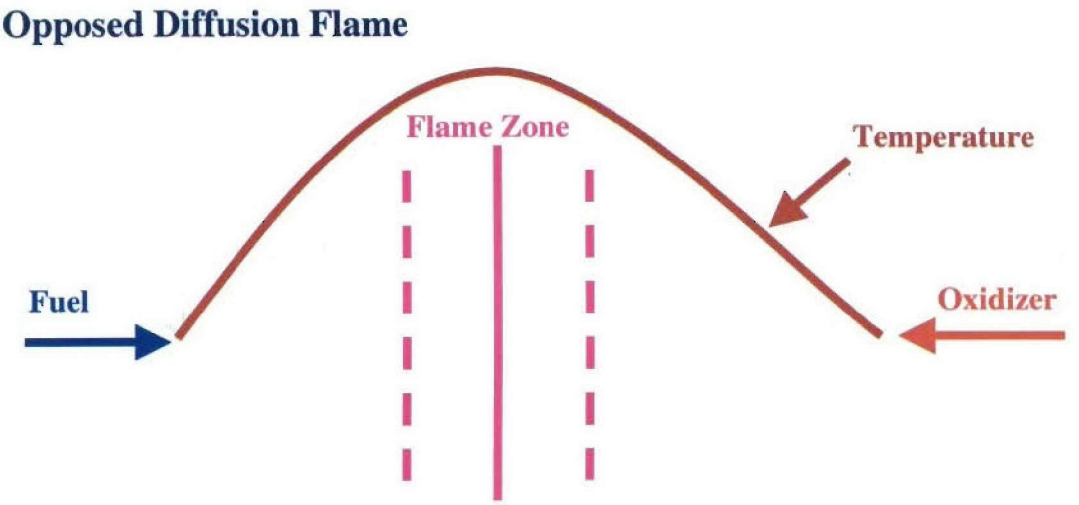

Figure 30. Schematic Of Opposed Diffusion Flame Configuration

Using opposed diffusion flame calculations, rate parameters for a 3-step, 6-species global mechanism were generated. Initially, the mechanism was fit to the species net production rates. The results are listed in Table 10. Finally, these rates were fit to the temperature and species profiles for a 1-D laminar opposed diffusion flame (Table 11).

Table 10. Intermediate Arrhenius Parameters Optimized On Species Net Production Rates

Reaction	A	β	Ea (J/kmol)	Reactant	Order	Reactant	Order
$2\ CH_4 + 3\ O_2 \Rightarrow 2\ CO + 4\ H_2O$	5.46E+10	0.413	1.80E+08	CH4	0.4080	O_2	1.305
$2\ CO + O_2 \Rightarrow 2\ CO_2$	9.96E+06	-0.203	1.11E+08	O_2	0.5356	CO	0.7947
$2\ CO_2 \Rightarrow 2\ CO + O_2$	1.84E+06	-0.121	1.78E+08	CO_2	0.5813		

Table 11. Arrhenius Parameters Optimized On Temperature And Species Profiles

Reaction	A	β	Ea (J/kmol)	Reactant	Order	Reactant	Order
$2\ CH_4 + 3\ O_2 \Rightarrow 2\ CO + 4\ H_2O$	3.51E+10	0.515	1.77E+08	CH_4	0.5662	O_2	1.263
$2\ CO + O_2 \Rightarrow 2\ CO_2$	8.24E+06	-0.005	1.01E+08	O_2	0.5338	CO	0.657
$2\ CO_2 \Rightarrow 2\ CO + O_2$	3.19E+06	-0.346	1.78E+08	CO_2	0.5460		

The intermediate rate parameters (Table 4) are remarkably close to the final ones (Table 5). This indicates that the rate parameters obtained from the species net production rates are a very good starting point for fitting to temperature and species profiles. The determination of the rate parameters in Table is a very inexpensive calculation (1-2 orders of magnitude less), whereas fitting to temperature and species profiles is a more costly calculation. Thus, by obtaining the rates in this two-step procedure the overall cost of computing the rate parameters is reduced.

Figures 31 to 33 show the results of the fitted global mechanism compared to the detailed mechanism predictions. Figure 31 shows the temperature comparisons, while Figures 32 and 33 compare species profiles. Other than a slight overshoot in the peak temperature, the match is very good. The species, especially CO and CO_2, match extremely well for such simplified chemistry.

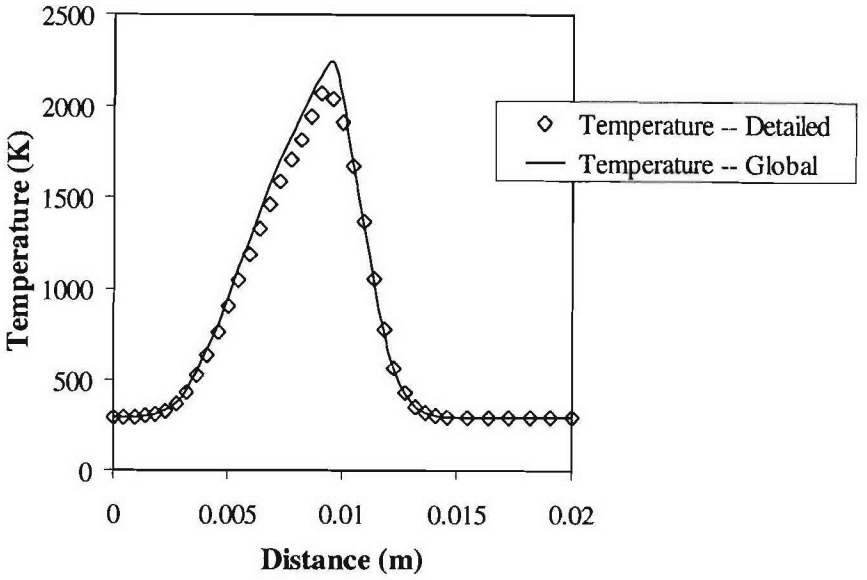

Figure 31. Temperature Profile For 1-D Opposing Diffusion Flame Using Fitted Global Rate Parameters Compared To The Detailed GRI-3.0 Mechanism Temperature Profile

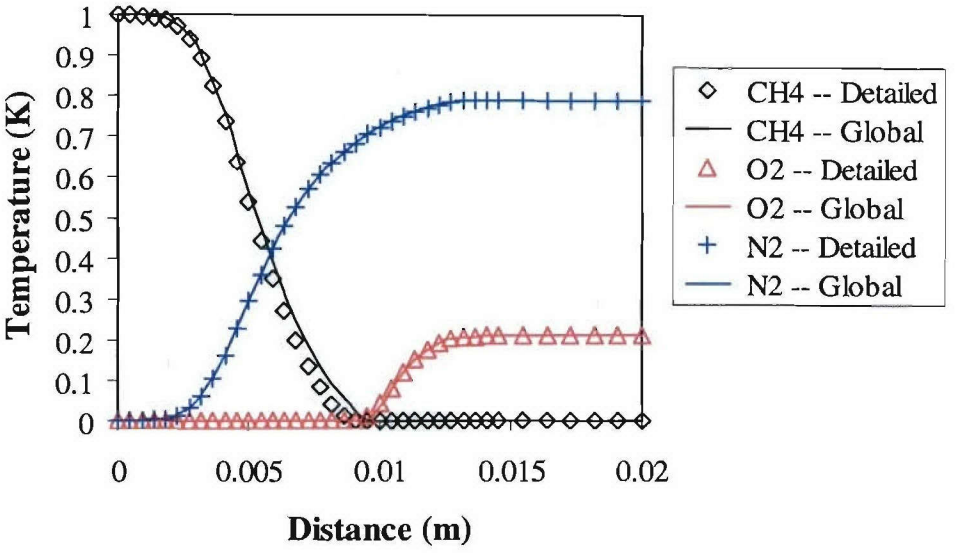

Figure 32. Species Profiles Of CH_4, O_2, And N_2 For 1-D Opposing Diffusion Flame Using Fitted Global Rate Parameters Compared To The Detailed GRI-3.0 Mechanism Species Profiles

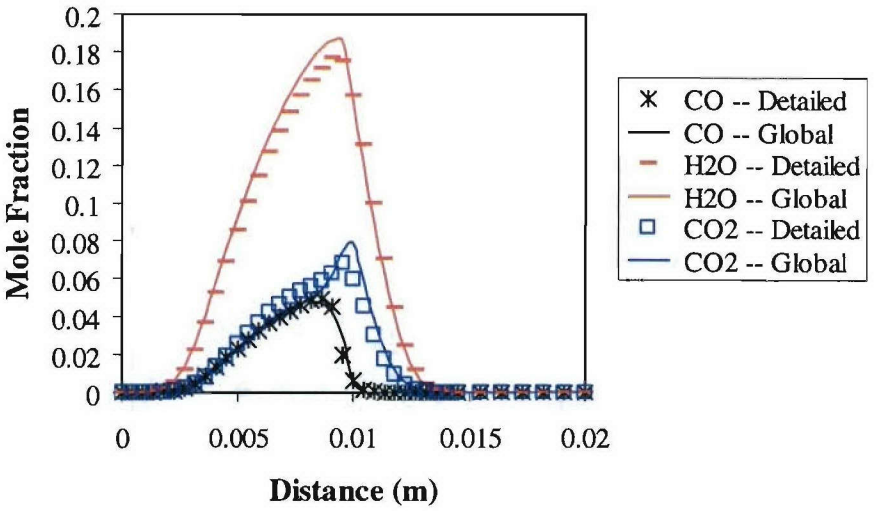

Figure 33. Species Profiles Of CO, H_2O, And CO_2 For 1-D Opposing Diffusion Flame Using Fitted Global Rate Parameters Compared To The Detailed GRI-3.0 Mechanism Species Profiles

Two additional steps were added to the global mechanism previously described to account for NO_x formation. This resulting mechanism is shown in Table 12. In the first NO_x step, the rate is not only a function of the N_2 and O_2 concentrations, but also of CO_2. In the second step, the rate is a function of only O_2 and N_2. The first step accounts for non-thermally formed NO via prompt, nitrous oxide, NNH, and non-equilibrium Zeldovich pathways. This is because CO is indicative of the free-radical chemistry that is linked to non-thermal NO formation (Nicol et al., 1997). Thermal NO_x is accounted for by the second reaction. Figure 34 shows the comparison of the NO detailed profile with that of the global calculation. The sharp nonlinear behavior around the peak is not correctly captured, but the overall trend is predicted quite well. The other species matches are very similar to those previously shown in Figure 32.

Table 12. Global Mechanism Containing 5 Steps And 7 Species That Includes NO_x Chemistry

Reaction	A	b	Ea (J/kmol)		Order		Order		Order
$2\ CH_4 + 3\ O_2 \Rightarrow 2\ CO + 4\ H_2O$	3.46E+10	0.515	1.77E+08	CH_4	0.4974	O_2	1.284		
$2\ CO + 1\ O_2 \Rightarrow 2\ CO_2$	1.01E+07	0.0141	1.01E+08	O_2	0.5104	CO	0.6528		
$2\ CO_2 \Rightarrow 2\ CO + 1\ O_2$	3.87E+06	-0.336	1.77E+08	CO_2	0.5316				
$1\ N_2 + 1\ O_2 + 1\ CO \Rightarrow 2\ NO + 1\ CO$	1.75E+09	-0.132	1.08E+08	O_2	1.144	CO	1.176	N_2	0.2348
$1\ N_2 + 1\ O_2 \Rightarrow 2\ NO$	1.15E+08	-0.334	1.21E+08	O_2	1.35	N_2	1.236		

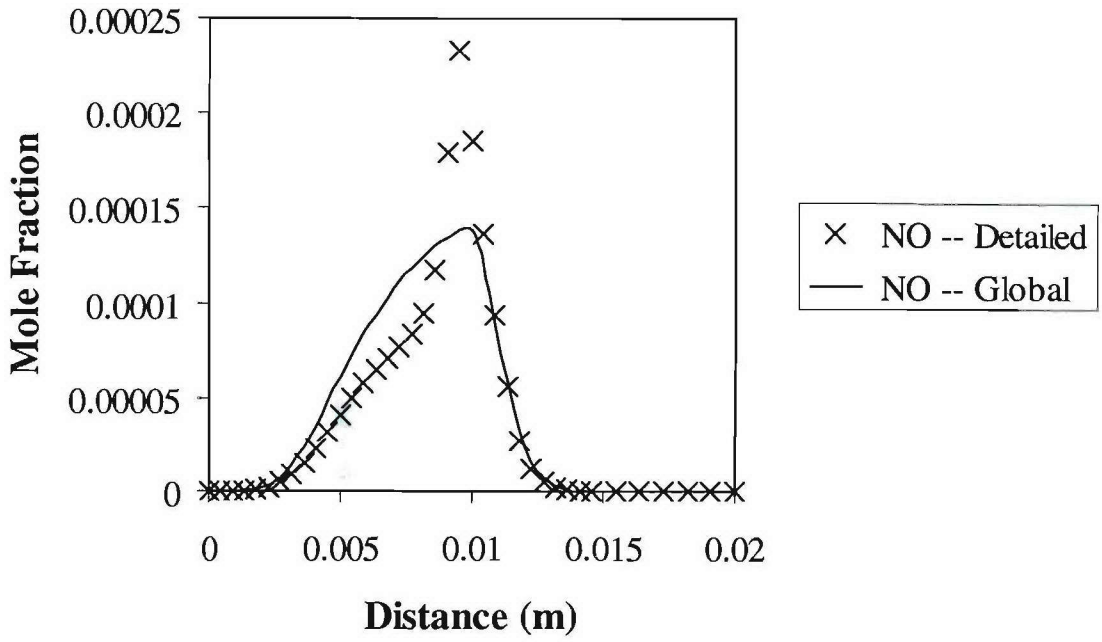

Figure 34. Species Profiles Of CO, H_2O, and CO_2 for 1-D Opposing Diffusion Flame Using Fitted Global Rate Parameters Compared to the Detailed GRI-3.0 Mechanism Species Profiles

3.5 Initial Code Validation

Comprehensive validation is a critical aspect of the program to demonstrate the capabilities of the multi-step chemistry models being developed in this SBIR. Initially, two validation cases have been identified to test the performance of the new CFD capabilities developed in this program. A turbulent premixed and a diffusion flame was selected to demonstrate the wide applicability of the approach to the analysis of turbulent reacting flows. The following sections discuss the two cases and the CFD simulations performed in the SBIR program.

3.5.1 University of Sydney Diffusion Flame Diffusion Flame

The multi-step PDF model was first validated using a diffusion flame. The piloted burner tested at the University of Sydney (Masri and Pope, 1990) has a central jet of fuel, 7.2 mm in diameter surrounded by a stoichiometric premixed and fully burned annulus of C_2H_2, H_2, and air with the C/H ratio adjusted to be the same as methane. The outer diameter of the annulus is 18.0 mm and the edges are thin. The annulus of combustion products from the pilot shields the fuel issuing from the central jet from contacting the surrounding air until a position about 4 fuel jet diameters downstream, allowing for any unburned reactants in the pilot stream to be consumed. Sketch of the piloted burner can be found in Masri and Pope's paper (1990). During all the measurements, the coflow air stream velocity, u_e, and the pilot burnt gas velocity, u_{pb}, were maintained at 15 and 24 m/s, respectively. The pilot burned gas velocity, u_{pb}, was calculated from known reactant flow rates assuming a product temperature of 2000 K. The flame characteristics were then changed by varying the methane bulk jet velocities u_j.

Masri and Bilger (1988) have reported thermocouple measurements of temperatures, LDA measurements of velocity and turbulence and composition measurements by sample probe. Space- and time-resolved measurements of temperature, density, mixture fraction, and the mass fractions of CH_4, O_2, H_2O, H_2, CO, CO_2, and N_2 have been obtained by pulsed spontaneous Raman and Rayleigh scattering in the blue (visibly soot-free) regions of pure methane flames. These data have been reported in Masri et al. (1988a, b, c). Table 13 describes the various flames investigated experimentally and indicates the type of measurements collected for each flame. The overall equivalence ratios for the three fuel injection velocities are 0.043, 0.066, and 0.088 from flame K, L, and M, respectively.

Table 13. Investigated Pilot-Stabilized Diffusion Flames of CH_4

Flame	Fuel Velocity u_j	LDA	Probe	Raman	Flame Characteristics
K	27	√	√		All yellow
L	41	√	√	√	Blue to x/D=30
M	55	√	√	√	Almost all blue

In this project, calculations are made for methane flames at the conditions listed in Table 9 (i.e. flames K, L, and M). The predictions are compared with the relevant experimental data, and the simulation results performed by Pope (1990) using a velocity-composition joint PDF transport equation solved by the Monte Carlo method. Here x is the distance from the burner's exit plane and D is the central jet diameter. In the simulations, the boundary conditions for all three passages are specified for the mean mixture fraction, the mean velocities, and the mean reaction progress variable.

A two-step reaction mechanism for methane oxidation was adopted for the multi-step model,

$$\begin{aligned} CH_4 + 1.5\,O_2 &\rightarrow CO + 2\,H_2O \\ CO + 0.5\,O_2 &\rightarrow CO_2 \end{aligned} \tag{4}$$

with Arrhenius rate coefficients used as,

$$\begin{aligned} q &= 7.943 \cdot 10^{10} \exp(-15562/T)[CH4]^{0.573}[O2]^{1.008} \\ q &= 7.079 \cdot 10^{9} \exp(-5365/T)[CO]^{0.3}[O2]^{1.946} \end{aligned} \tag{5}$$

These rate parameters were reduced from the GRI 3.0 detailed mechanism as discussed in Section 3.4. Comparisons with the experimental results for velocity, turbulence, and mixing fields for flames K, L, and M are made with the calculations from the current multi-step PDF (pdf_ms) model and from the Monte Carlo PDF (pdf_mc) model of Pope. Figure 35 shows the simulated flow field by pdf_ms for flame L. Fuel is injected from the central hole at a high speed, which gradually entrains the surrounding air to enter the fuel stream, causing the stream velocity to decrease and the stream width to expand down the stream. Fuel and air are initially separated by the burnt piloted flame gas immediately surrounding the fuel stream until an axial

position of 5D is reached, where the entrained air and fuel diffuse toward each other and combustion takes place downstream near the fuel stream surfaces as shown in Figure 36 with corresponding rising temperature.

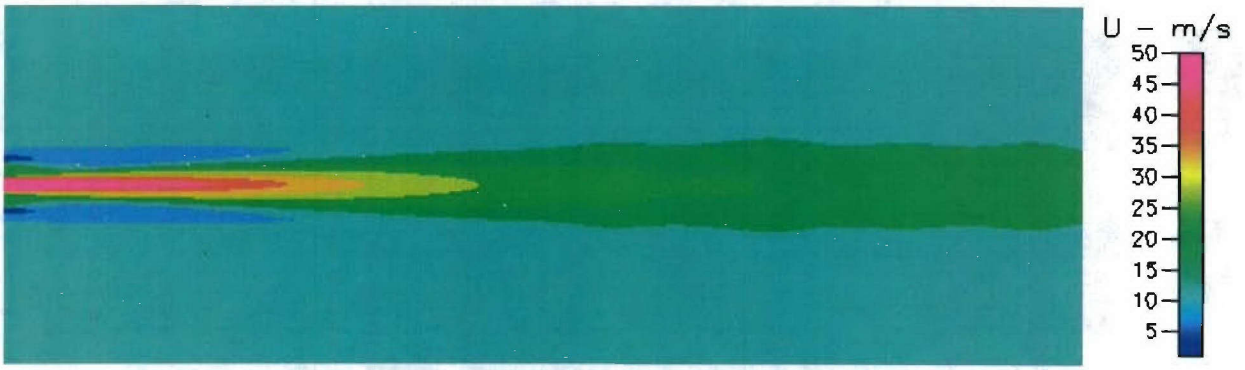

Figure 35. Calculated Axial Velocity Distribution for Flame L

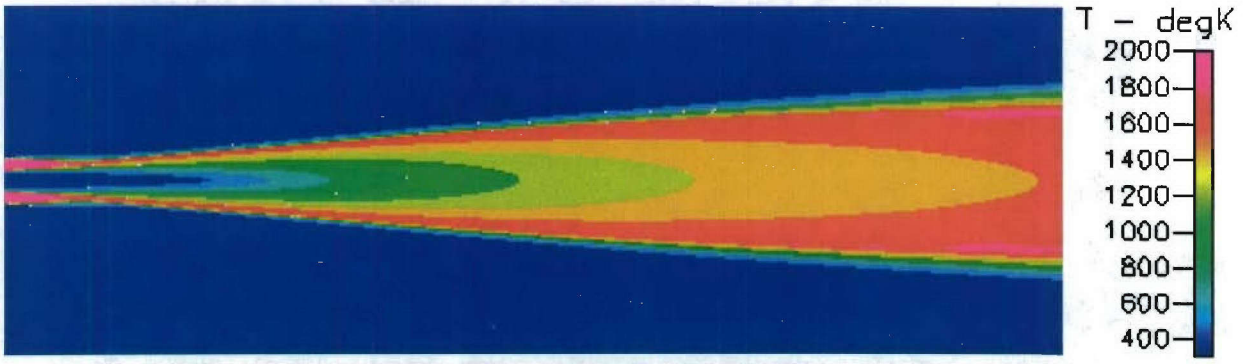

Figure 36. Calculated Flame Temperature Distribution for Flame L

Flame K, Axial Velocity = 27m/s

Figure 37 shows plots of axial velocity (a), normalized temperature (b), CO mass fraction (c), and O_2 mass fraction (d) at an axial location of x/d of 20. Results at an x/d of 50 are shown in Figure 38. In general, agreement is very good. The gradient in the O2 mass fraction is steeper than measured, placing the flame location a little farther radially out than measured. However, CO predictions are relatively good. Temperature predictions also match the data well. Velocity matches are good, with the center peak velocities being under predicted.

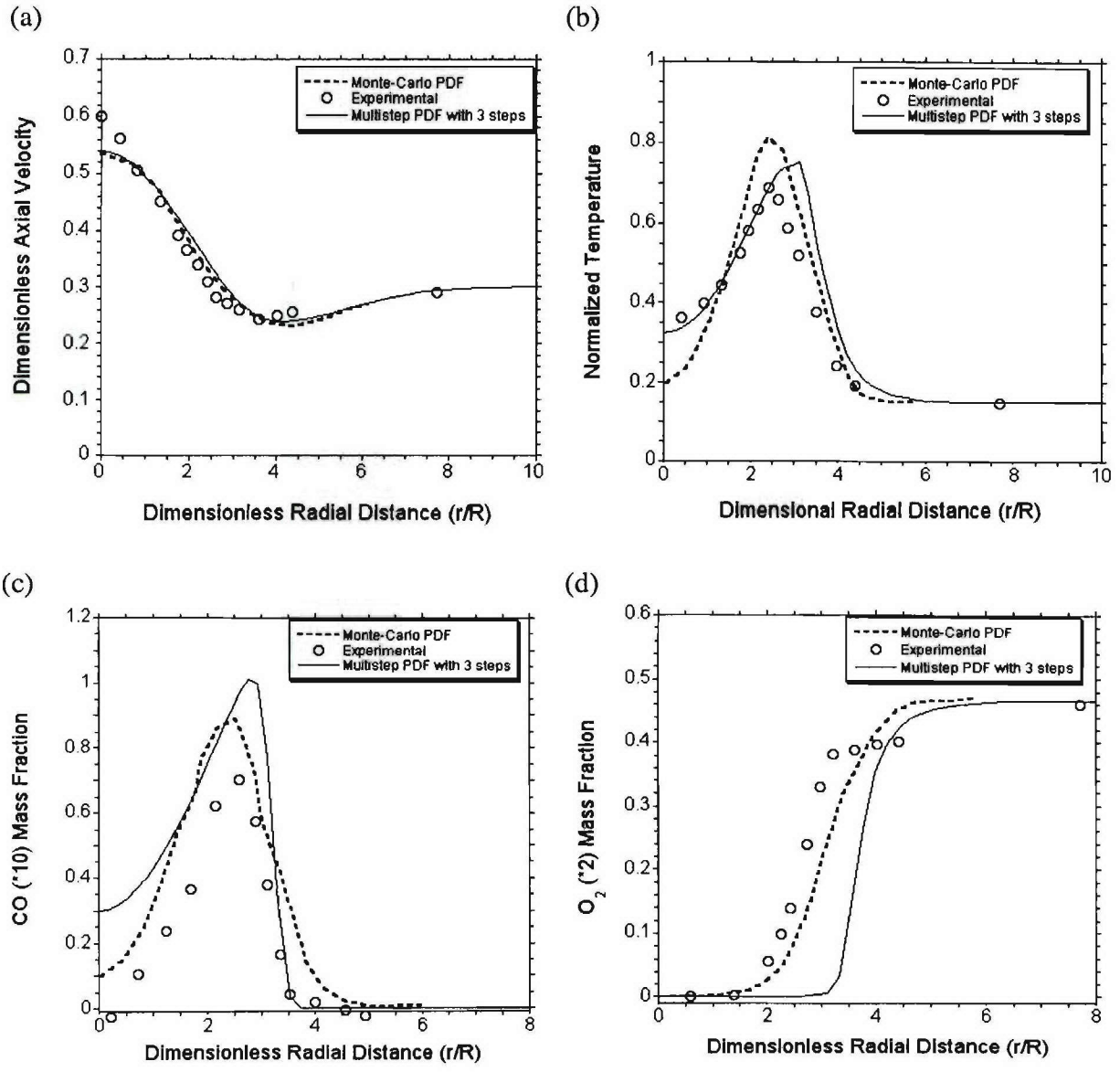

Figure 37. Results for Diffusion Flame K with an Inlet Axial Velocity of 27m/s at an x/d = 20

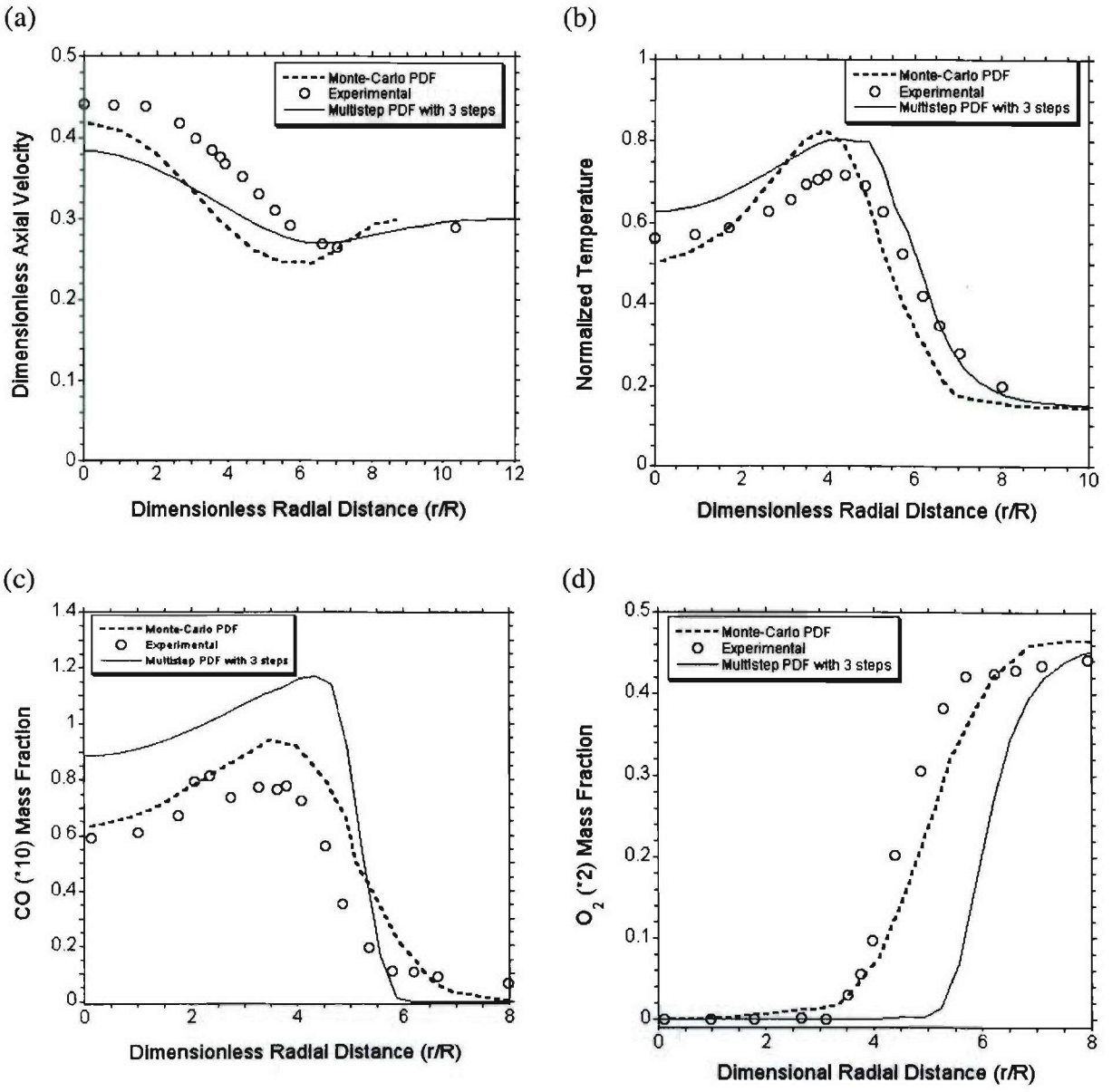

Figure 38. Results for Diffusion Flame K with an Axial Inlet Velocity of 27m/s at an x/d = 50

Flame L, Axial Velocity = 41m/s

The results for Flame K, with an axial velocity of 41 m/s, are plotted in Figures 39 and 40. Again, the overall agreement with the data is relatively good. There is some overshoot in temperature, but the results are comparable with the more computationally expensive Monte Carlo PDF method. The peak in CO is over predicted and the concentration gradient on O2 is steeper than measured. It is likely that for 3-step kinetics are insufficient and agreement would improve with the application of more complex mechanisms. Also, as the jet velocity is increased, the effect of local extinction, due to turbulent strain, starts to become important. This effect is not included in the present model.

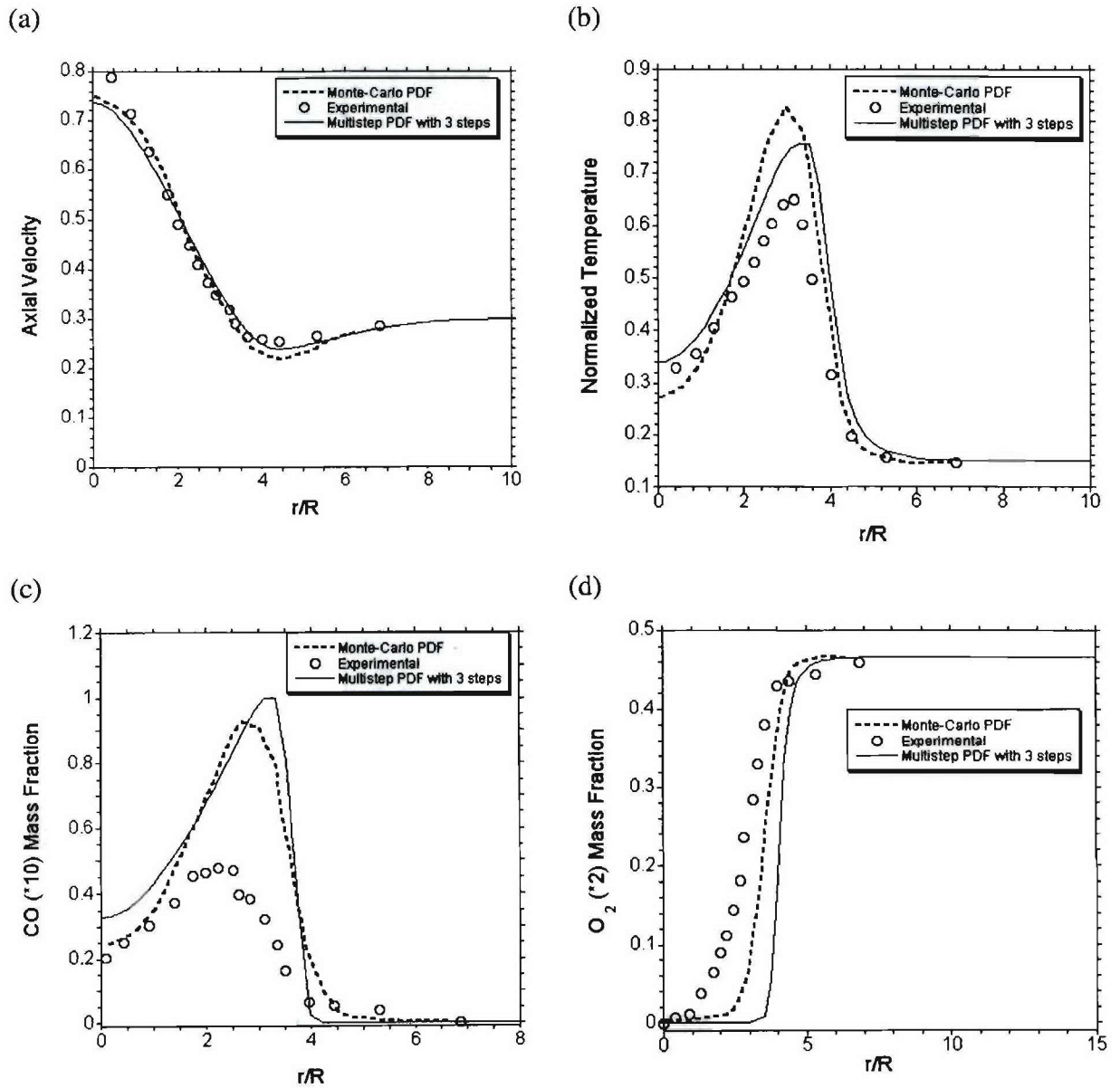

Figure 39. Results for Diffusion Flame L with an Axial Inlet Velocity of 41m/s at an x/d = 20

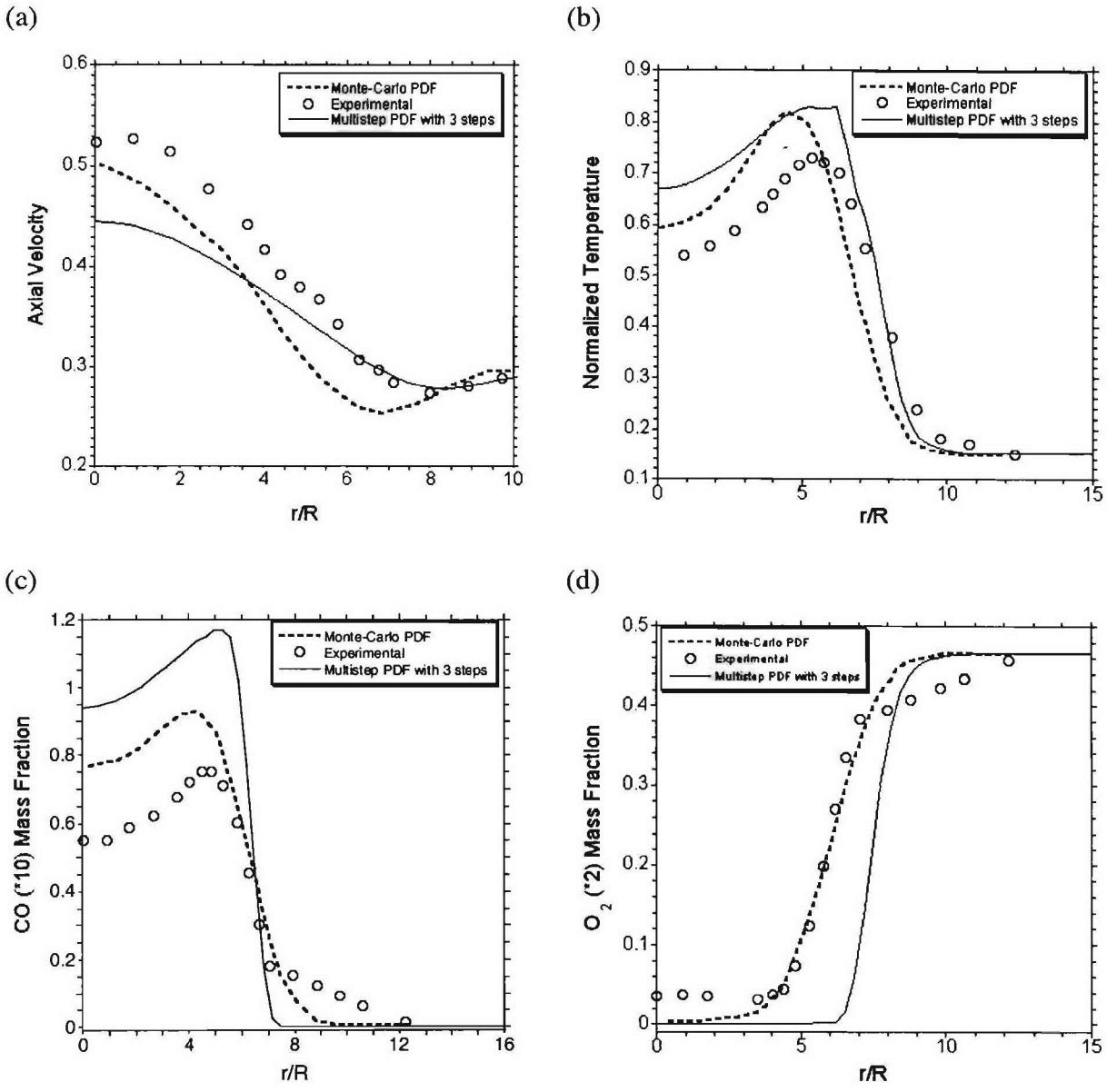

Figure 40. Results for Diffusion Flame L with an Axial Inlet Velocity of 41m/s at an x/d = 50

Flame M, Axial Velocity = 55 m/s

The results for Flame M, with an axial velocity of 55 m/s, are plotted in Figures 41 and 42. Velocity profile match well, but the temperature and species predictions show significant deviations from the measured data. The same is true for the Monte Carlo PDF predictions. At this jet velocity, local extinction due to turbulent strain is playing an important role. Since this effect is not accounted for in the present model, the simulations show reactions taking place earlier than measured. A turbulent strain model can be incorporated into the present framework and CFDRC will look at appropriate options for continued development of the capability in the future.

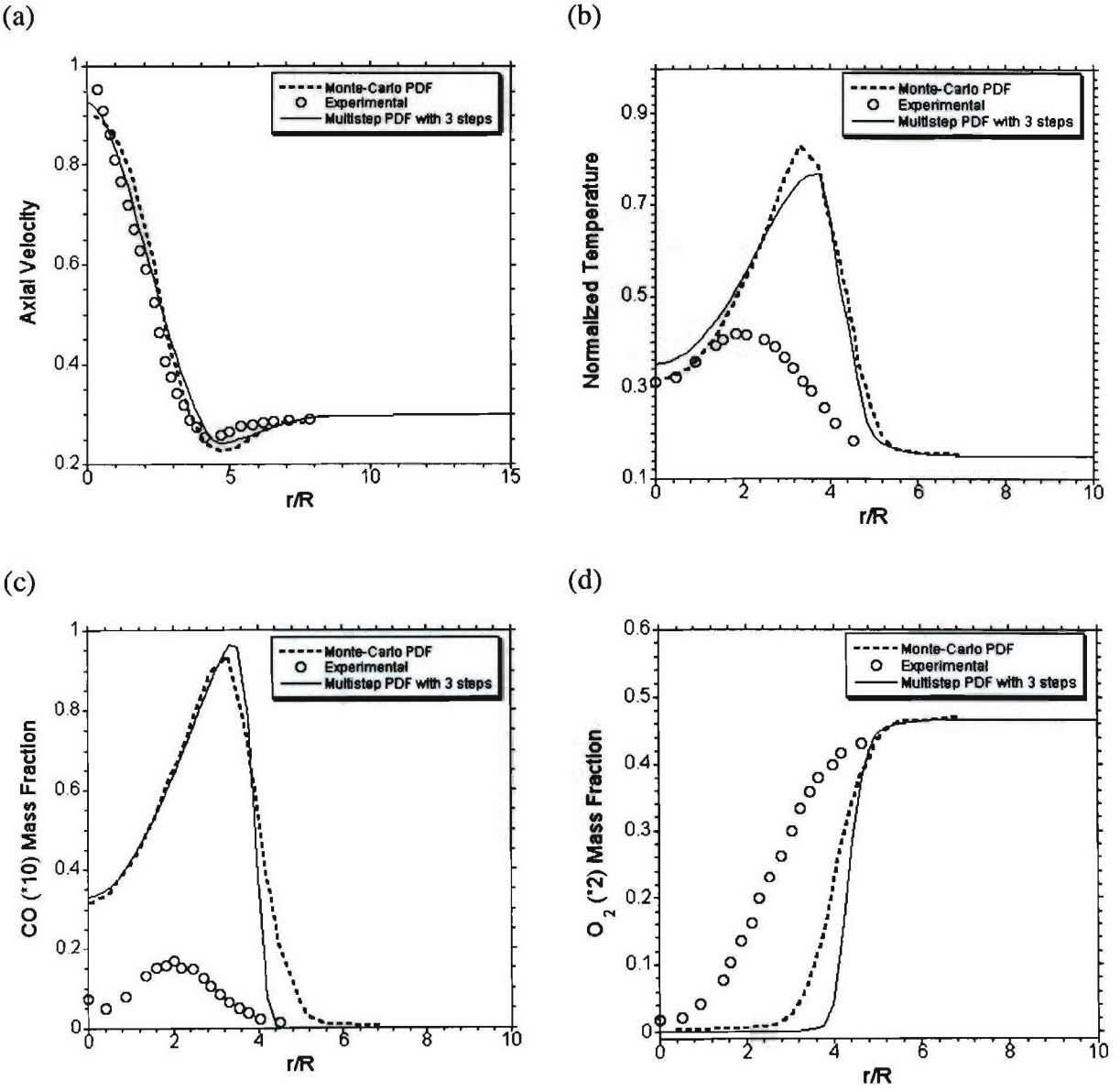

Figure 41. Results for Diffusion Flame M with an Axial Inlet Velocity of 55m/s at an x/d = 20

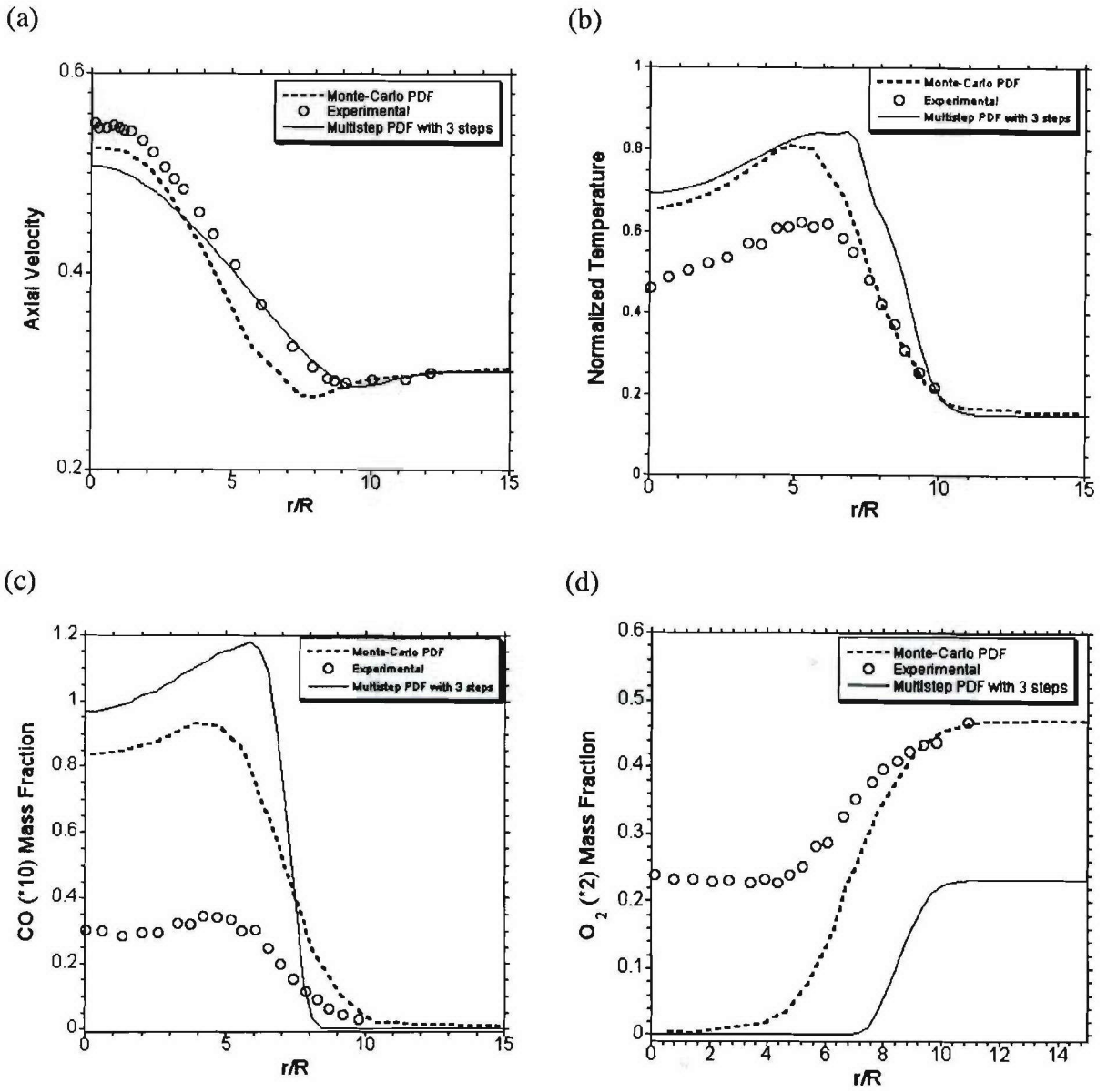

Figure 42. Results for Diffusion Flame M with an Axial Inlet Velocity of 55m/s at an x/d = 50

3.5.2 Premixed Flame of Moreau et al.

The potential of the multi-step PDF model was further studied by applying it to a two-dimensional premixed combustion case, with the test burner designed by Moreau *et al.* (1976, 1977). A lean-premixed mixture of methane and air, which has been preheated to 600 K, constitutes the main stream into the combustor. Parallel to the main stream, a pilot stream of hot exhaust gases at 2000 K is injected for flame stabilization. The mass flow of the pilot stream is approximately 15% of the main stream. The test section has a length of 1000 mm. The main stream has a height of 80 mm and the pilot stream has a height of 20 mm. The width of the test section is 100 mm. The whole setup is adiabatic, except for some heat loss occurring at the silica windows of the test section.

Moreau *et al.* (1976, 1977) performed measurements for various inlet velocities and equivalence ratios. Concentrations of chemical species were determined by gas chromatography of samples taken with extractive probes. The most data are available for an equivalence ratio of approximately 0.82 and velocities of 69 m/s for the main stream and 121 m/s for the pilot stream close to the inlet of the test section (Bohn and Lepers, 1999). Therefore, these boundary conditions were chosen for use in the numerical simulation. The experiments were performed at atmospheric pressure. The experiments were performed at atmospheric pressure, with the flame front observed to stabilize in the combustion chamber as shown in Figure 43.

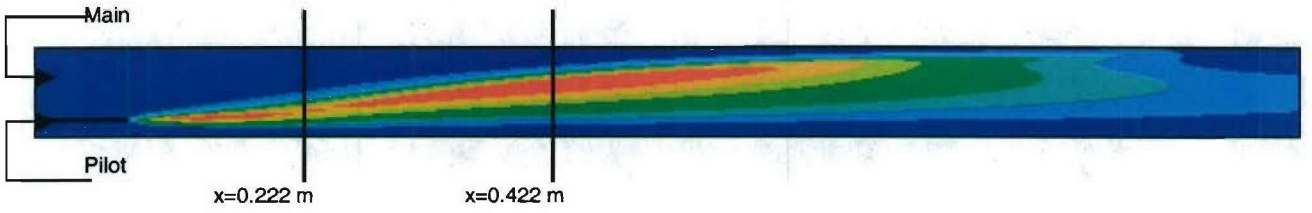

Figure 43. Flame Front (Progress Variance)

For this simulation, a two-step reaction mechanism for methane oxidation was adopted,

$$\begin{aligned} &\textit{Step 1 - } CH_4 + 1.5O_2 \rightarrow CO + 2H_2O \\ &\textit{Step 2 - } CO + 0.5O_2 \rightarrow CO_2 \end{aligned} \tag{29}$$

with Arrhenius rate coefficients given by Dupont et al. (1993).

$$\begin{aligned} q_1 &= 1.0 \cdot 10^{10} EXP(-12019/T)[CH_4][O_2] \\ q_2 &= 1.0 \cdot 10^{10} EXP(-12019/T)[CO][O_2] \end{aligned} \tag{30}$$

Calculations using laminar chemistry or a PDF turbulent combustion model with one-step global mechanism could not predict a stable flame front located inside the combustion chamber similar to the experimentally observed one. The calculated flame either flashes back to the inlet or blows out. The present model predicts the flame front stabilized inside the combustion chamber as shown in Figure 44.

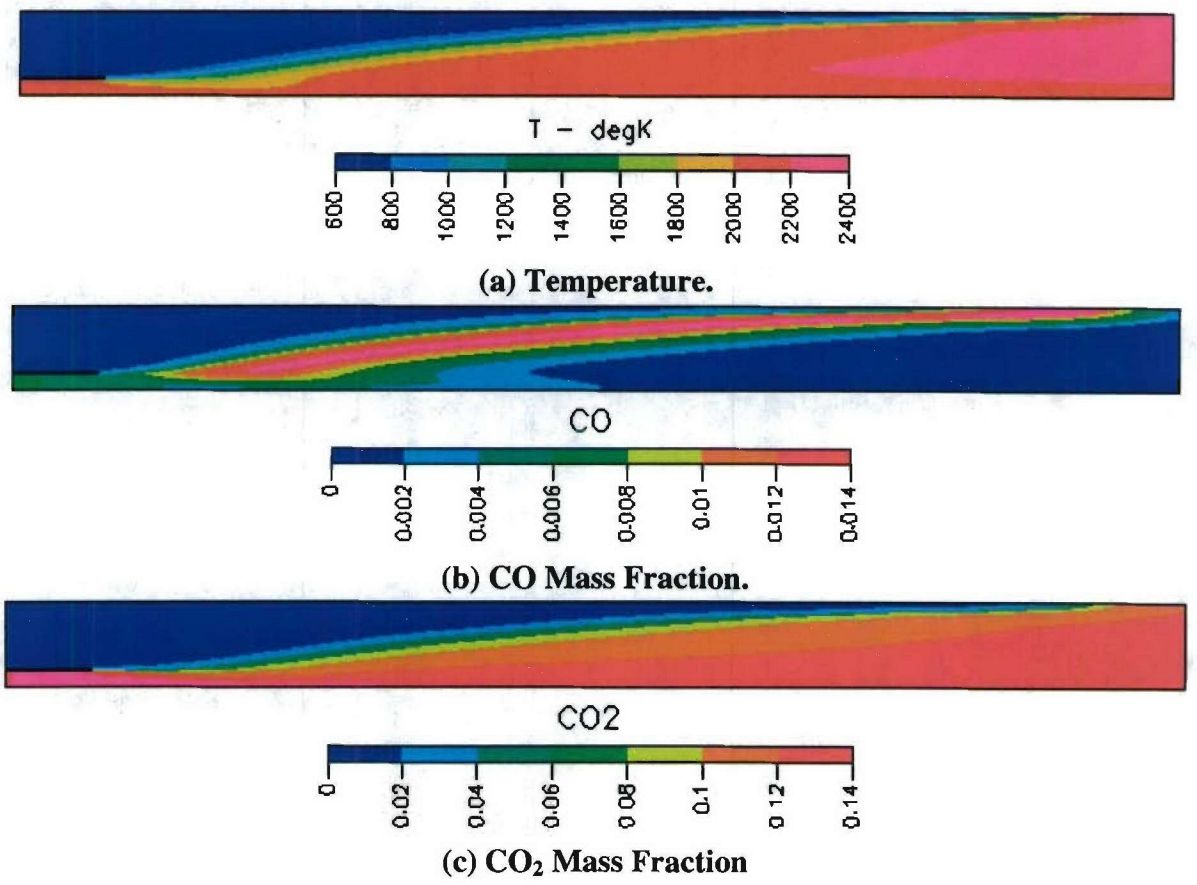

Figure 44. Calculated Distributions of Temperature, CO, and CO_2 Mass Fraction

Comparisons of species and temperature profiles are shown in Figures 45 and 46. Figure 45 gives the comparison of the calculated fuel (CH4) concentration distribution along the cross section (y direction) with the measured result. These fuel concentration data have been normalized by the N2 concentration, which is a constant value in the whole field as the flame is premixed. At the axial position of x=0.222 m, the upper section is dominated with the unburned mixture. The pilot flame ignites the premixed flow, and turbulent combustion develops in the mixing layer behind the board that originally separates the unburned mixture with the pilot flame. The current model predicts the flame propagation well with good agreement of the major species concentration profiles to the measured data.

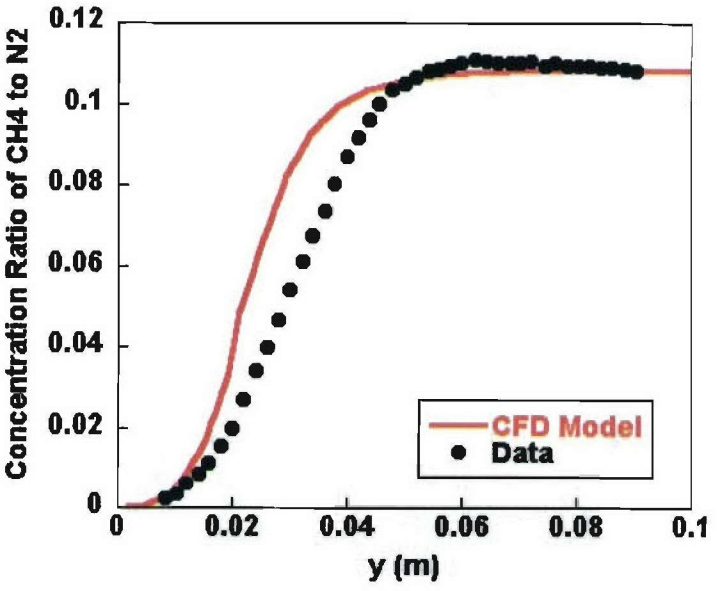

(a) x= 0.222 m

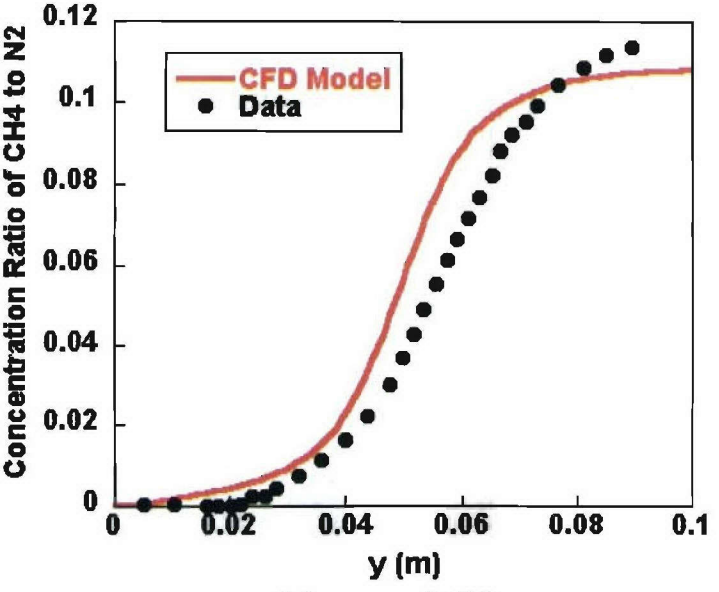

(a) x = 0.422 m

Figure 45. Comparison of Fuel Concentration Profile Normalized by N_2 Concentration

Figure 46 shows a comparison of calculated and measured flame temperature distributions at x=0.422 m. At this location, the flame has propagated to the upper section of the main stream, ranging from y=0.03 m to 0.07 m. Here, the present combustion model predicts an appropriate flame front located around y=0.05 m. Some deviation between the calculated results and the measured data exist in the high temperature region with the model predicting a slightly faster temperature rise than was measure. However, overall agreement with the experimental data is good.

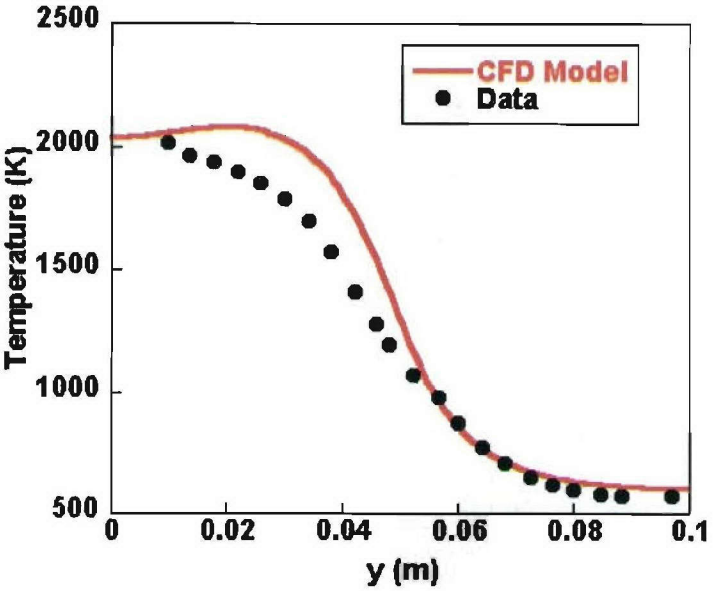

Figure 46. Comparison of the Flame Temperature Profile

3.6 Final Code Validation

Several laboratory flame geometries were selected for final validation of the newly developed LES and multi-step PDF combustion capability. The cases included a premixed flame, two swirl stabilized flames, and a jet diffusion flame. The cases are well established in the literature and are also currently being used by researchers around the world to validate advanced turbulence-combustion modeling techniques. Often the flames are near extinction limits and challenging to predict numerically. RANS results are typically poor and LES, with multi-step chemistry, is necessary in achieving accurate results. Simulations were performed with the conventional single-step capability and with the new multi-step PDF combustion model. LES simulation results with multi-step kinetics were limited, due to the inadequacy of the point-solver approach available in CFD-ACE+.

3.6.1 Bluff Body Lean-Premixed Combustor

Experimental data in a bluff-body-stabilized combustor at lean premixed conditions were obtained by Nandula, Pitz, and coworkers (Pan et al., 1991; Nandula et al., 1996). These laser-Doppler anemometry (LDA) measurements of velocity and a combination of Rayleigh scattering, spontaneous Raman scattering, and laser-induced fluorescence (LIF) measurements were obtained to provide a source of information with which to evaluate combustion models. The uncertainty involved in the species and temperature measurements, based on a single-shot uncertainty analysis, is given in Table 14.

Table 14. Uncertainty in Chemical Species Measurements and Temperature Measurements from Nandula et al (1996)

Scalar	% Error
CH4	3.3
O2	7.5
H2O	5.1
CO2	5.1
NO	7.6
CO	17.6
Temperature	1.0

The combustion chamber, shown in Figure 47, was configured such that a stainless steel conical bluff body of base diameter 44.45 mm and apex angle 45° was mounted coaxially at the center of the combustor and served as a flame holder. The burner enclosure consisted of a square cross-section with filled round corners.

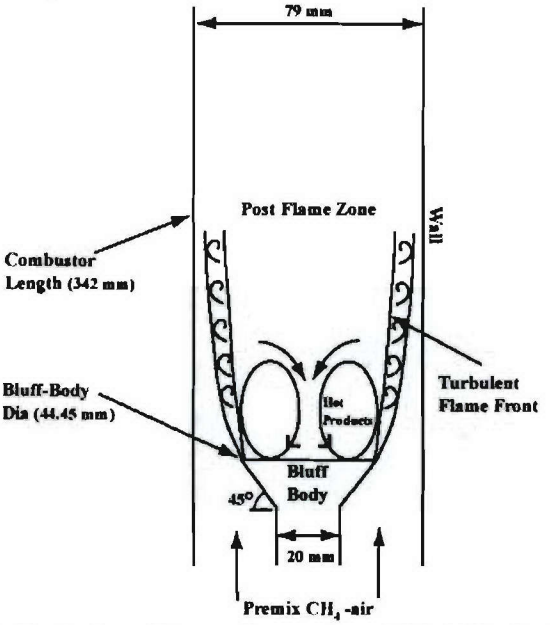

Figure 47. Schematic and Turbulent Flame Structure of Bluff-Body-Stabilized Lean Premixed Combustor (Nandula et al., 1996)

The CFD simulations use a full 3D geometry (1015488 cells) as shown in Figure 48. The mass-flow rate for the combustor was specified by using the measured values reported for the air (3960 slpm) and the CH_4 fuel (244 slpm). This corresponded to a CH_4-air equivalence ratio of 0.586. The free stream turbulence at the inlet was measured to be 24% (based on a 15 m/s mean velocity). Appropriately scaled turbulence levels were set in the LES model at the inlet for the boundary condition of k_{sgs}. An inlet temperature of 300 K and a combustor pressure of 1 atm were also specified in the model. Wall temperatures for the combustor and bluff-body were set to 500 K.

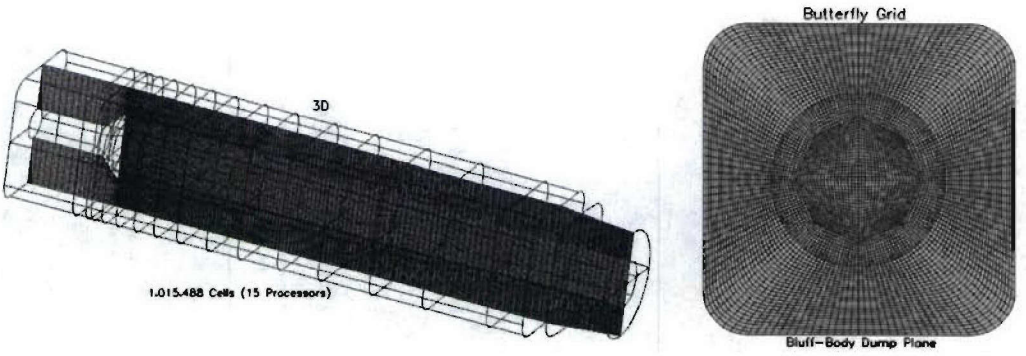

Figure 48. Structured Grids for 3D Combustor Geometry

Table 15 shows the multi-step mechanism used for the calculations. The rates were determined using a fit to laminar 1D flame calculations using the GRI 3.0 mechanism as described in Section 3.2.3.

Table 15. Optimized Arrhenius Rate Parameters Nandula 3-Step Methane Oxidation Mechanism (Phi = 0.586, T=300 K)

$CH_4 + \frac{3}{2}O_2 \Rightarrow CO + 2H_2O$	$R_1 = 4.56\times10^{9} T^{0.1048} \exp\left(\frac{-15273}{T}\right)[CH_4]^{0.6199}[O_2]^{0.8846}$
$CO + \frac{1}{2}O_2 \Rightarrow CO_2$	$R_2 = 3.76\times10^{11} T^{0.28} \exp\left(\frac{-8556}{T}\right)[CO]^{1.9127}[O_2]^{1.0167}$
$CO_2 \Rightarrow CO + \frac{1}{2}O_2$	$R_3 = 6.023\times10^{5} T^{-0.318} \exp\left(\frac{-15426}{T}\right)[CO_2]^{1.134}$

The lean operating conditions of the Nandula combustor make it difficult to simulate. The RANS simulations with and without multi-step kinetics did not lead to a converged solution with a flame. The flame structure in the RANS simulations would gradually pinch off downstream of the bluff body until the flame extinguished. Figure 49 shows a plot of the temperature profiles in the RANS simulations illustrating the pinching off and extinguishing of the flame downstream of the bluff body.

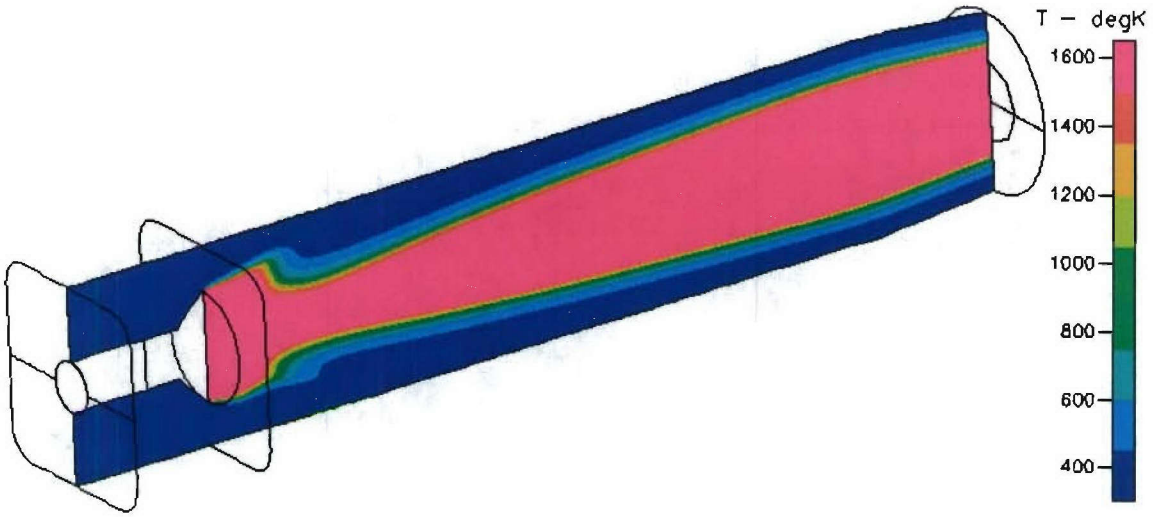

Figure 49. RANS Simulation Results Prior to Blowout Showing the Extinguishing of the Flame Downstream of the Bluff Body

By capturing the turbulent flow structures that mix hot products and reactants together, LES simulations are capable of predicting a stable flame. At the very lean operating conditions of this validation case, LES is essential to capture realistic flame behavior. The simulation is also very sensitive to the kinetics used. Due to bug fixes and software problems, the simulation was restarted multiple times. Figures 50 through 52 shows snapshots from the LES calculations for temperature, axial velocity, and CO mass fraction. Averaged quantities are not yet available for the simulation.

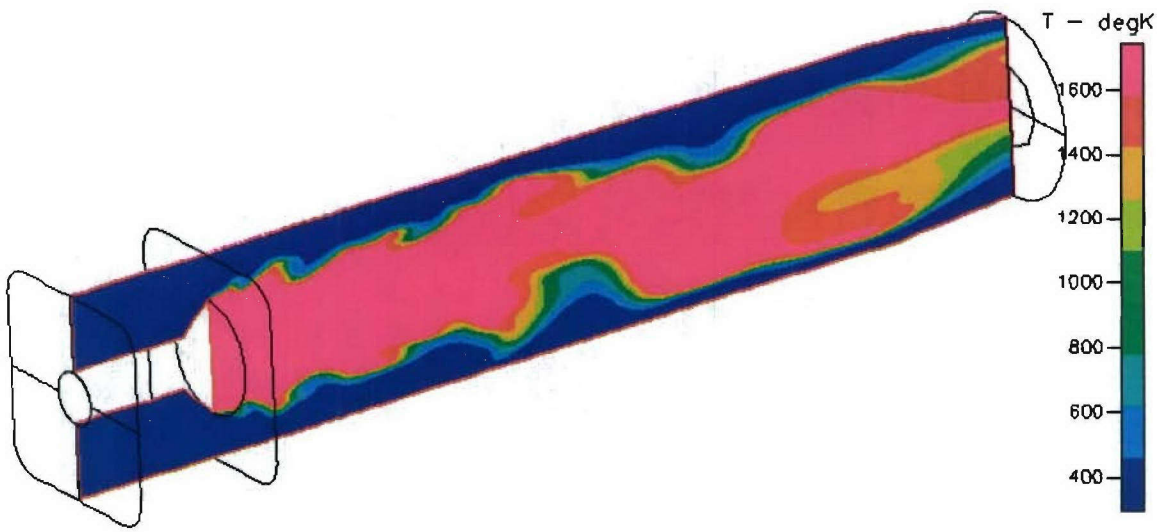

Figure 50. Snapshot of Temperature in the Nandula Bluff-Body Combustor LES Simulation Using Multi-Step Chemistry

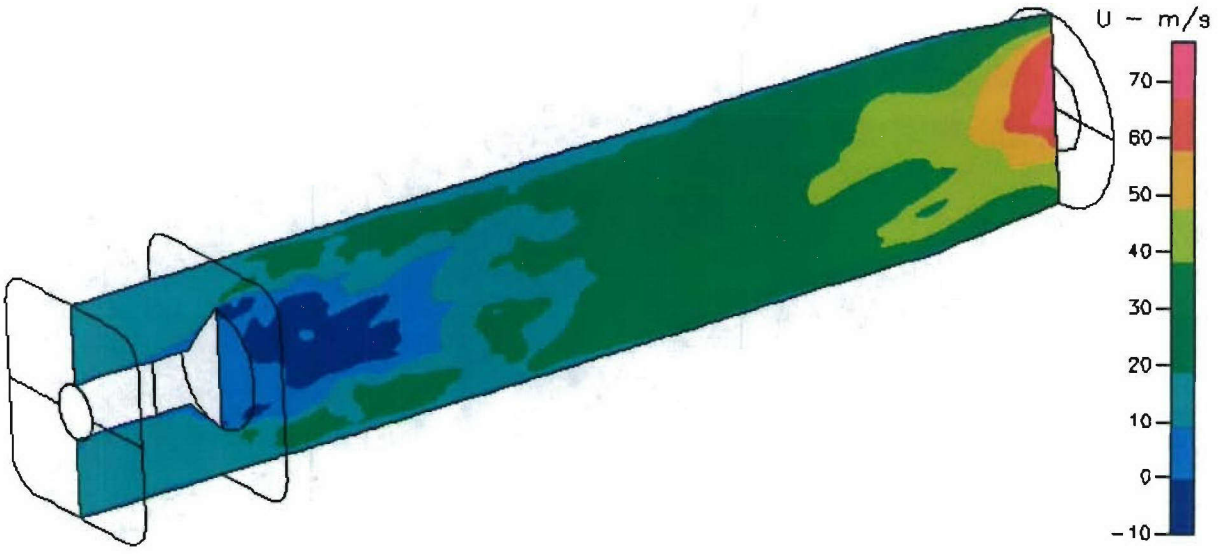

Figure 51. Snapshot of Axial Velocity in the Nandula Bluff-Body Combustor LES Simulation Using Multi-Step Chemistry

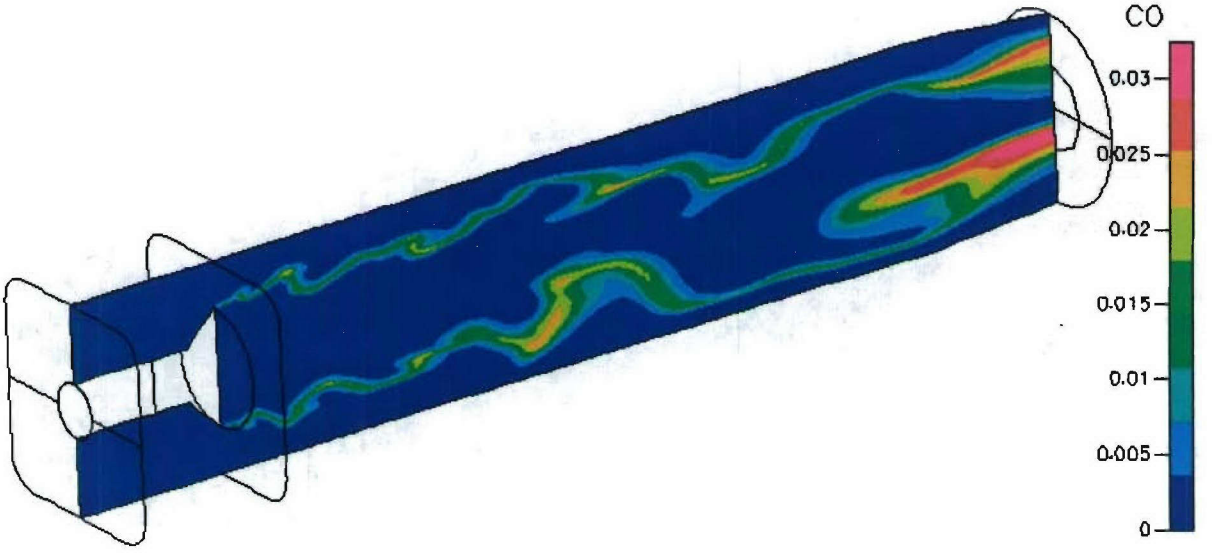

Figure 52. Snapshot of CO Mass Fraction in the Nandula Bluff-Body Combustor LES Simulation Using Multi-Step Chemistry

Comparison of the predicted temperature, CO, CO_2, H_2O, and O_2 are shown in the following plots (Figures 53 through 56) at axial locations with an x/d of 0.1, 0.6, and 1.0. Only instantaneous LES results are available at this time. As the results are averaged, the peaks in the profiles will be reduced as the fluctuations in the flame surface are accounted for. Overall the radial flame location is predicted well. As expected, the gradients in the instantaneous LES plots

are much steeper than those observed in the averaged data. The fluctuations captures within the LES simulation will tend to smooth out gradients and decrease the peak magnitudes as the results are averaged. CO concentrations downstream of the bluff body are significantly lower (about 80%) than the measured data.

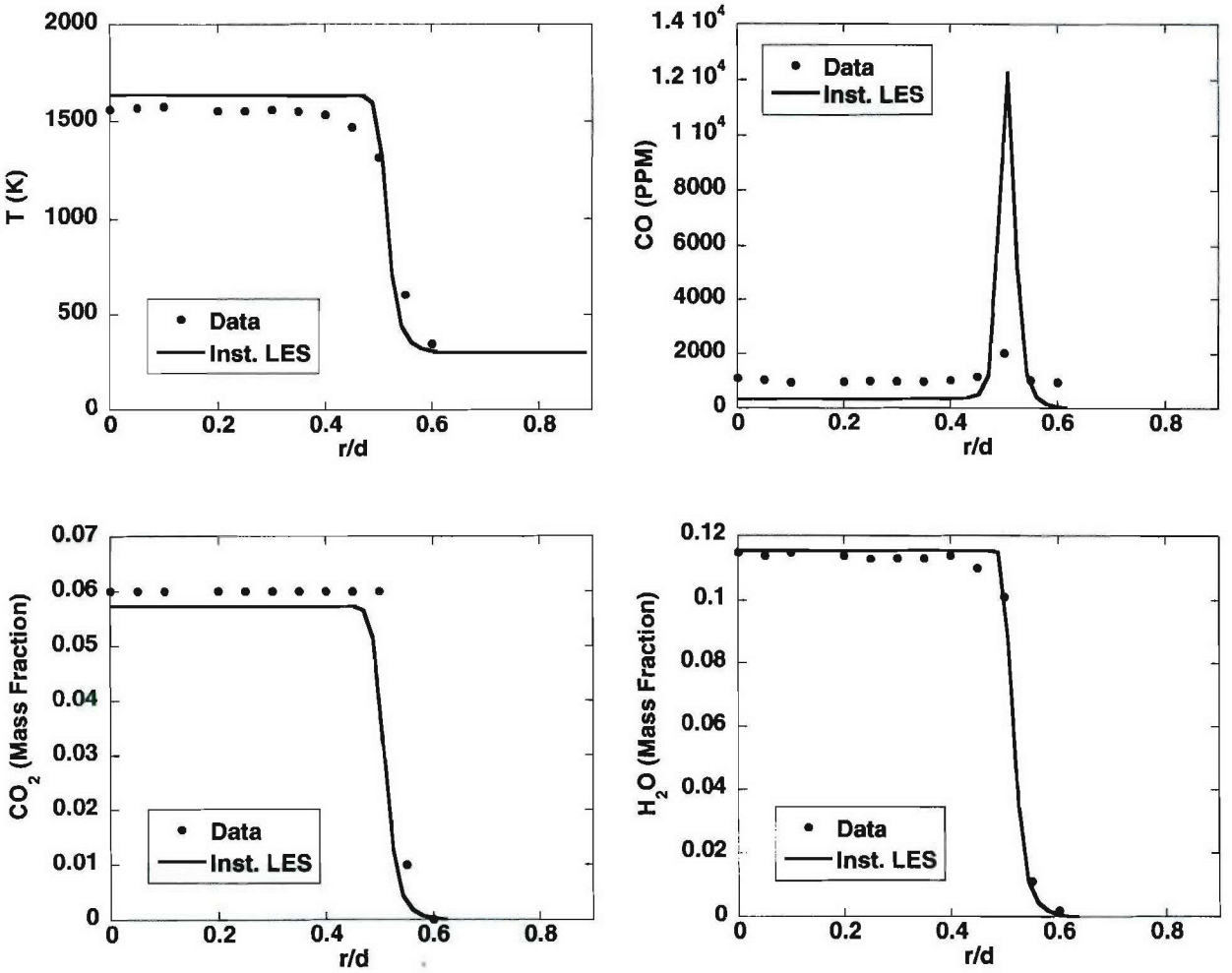

Figure 53. Plots of Instantaneous LES Results Compared to the Averaged Measured Data for CO, T, CO_2, and H_2O Downstream of the Bluff Body at an x/d of 0.1

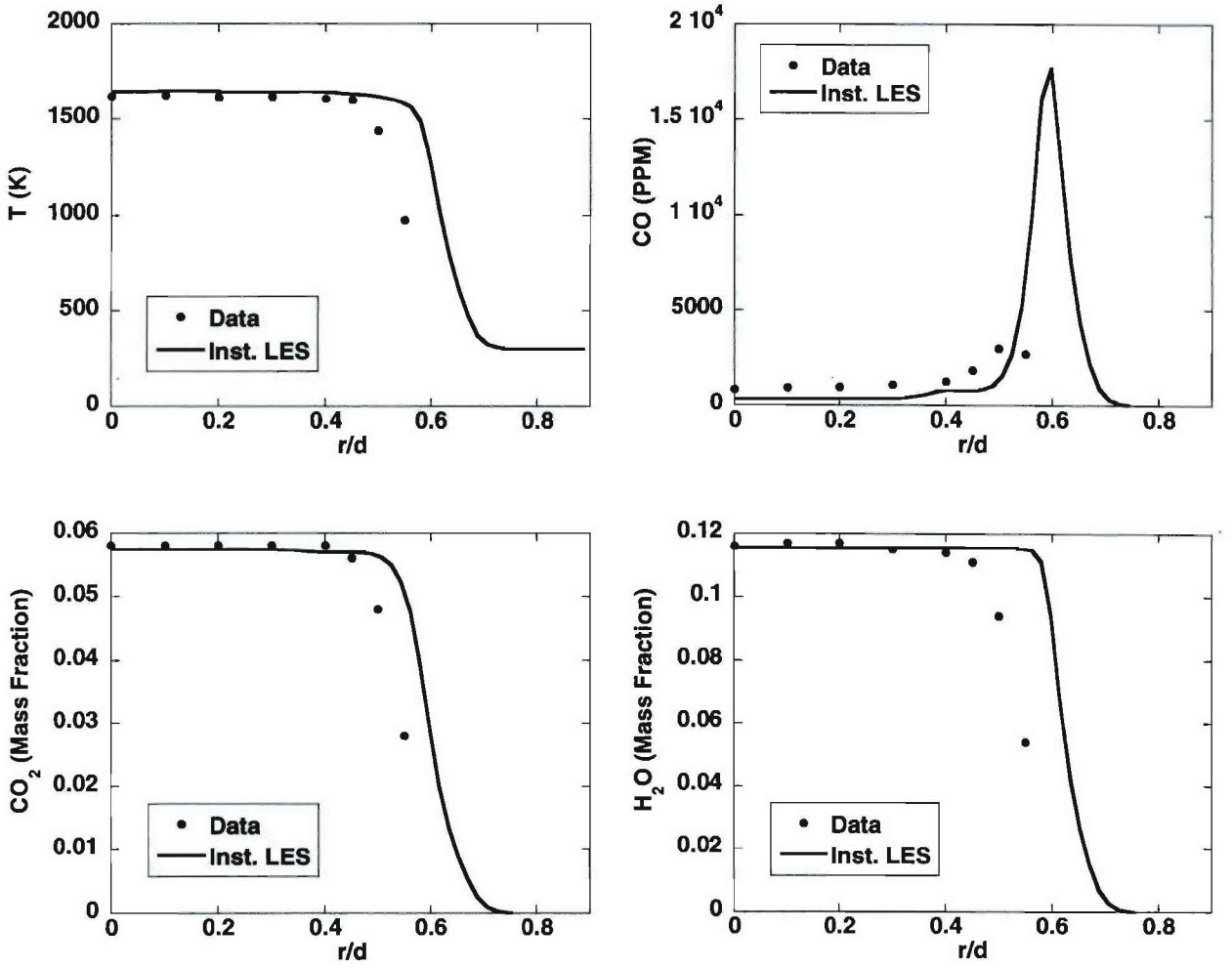

Figure 54. Plots of Instantaneous LES Results Compared to the Averaged Measured Data for CO, T, CO_2, and H_2O Downstream of the Bluff Body at an x/d of 0.6

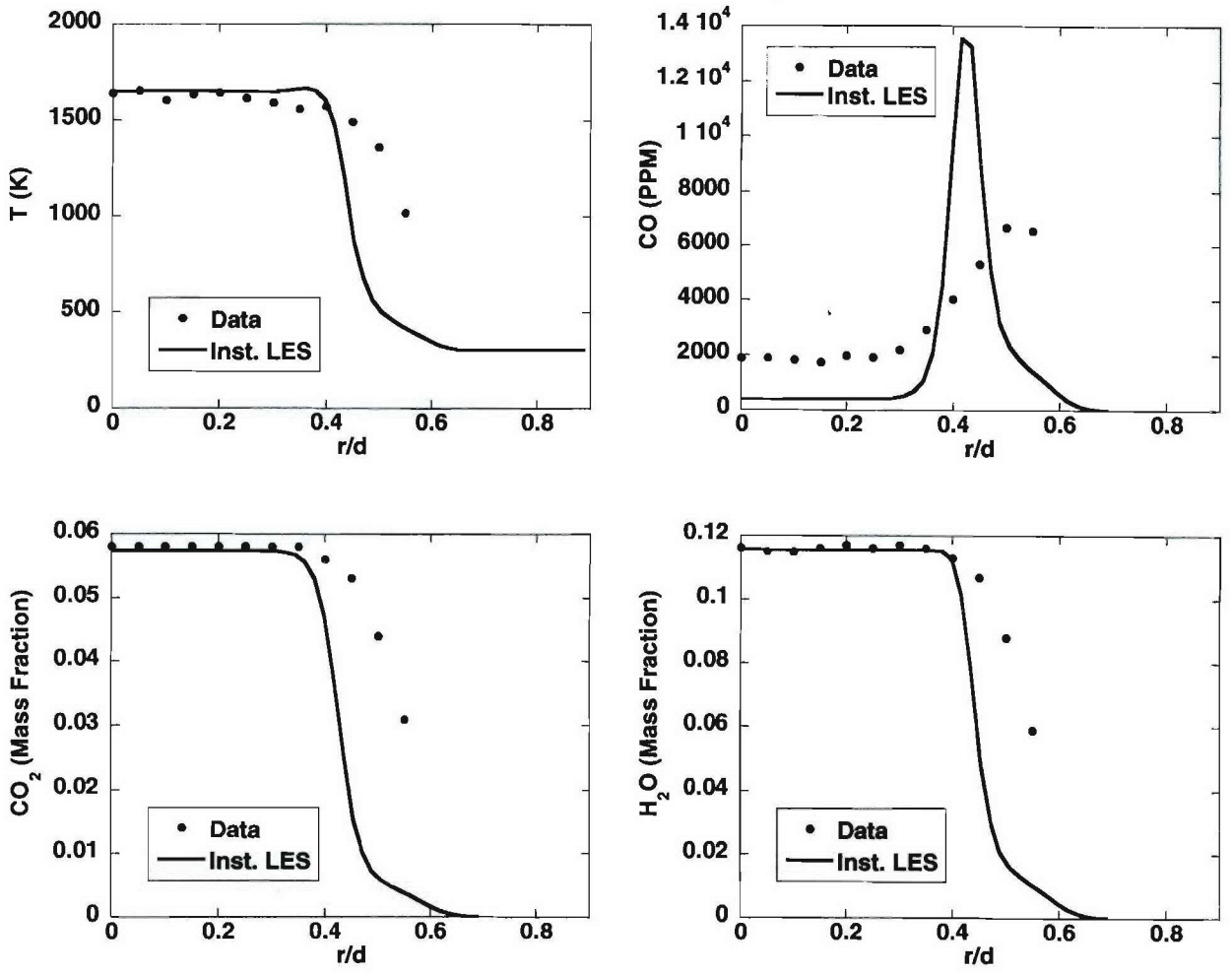

Figure 55. Plots of Instantaneous LES Results Compared to the Averaged Measured Data for CO, T, CO_2, and H_2O Downstream of the Bluff Body at an x/d of 1.0

3.6.2 SMA2 – Swirl Stabilized Methane Air Flame

Swirl stabilized diffusion flames are often observed in practical combustors. The new CFD capabilities developed in this program must be able to resolve the characteristics of these flames correctly. As part of the TNF workshop, detailed experiments have been performed for swirl stabilized diffusion flames. A comprehensive set of validation data has been collected that can be used to validate turbulence and chemistry models. For this reason, the SMA2 flame was selected as a validation case. The SMA2 flame is the high swirl diffusion flame extensively documented in the TNF workshop. The following sections briefly review the burner details presented in the last quarterly report. The CFD setup and results from the RANS calculations are presented in the next section.

Experimental Setup: The swirl burner for the SMA2 case is centrally located in an air co-flow. The co-flow is confined in a square duct with sides 130 mm in length. Air flows through the swirler annulus, which is supplied through the main inlet and/or the tangential injectors as shown in Figure 56. Figure 57 shows a picture of the SMA2 flame [TNF workshop, 2002]. The fuel (2

parts air and 1 part methane by volume) issues from the central jet, located in the center of the ceramic bluff-body face. The jet is fully developed at the burner exit. The SMA2 flame characteristics are summarized in Table 16.

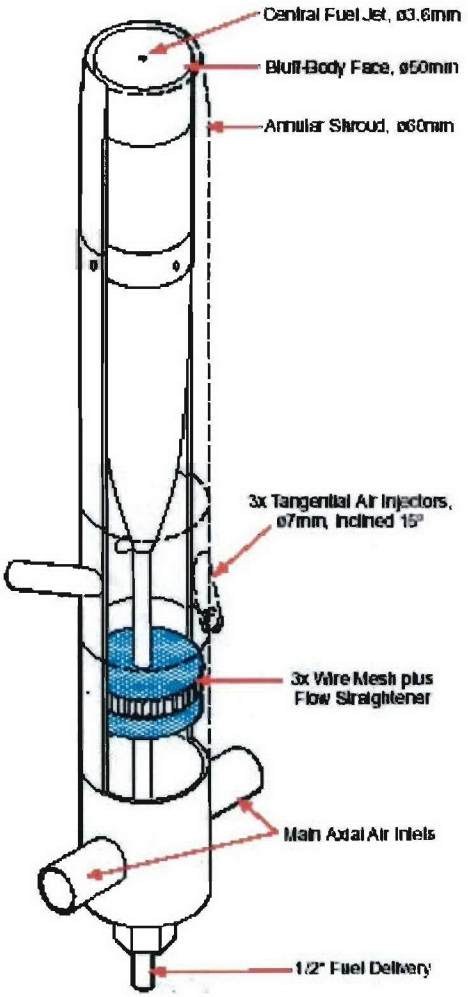

Figure 56. SMA2 Burner Schematic

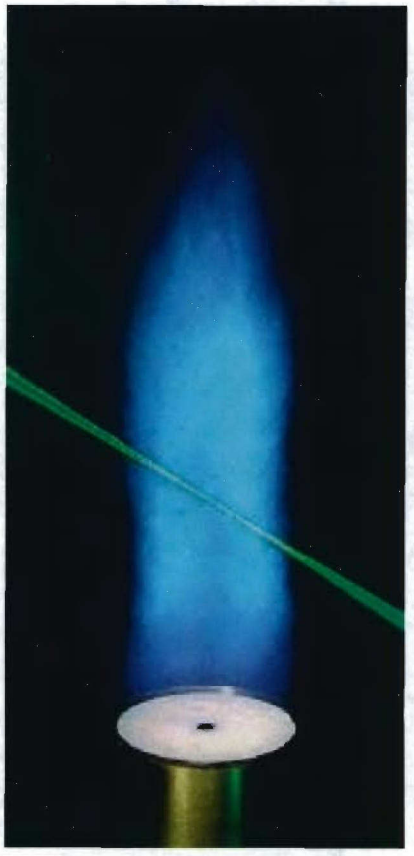

Figure 57. The SMA2 Flame

Table 16. SMA2 Operating Conditions.

Fuel mixture	Axial annulus velocity (m/s)	Tangential annulus velocity (m/s)	Fuel jet velocity (m/s)	Reynolds number at annulus exit	Reynolds number of fuel jet	Swirl number
Methane -Air	16.3	25.9	66.3	32400	15400	1.59

The experimental data set for this case consists of radial profiles of axial and tangential velocity, temperature and mass fraction of OH, CO, CO_2, H_2O at many locations downstream of the burner exit. This set of data results in a comprehensive test of the CFD capabilities to predict the characteristics of a swirl-stabilized diffusion flame.

CFD-Model Description: The experimental data for the SMA2 flame was collected starting from 6.8 mm downstream of the burner exit. To get the boundary conditions for the 3D case at the burner exit for the jet, annulus and co-flow, a 2D axi-symmetric non-reacting RANS simulation was performed. The 2D axi-symmetric grid is shown in Figure 58.

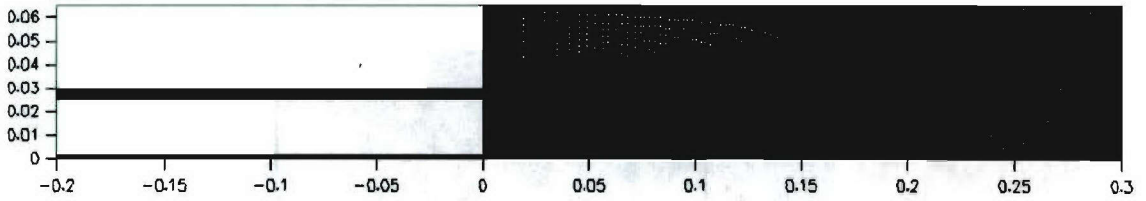

Figure 58. 2D Axi-Symmetric Grid for Non-Reacting SMA2 Case

The swirler and fuel inlets were made sufficiently long to allow the flow to fully develop at the burner exit. The boundary conditions at the swirler and jet inlets were varied till the velocity profile from the CFD simulations matched the velocity profile measured experimentally at 6.8 mm downstream of the burner exit. This provided a means to estimate the boundary conditions for the swirler and jet inlets in the 3D reacting RANS case. The combustor walls were given adiabatic boundary conditions and a constant pressure outlet was used for the exit boundary. The standard k-epsilon turbulence model was used for turbulence closure. The comparison between the experimental measurements and 2D axi-symmetric CFD RANS simulation for the non-reacting case is shown in Figure 59.

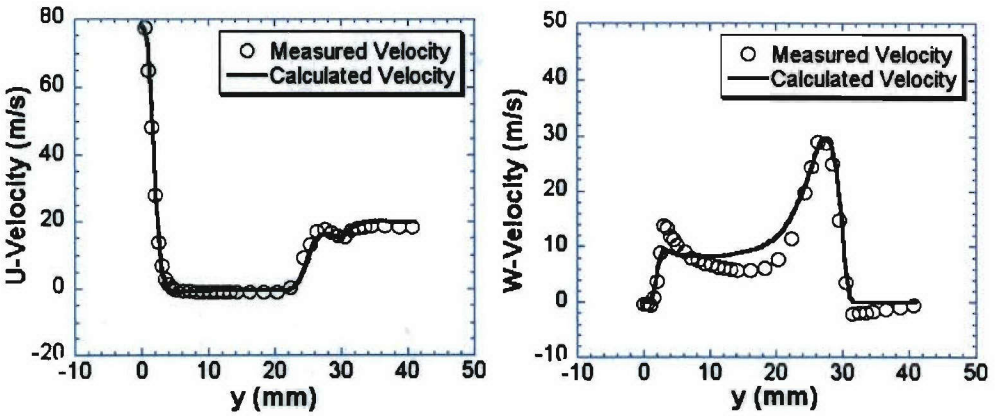

Figure 59. Axial and Tangential Velocity Comparisons Between Experimental and 2D Axi-Symmetric CFD Results at 6.8 mm Downstream of Burner Exit

The results shown in Figure 59 indicated that the right boundary conditions for the burner exit were now available to do a full 3D simulation. Excellent agreement in axial velocity was achieved. Agreement to the swirl velocity was similar to what has been report by other researchers (Masri, 2002). A 3D steady state RANS non-reacting case was then set up to get the initial conditions for the reacting case. The 3D grid is shown in Figure 60. The computational grid had a total of 1,263,600 cells.

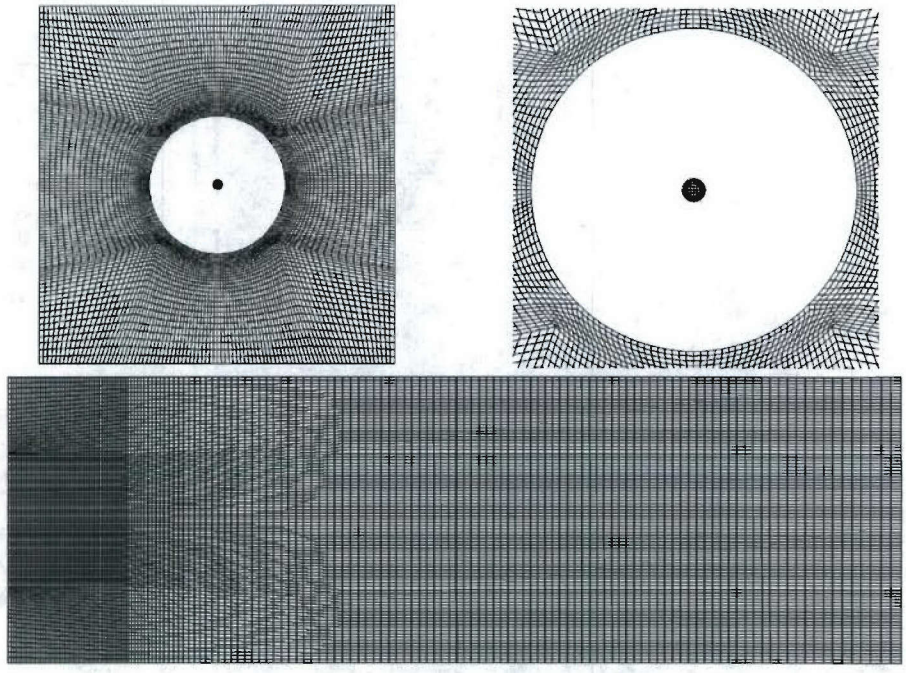

Figure 60. 3D RANS Grid, (a) Top Left: Front View, (b) Top Right: Close-Up of Front View and (c) Bottom: Side View

The standard k-epsilon model was used for turbulence closure with Schmidt and Prandtl numbers of 0.7. The inlet boundary conditions for the swirler annulus and the jet inlet were taken from the 2D axi-symmetric case previously discussed. Central differencing was used for all spatial discretizations. Figures 61 shows the axial velocity contours of the RANS result.

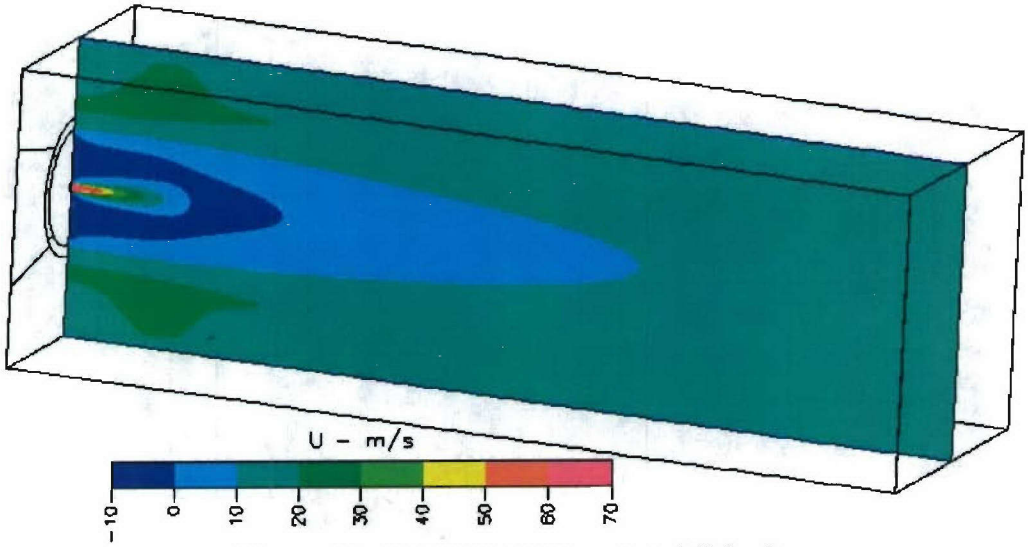

Figure 61. RANS Cold-Flow Axial Velocity

Figures 62-64 show the comparisons between the experimental measurements and CFD predictions of air velocity at different axial locations downstream of the burner exit.

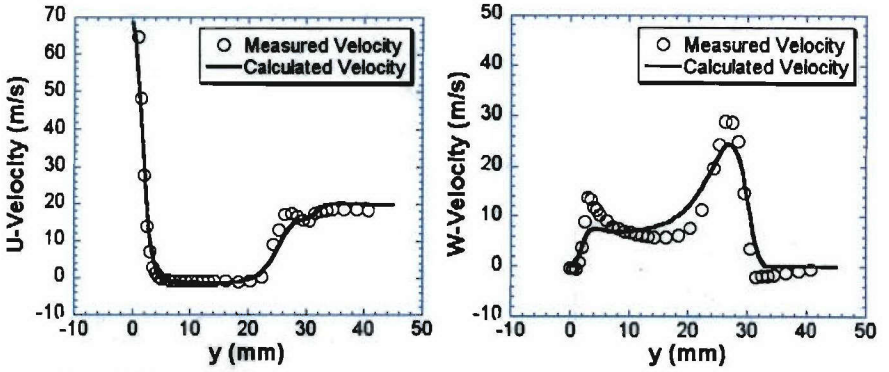

Figure 62. Axial and Tangential Velocity Comparisons Between Experimental and 3D CFD RANS Results at 6.8 mm Downstream of Burner Exit

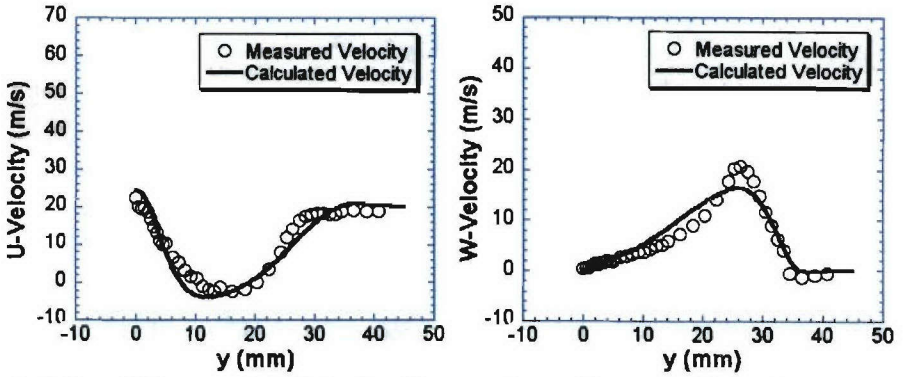

Figure 63. Axial and Tangential Velocity Comparisons Between Experimental and 3D CFD RANS Results at 30.0 mm Downstream of Burner Exit

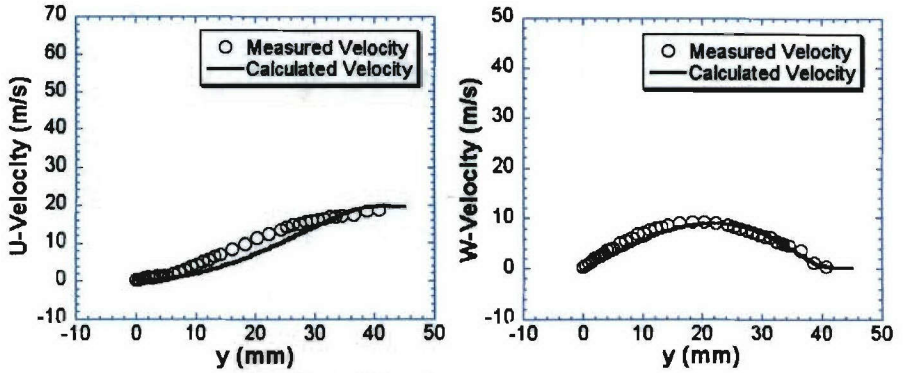

Figure 64. Axial and Tangential Velocity Comparisons Between Experimental and 3D CFD RANS Results at 100.0 mm Downstream of Burner Exit

The CFD results show good comparison to data for the non-reacting case. Some detailed features adjacent to the inlets are not well resolved, due to the coarser grid spacing of the 3D mesh. With the non-reacting case converged and matching well with experimental data, a reacting flow case was performed.

The reacting case used the same grid as was used by the non-reacting case above. To start with, the k-epsilon model was used for the turbulence closure and the single step assumed PDF model was used for modeling the effects of turbulence-chemistry interaction. The 3D reacting RANS case was initialized by the flow field obtained from the non-reacting case. Central differencing was used for all spatial discretizations. Contour plots of axial velocity and temperature are shown in Figures 65 and 66. Comparison to data at various axial locations of the 3D steady state, reacting-flow, and RANS simulations are shown in Figure 67.

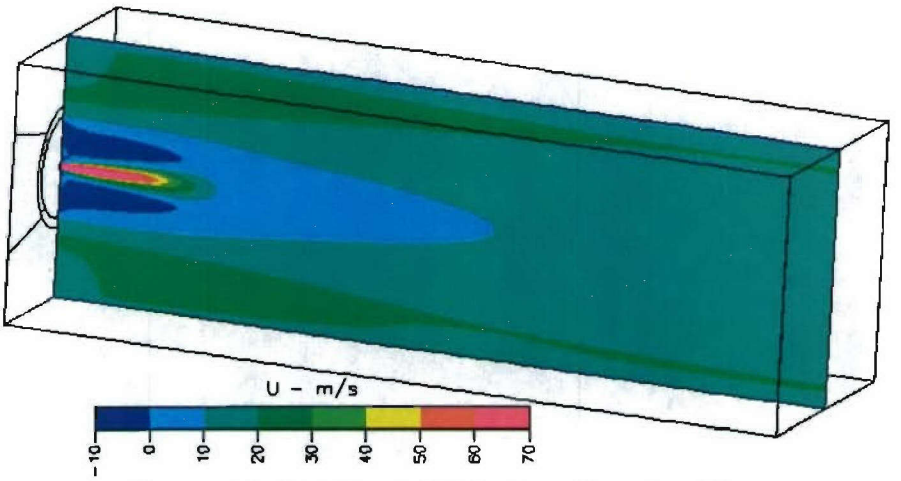

Figure 65. RANS Axial Velocity – Reacting Flow

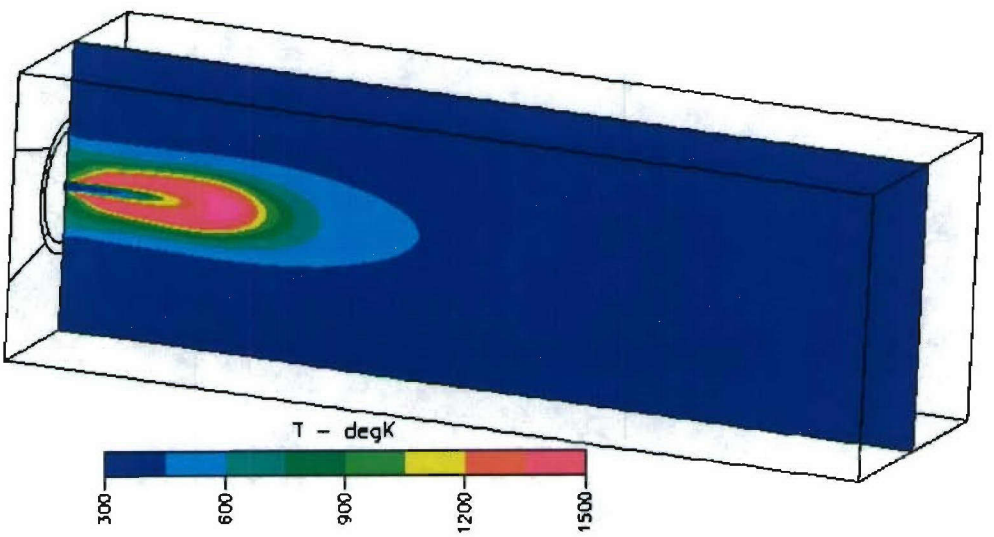

Figure 66. RANS Temperature – Reacting Flow

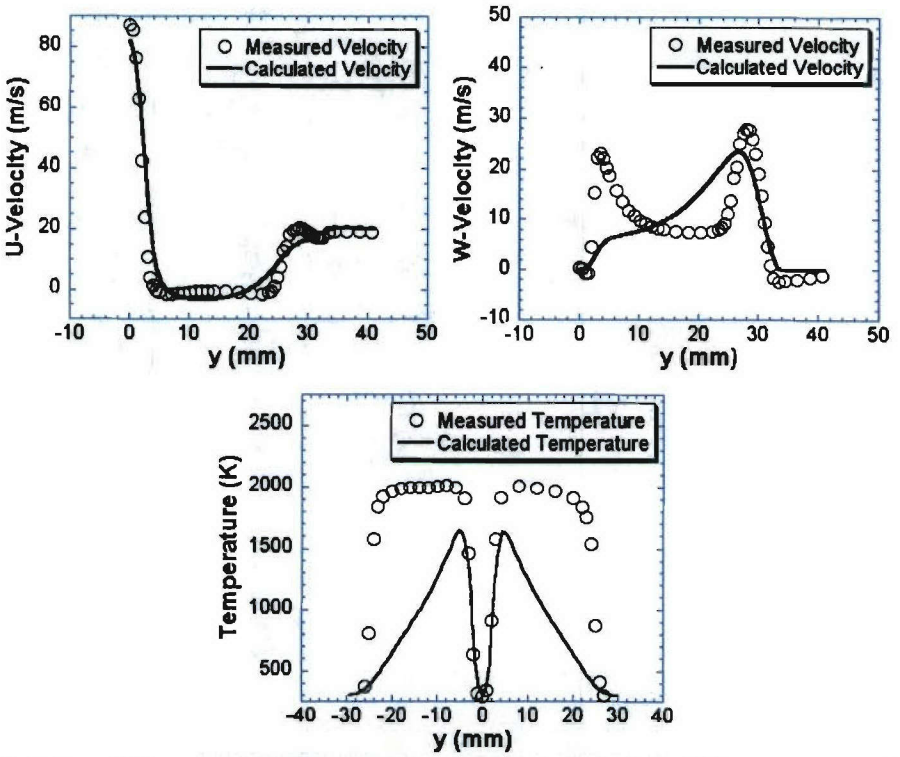

Figure 67. Axial and Tangential Velocity Comparisons (Top) and Temperature Comparisons (Bottom) Between Experimental and 3D CFD Results at 10.0 mm Downstream of Burner Exit

Figure 68 shows the comparison of the radial profiles of velocity components and temperature of the flow-field between the CFD results and the experimentally collected data at 10 mm downstream of the burner exit. The axial velocity predictions compare well with experimental measurements. However, the RANS simulation is not able to capture the two peaks in the tangential velocity as noted in the experiments. Traditionally RANS simulations have not performed very well for highly swirling and reacting flows. The temperature profile shape and magnitudes are also not well captured by the RANS simulation. The peak temperature is under-predicted by 350K, while the hot recirculation zone near the centerline is not captured quite as well. These results are similar to RANS results for this flame reported by Masri et al. (2002).

Figure 69 shows the comparisons of the CFD predictions with the experimental measurements 30 mm downstream of the burner exit. The axial and tangential velocities shapes are also not well captured by the RANS predictions. The velocity profiles predicted by the CFD calculations have been substantially dissipated near sharp changes in the experimental observed profiles.

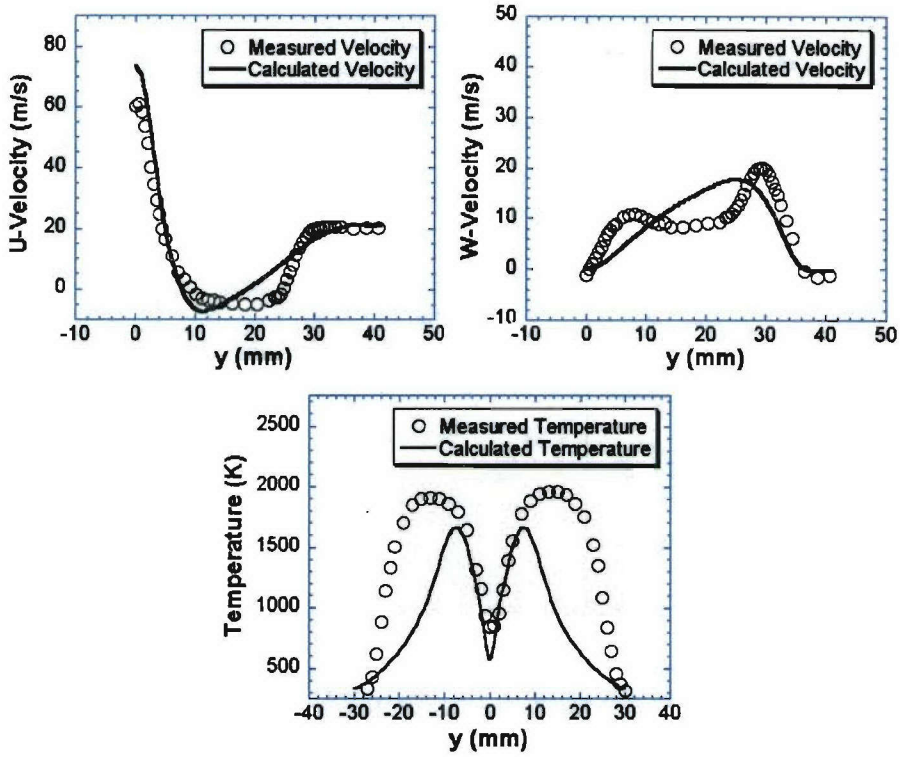

Figure 68. Axial and Tangential Velocity Comparisons (Top) and Temperature Comparisons (Bottom) Between Experimental and 3D CFD Results at 30.0 mm Downstream of Burner Exit

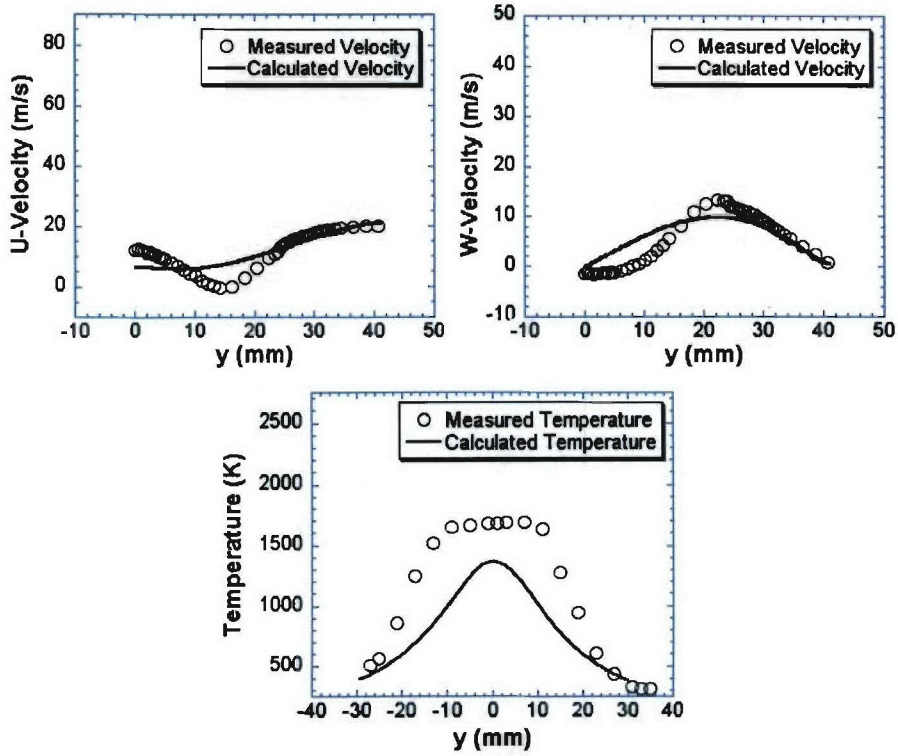

Figure 69. Axial and Tangential Velocity Comparisons (Top) and Temperature Comparisons (Bottom) Between Experimental and 3D CFD Results at 100.0 mm Downstream of Burner Exit

Figure 70 also shows the decay in the CFD predictions of the RANS simulation compared to the experimentally observed profiles. Such a behavior is representative of RANS calculations for highly swirling and reacting flows. It is expected that the LES results will be able to capture the relevant flow features much better than RANS.

A 3D LES calculation using the assumed PDF model was performed for the SMA2 case. The LDKM model was used for the subgrid closure. The grid used for the LES case is the same as RANS cases above. The Crank-Nicolson scheme with a blending factor of 0.6 is used for time integration while the central differencing scheme is employed for spatial discretizations. Figure 22 shows a snapshot of the LES temperature contours for the SMA2 case.

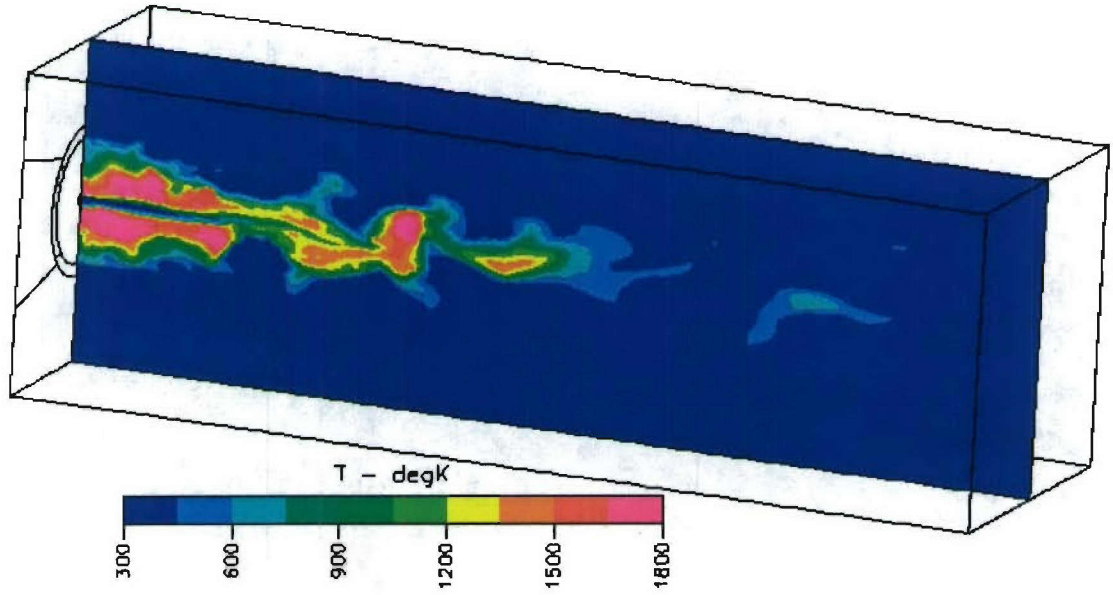

Figure 70. Snapshot of Temperature for the LES SMA2 Case

Comparison to data for two downstream axial locations of the 3D reacting LES simulation is shown in Figure 71-72.

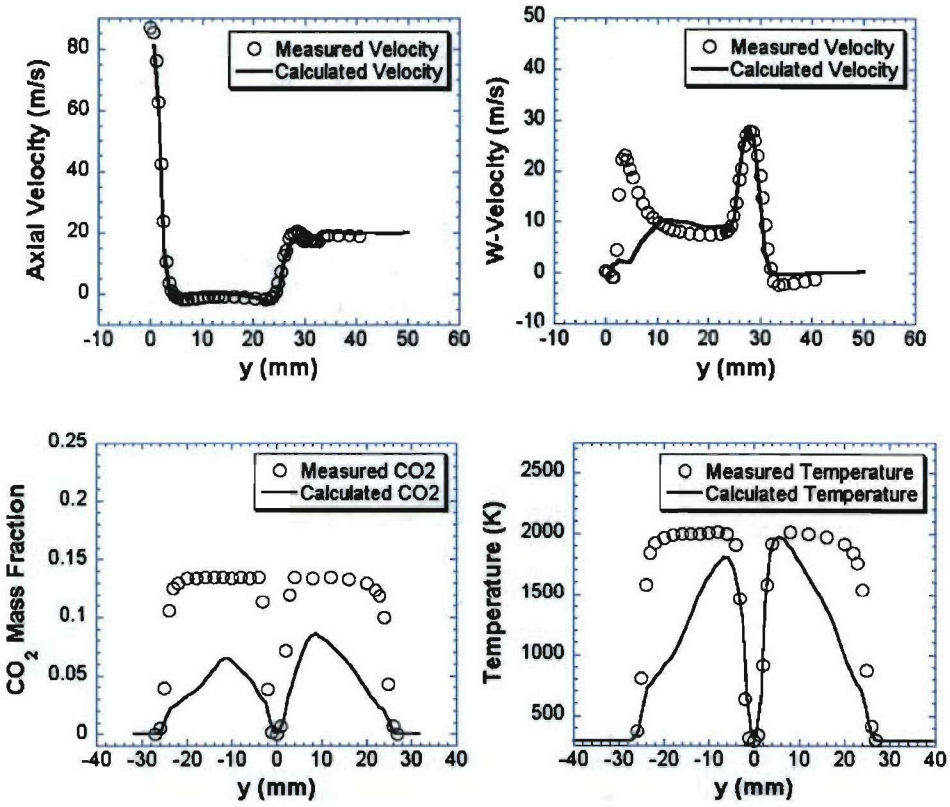

Figure 71. Axial Velocity (Top Left), Tangential Velocity (Top Right), CO_2 Mass Fraction (Bottom Left) and Temperature (Bottom Right) Comparisons Between Experimental and 3D CFD Results at 10.0 mm Downstream of Burner Exit

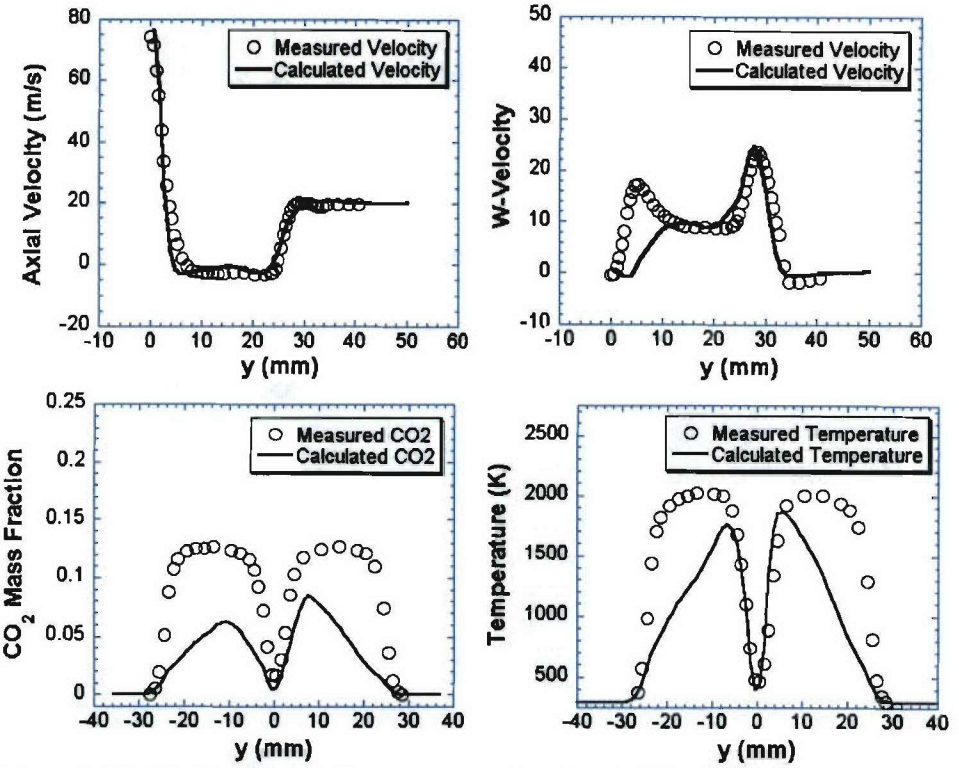

Figure 72. Axial Velocity (Top Left), Tangential Velocity (Top Right), CO_2 Mass Fraction (Bottom Left) and Temperature (Bottom Right) Comparisons Between Experimental and 3D CFD Results at 10.0 mm Downstream of Burner Exit

The LES results shows signs of improvement over the RANS results. The axial velocity profiles are almost perfectly captured, while the tangential velocity profiles seem to miss the first peak as observed in the experiments. The species predictions, although better than RANS, are not captured correctly. The temperature profile with LES is flatter and more consistent with the observed profile.

2D simulations were performed using both the 3 and 5 step mechanisms shown in Section 3.2. Also, results using the conventional single-step chemistry are shown for comparison purposes. Axial and tangential velocity results are shown in Figures 73 and 74, plotted at axial locations of 6.8, 30, and 100 mm downstream of the swirler exit. Initial results close to the boundary are good, but worsen farther downstream. Typically RANS has a difficult time with swirling flows, and these difficulties are highlighted in the results. Swirling flow velocities near the centerline underpredicted. This has also been shown by other researchers for RANS and LES is expected to result in improved velocity predictions. As shown in Figure 73c, chemistry also has a strong influence on the centerline velocity. Overall results with improved chemistry result in improved velocity predictions.

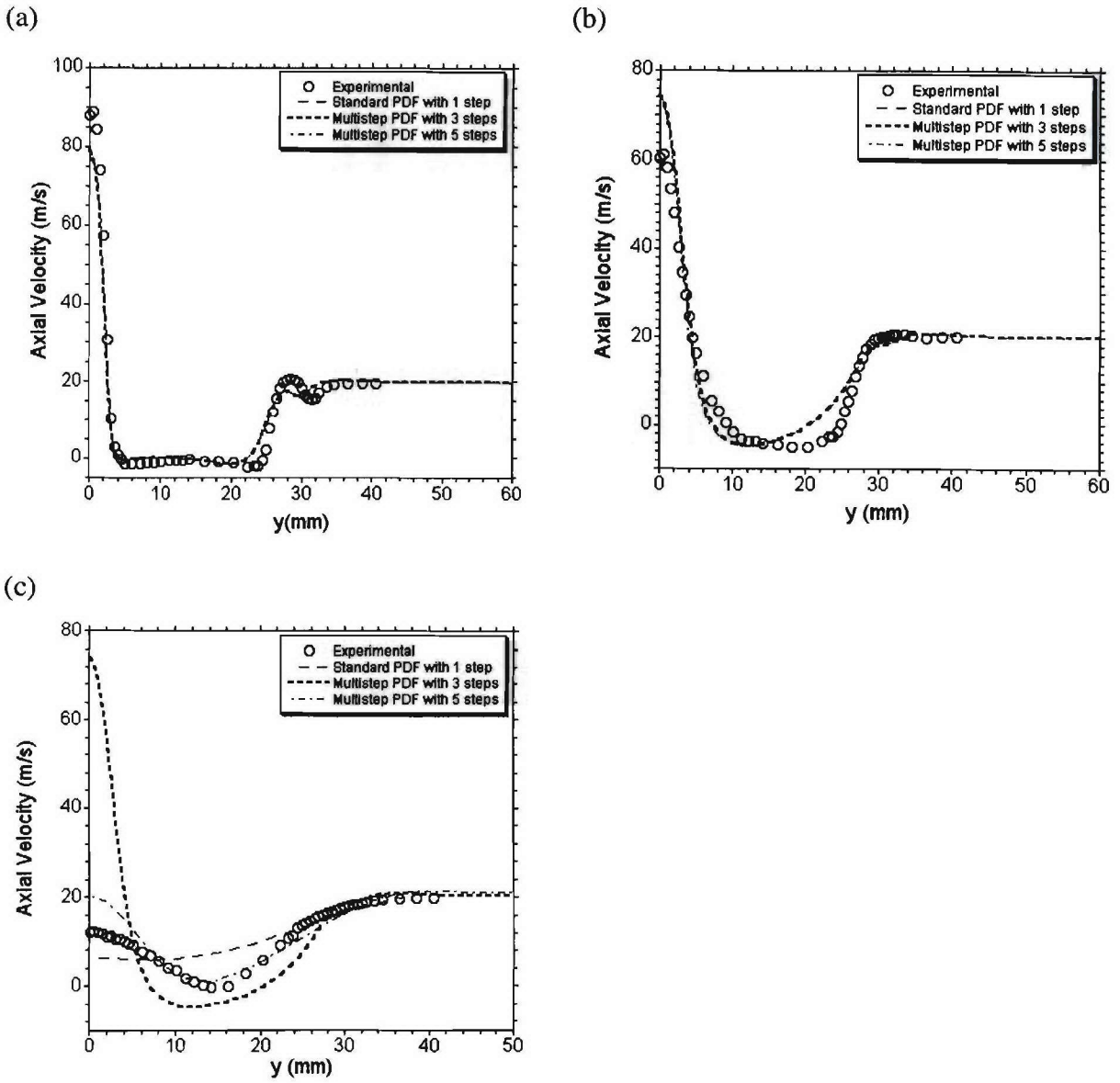

Figure 73. SMA2 Flame Axial (u-) Velocity Comparisons at Various Axial (x-) Locations Downstream of the Burner (a) x = 6.8mm (b) x = 30mm (c) = 100mm

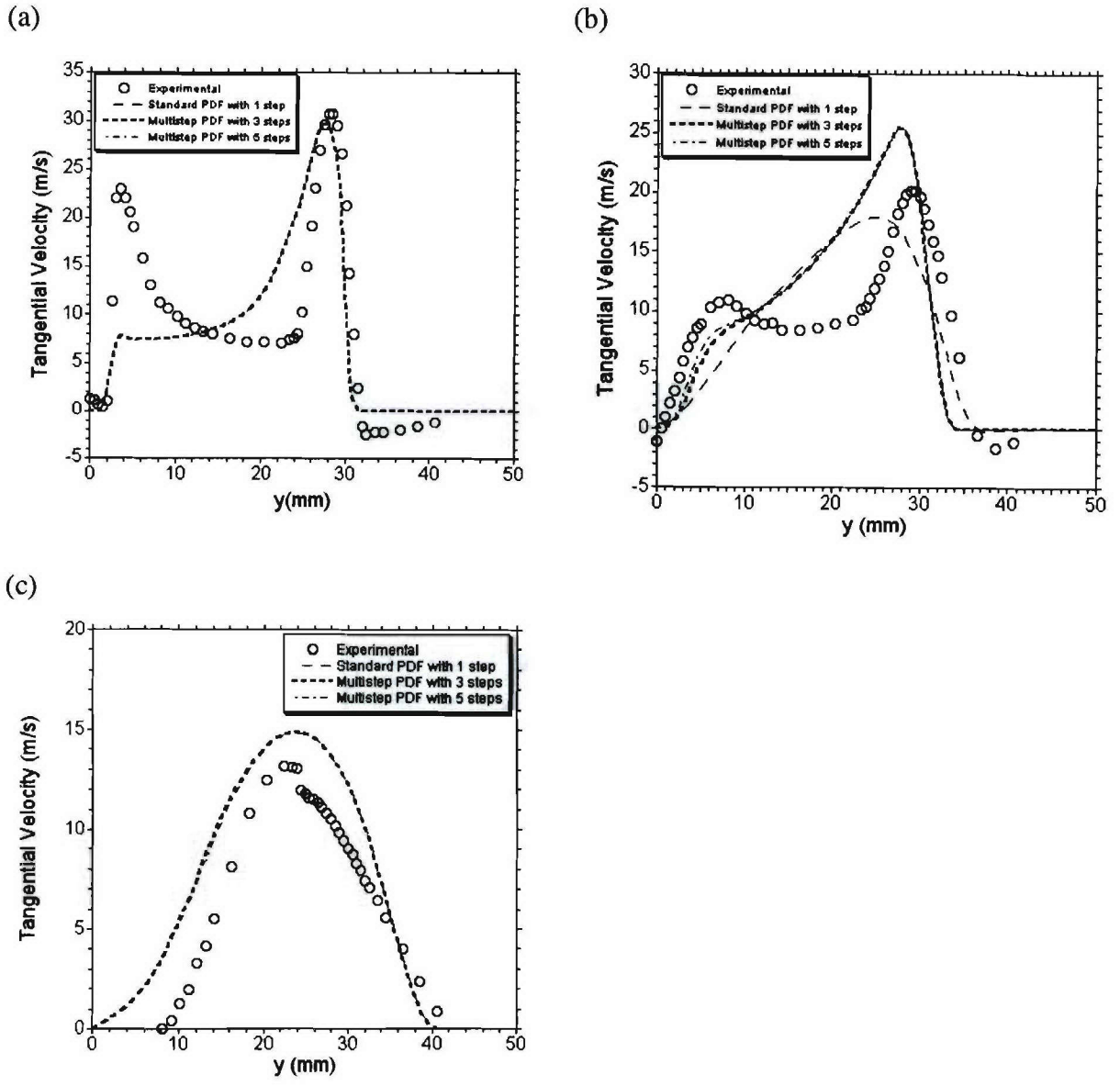

Figure 74. SMA2 Flame Tangential (w-) Velocity Comparisons at Various Axial (x-) Locations Downstream of the Burner (a) x = 6.8mm (b) x = 30mm (c) = 100mm

Temperature, CO_2, and CO results are plotted in Figures 75 through 77. Near the swirler, only minor differences with different chemical mechanisms are noted, with temperatures reaching the experimental values only near the centerline. Downstream, peak temperatures are much more realistic with both the 3 and 5 step mechanisms. Initial peak CO values are higher than measured. However, the multi-step mechanisms do a much better job of predicting CO concentrations at the 100 mm location. Here, the single-step mechanism results in essentially zero CO, while the multi-step mechanism results show high CO values on the centerline. The results show that multi-step mechanisms provide improved predictions, but there are still significant discrepancies between the predictions and the measured results. It is expected that

the application of LES will result in improved mixing and velocity predictions, and therefore will provide improved temperature and concentration results.

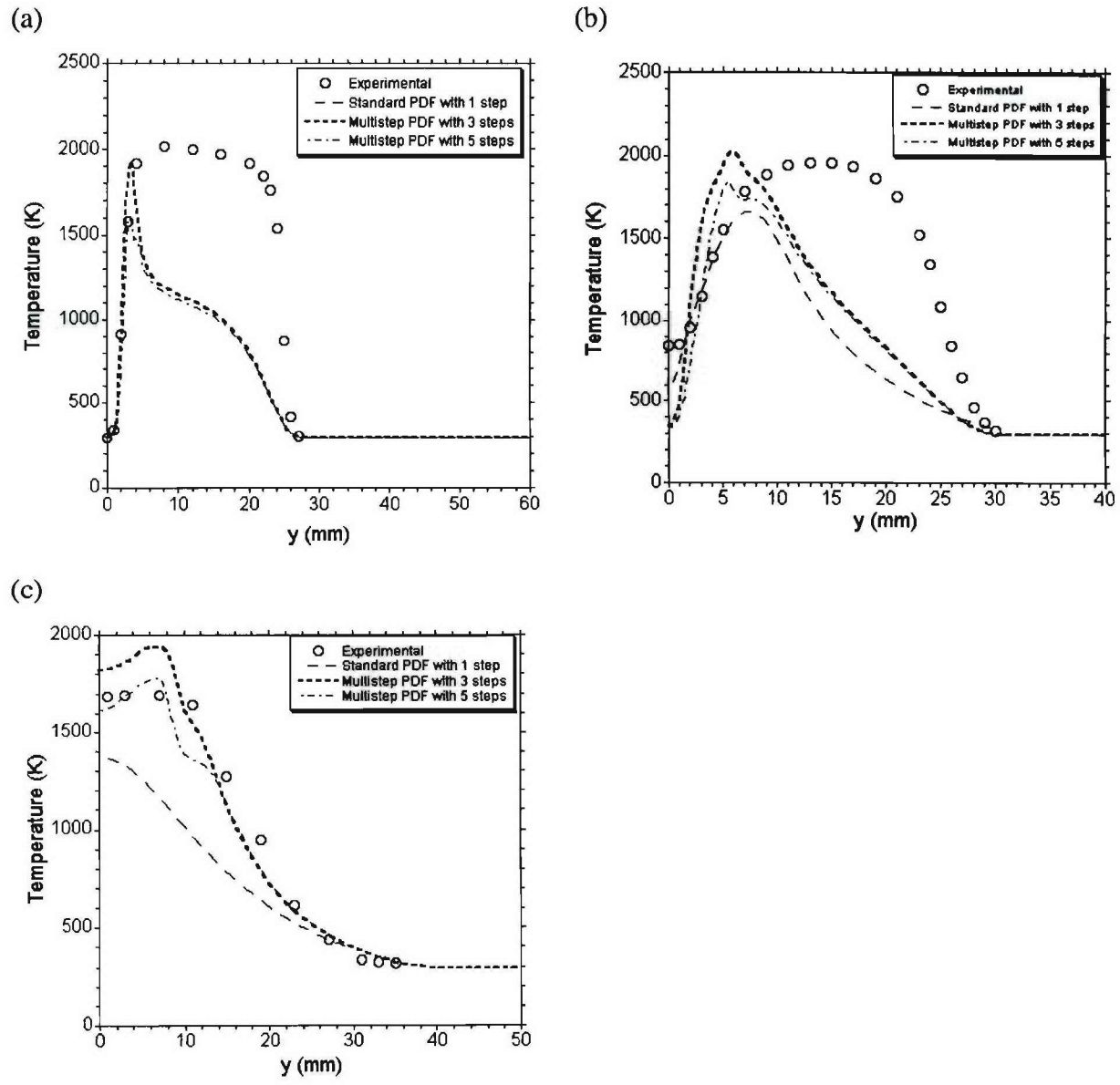

Figure 75. SMA2 Flame Temperature Comparisons at Various Axial (x-) Locations Downstream of the Burner. (a) x = 10mm (b) x = 30mm (c) = 100mm

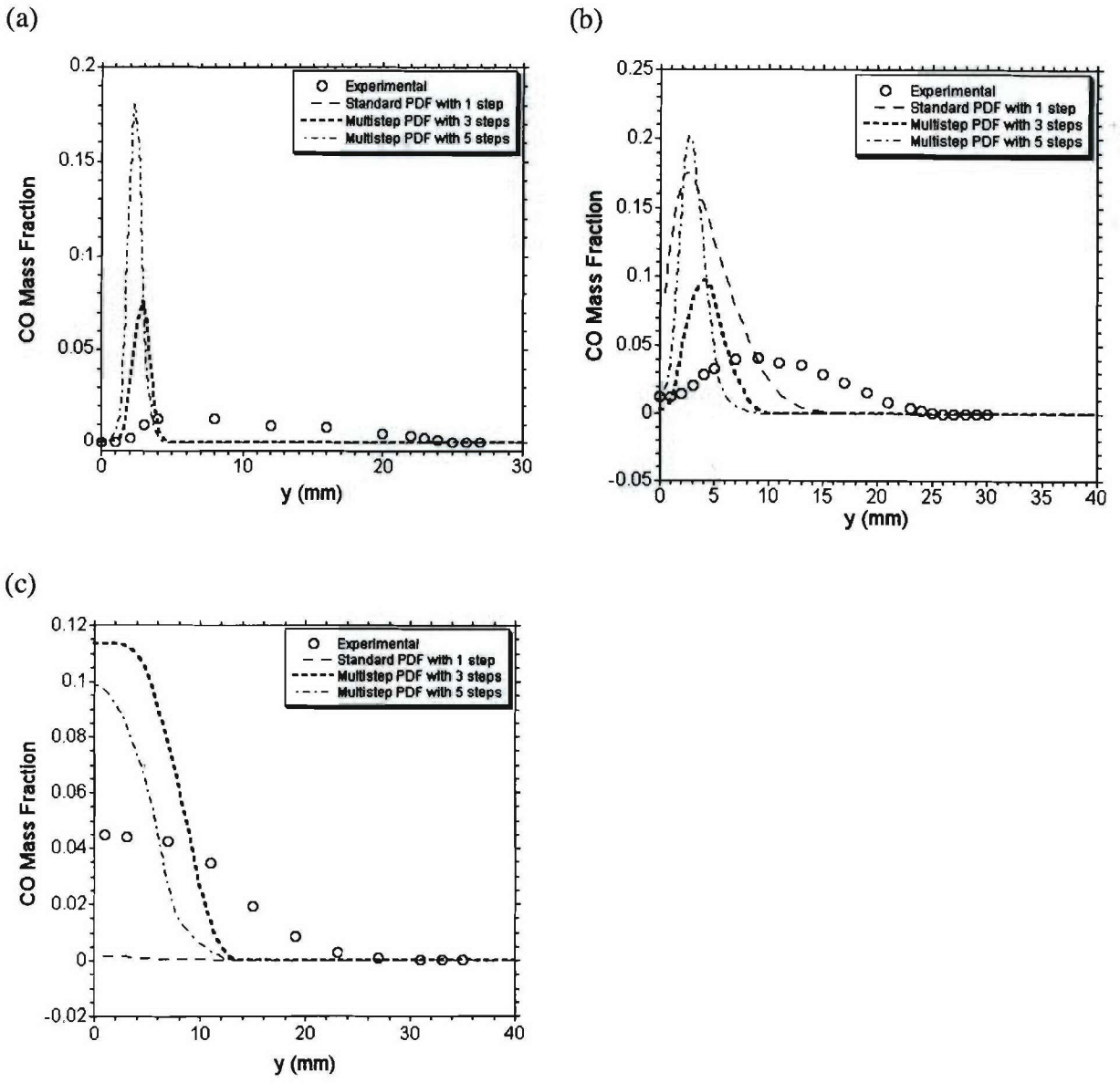

Figure 76. SMA2 Flame CO Mass Fraction Comparisons at Various Axial (x-) Locations Downstream of the Burner (a) x = 10mm (b) x = 30mm (c) = 100mm

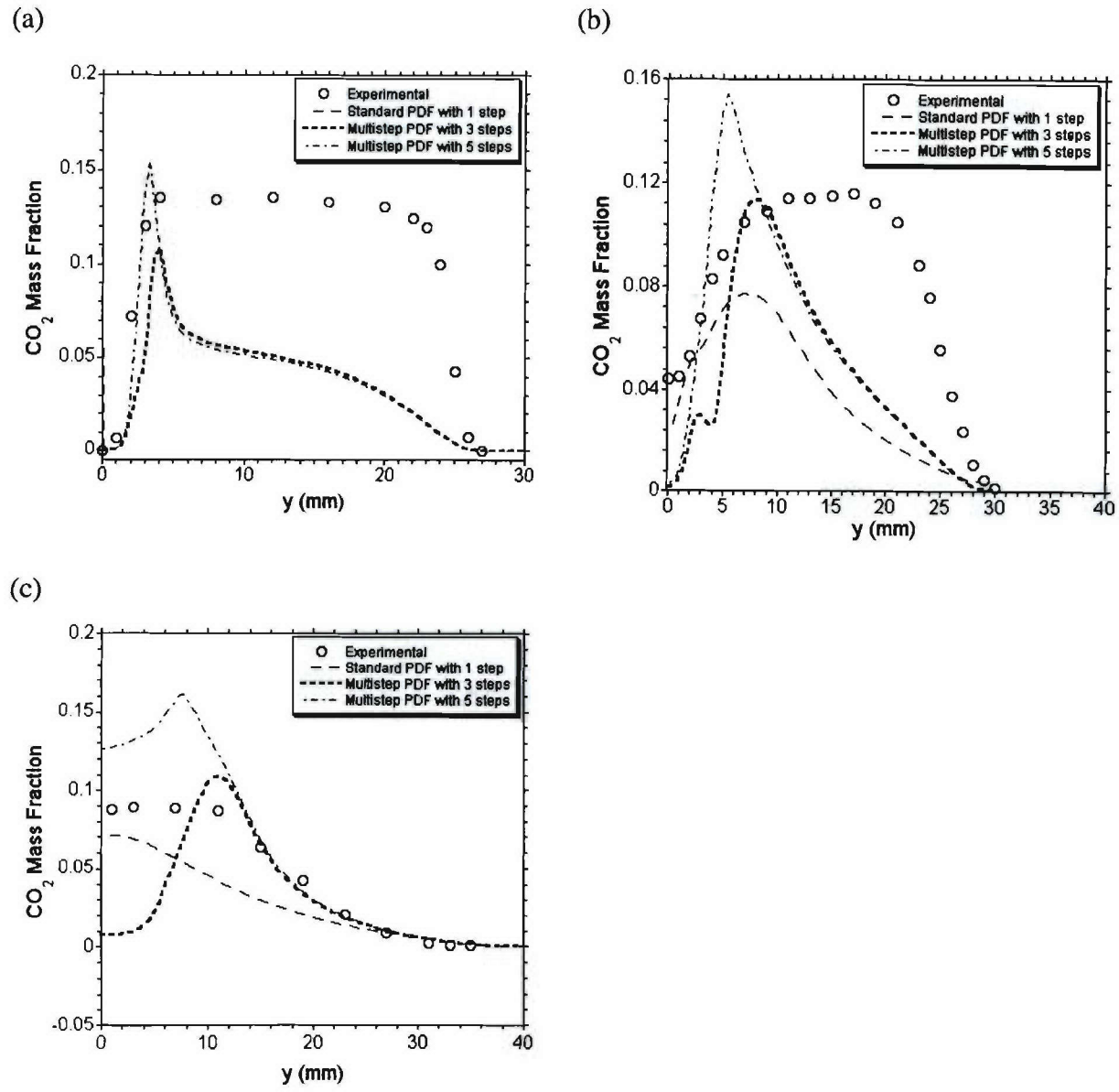

Figure 77. SMA2 Flame CO_2 Mass Fraction Comparisons at Various Axial (x-) Locations Downstream of the Burner (a) x = 10mm (b) x = 30mm (c) = 100mm

The 3D model of the SMA2 geometry with multi-step chemistry was attempted but a converged solution was not obtained. The unswirled center jet make obtaining converged 3D simulations difficult and the difficulty is significantly increased using the multi-step PDF model. As previously mentioned, the solvers available in CFD-ACE+ have proven to be inadequate for solving the coupled species and energy equations. The slow propagation of species information relative to the enthalpy results in unrealistically low temperatures in the flow domain, preventing convergence.

3.6.3 Sandia-D – Piloted Jet Flame

The third validation case selected is the Sandia-D flame. This flame has also been well characterized as part of the TNF workshop and is widely used as a validation case for diffusion flames. As opposed to the swirl-stabilized SMA2 flame discussed above, the Sandia-D flame is a pilot-stabilized flame. Figure 78 shows a close-up picture of the Sandia-D flame.

The Sandia-D flame provides a good validation case to test the turbulence-chemistry interaction model in conditions often observed in practical combustors. A brief summary of the experimental setup is presented below.

Figure 78. The Sandia-D Flame

The piloted, axi-symmetric burner has a main jet diameter of 7.2 mm and a pipe length exceeding 40 times the diameter, thus ensuring a fully developed flow at the pipe exit. The jet composition is 25% methane and 75% air by volume. The jet exit Reynolds number is 22,400. The diameter of the annular pilot is 18.2 mm and consists of 72 tiny premixed jets creating a homogenous distribution of temperature and gas composition. A mixture of acetylene, hydrogen, air, carbon dioxide and nitrogen is chosen with the same enthalpy and equilibrium composition as methane/air at 0.77 equivalence ratio for the pilot. The burner is placed concentrically to the exit nozzle of a wind tunnel that provides a laminar annular co-flow of filtered air at a speed of approximately 1.0 m/s. The jet exit is placed 20 mm above the exit of the co-flow nozzle. All gas flows before combustion are at room temperature.

CFD-Model Description: The experimental data for the Sandia-D case was collected starting from 1mm downstream of the burner exit, thus providing a good boundary condition to start the

calculations. Experimental profiles of the axial and radial velocities were specified at the fuel and air inlets. A constant axial velocity of 0.9 m/s was specified for the co-flow. The 3D grid for the CFD calculation is shown in Figure 79.

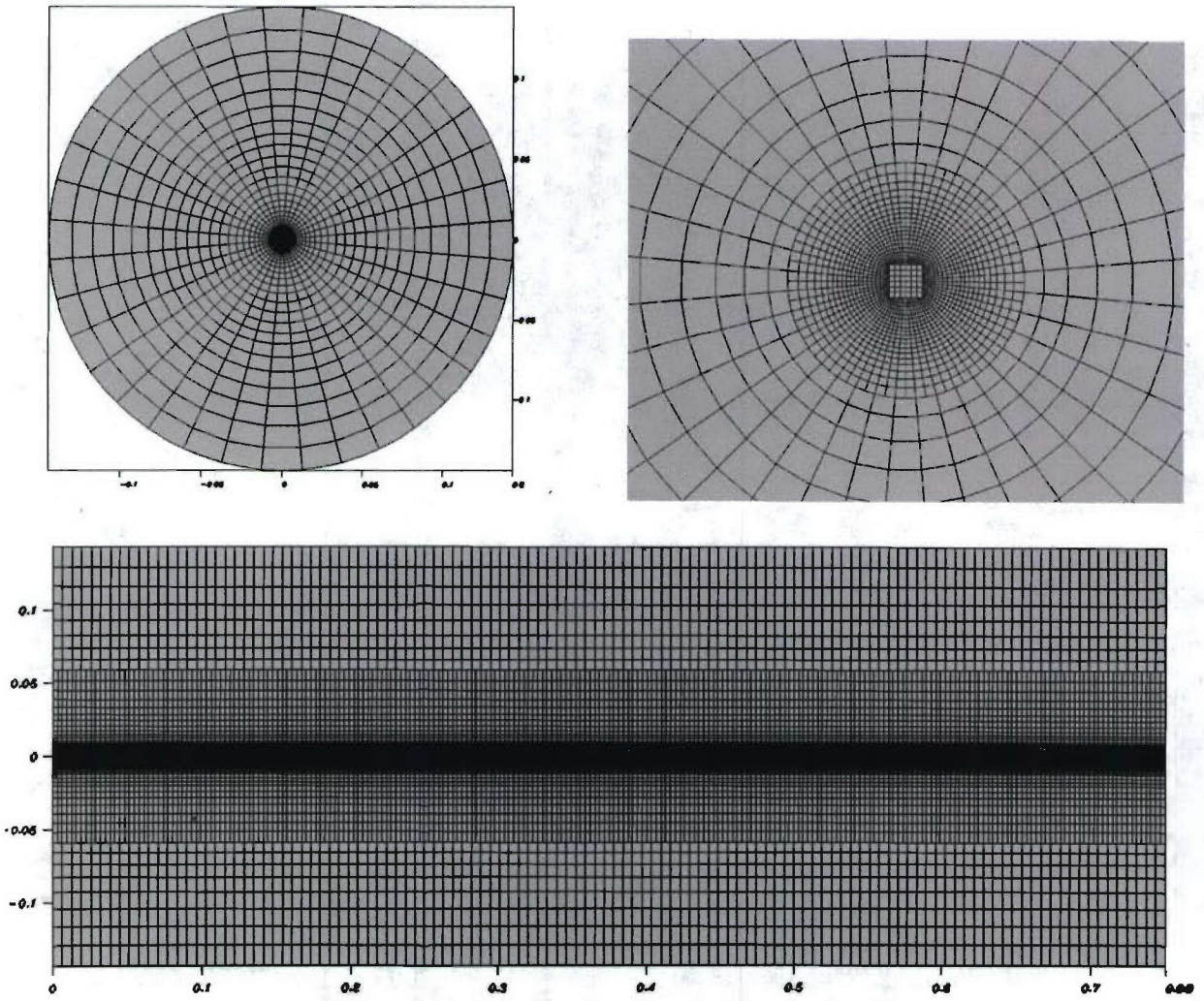

Figure 79. 3D RANS Grid, (a) Top Left: Front View, (b) Top Right: Close-Up of Front View and (c) Bottom: Side View

The RANS simulation used the k-ε turbulence model and the single step assumed PDF model for turbulence-chemistry closure. Upwind differencing was used for all spatial discretizations. Contour plots of axial velocity and temperature are shown in Figures 80 and 81. Comparison to data at various axial locations of the 3D steady state, reacting-flow, RANS simulation are shown in Figures 82-86.

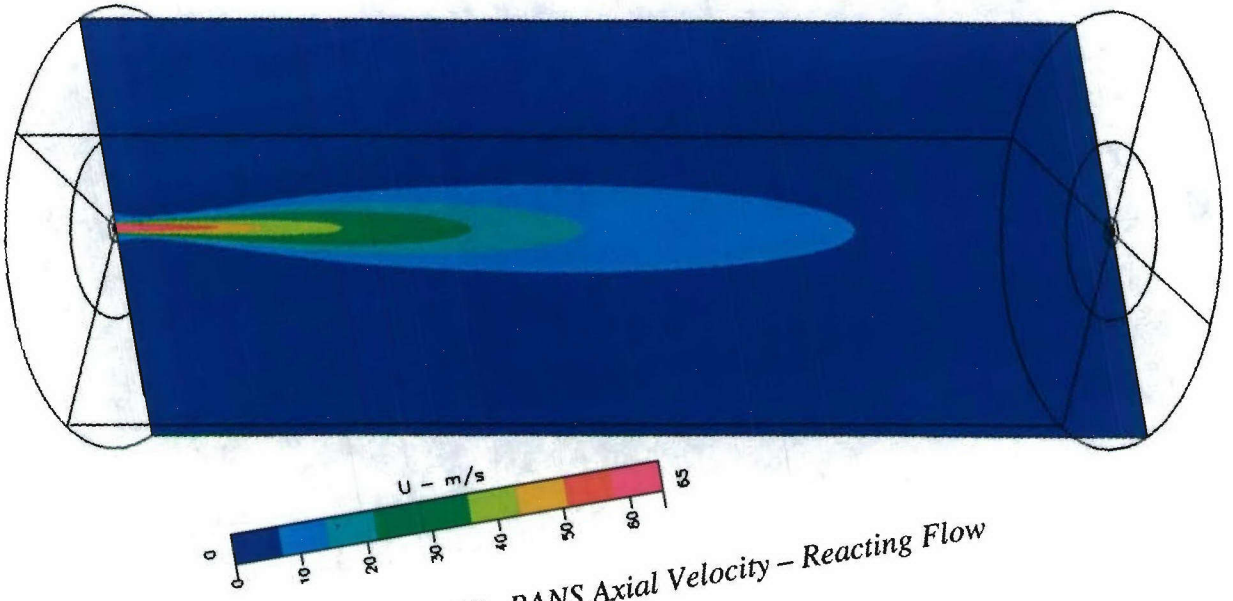

Figure 80. RANS Axial Velocity – Reacting Flow

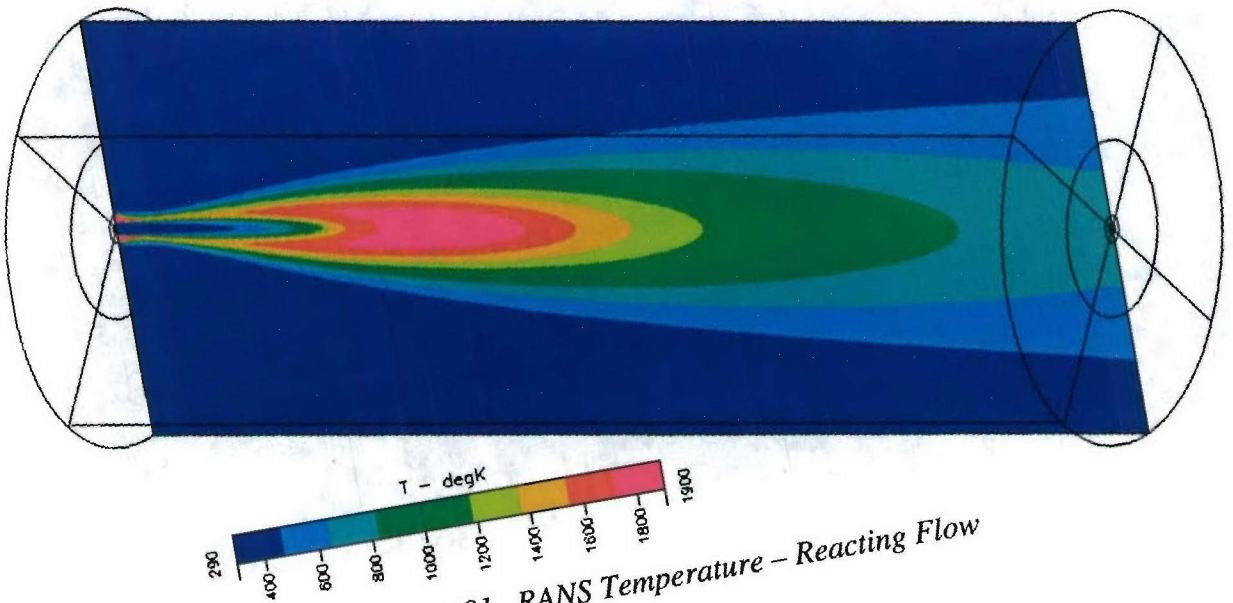

Figure 81. RANS Temperature – Reacting Flow

8503/8

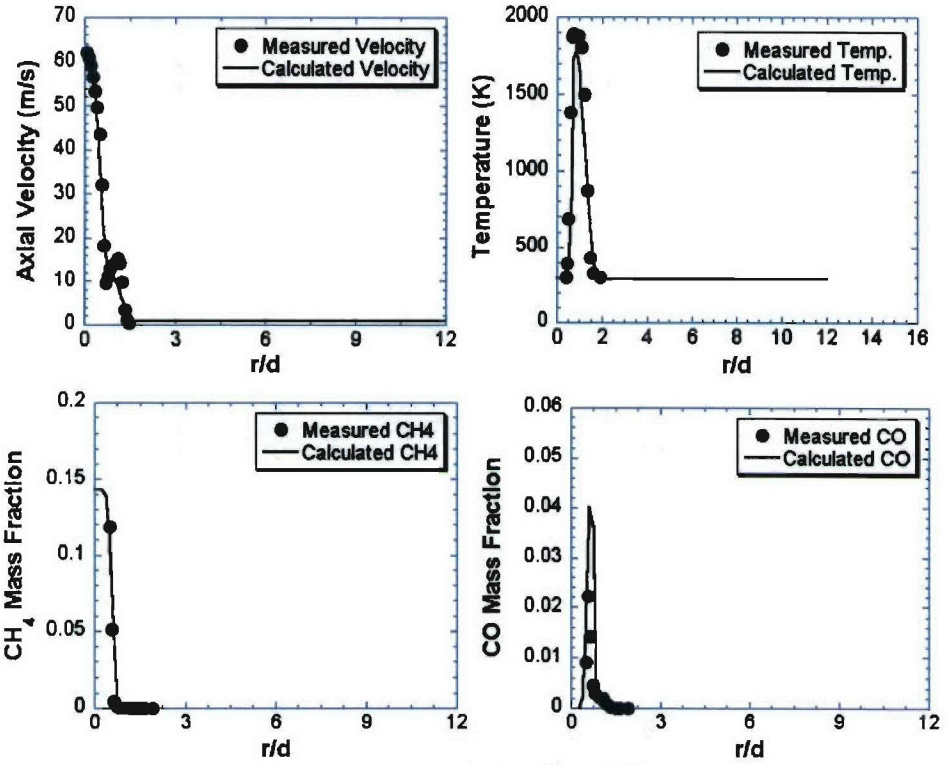

Figure 82. Axial Velocity (Top Left), Temperature (Top Right), CH_4 Mass Fraction (Bottom Left) and CO Mass Fraction (Bottom Right) Comparisons Between Experimental and 3D CFD Results at x/d = 1 Downstream of Burner Exit

As shown in Figure 82, the RANS results show excellent predictions for velocity, temperature and species just downstream of the burner exit. The CO mass fraction is over predicted, which will be corrected when the multi-step chemistry closure is used.

As we move downstream (Figure 83 and 84), the velocity predictions still show a great match with data, but the temperature predictions deteriorate. The reason for this discrepancy can be attributed to the high resolution required where the pilot holds the flame. RANS simulations cannot provide the rapid mixing and burning predictions in this zone. LES provides the necessary capabilities to resolve this region. Due to the temperature under-predictions, the species are also not well predicted in this region.

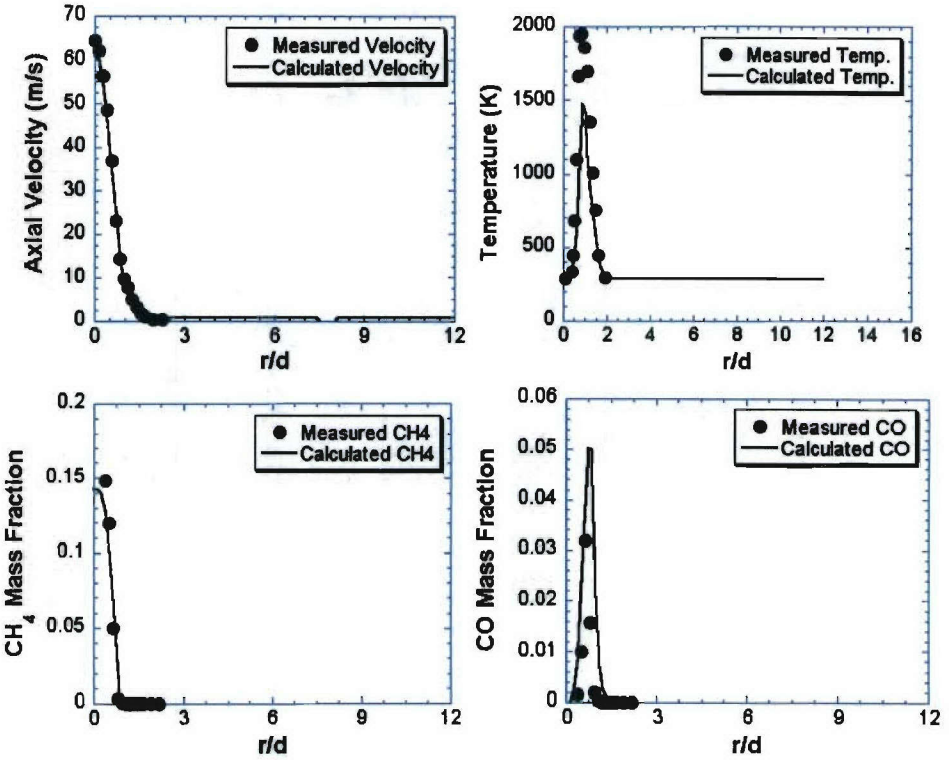

Figure 83. Axial Velocity (Top Left), Temperature (Top Right), CH_4 Mass Fraction (Bottom Left) and CO Mass Fraction (Bottom Right) Comparisons Between Experimental and 3D CFD Results at x/d = 3 Downstream of Burner Exit

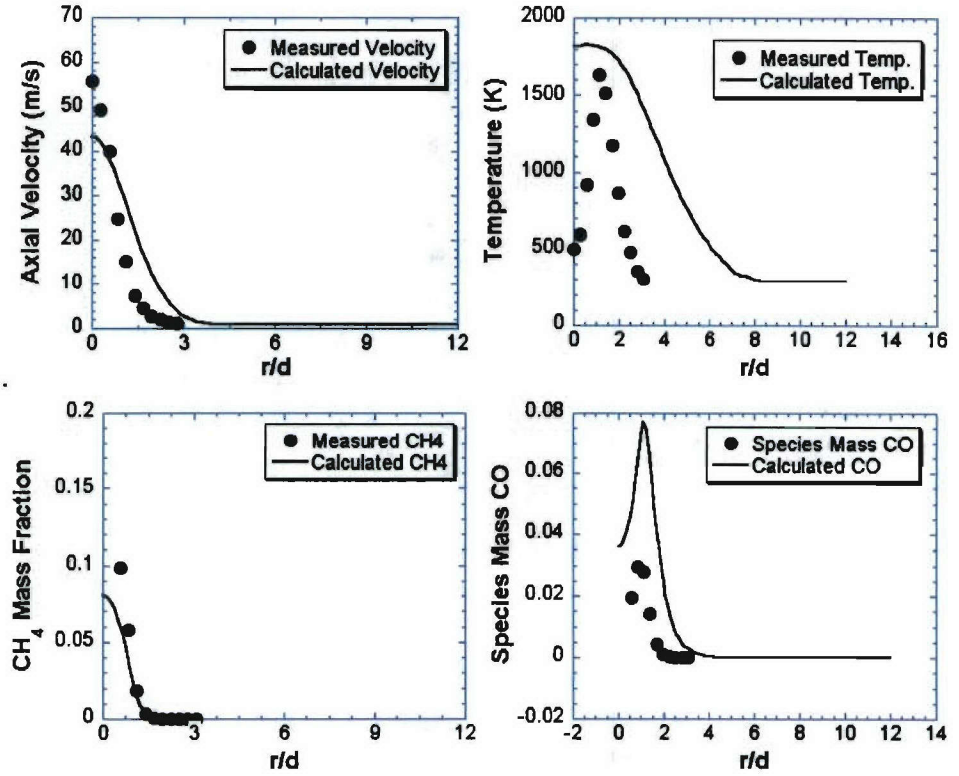

Figure 84. Axial Velocity (Top Left), Temperature (Top Right), CH_4 Mass Fraction (Bottom Left) and CO Mass Fraction (Bottom Right) Comparisons Between Experimental and 3D CFD Results at x/d = 15 Downstream of Burner Exit

Further downstream, RANS predictions again improve and velocity, temperature and species are well predicted (Figures 85 and 86). Downstream of this location, methane is all consumed and thus only CO predictions are shown.

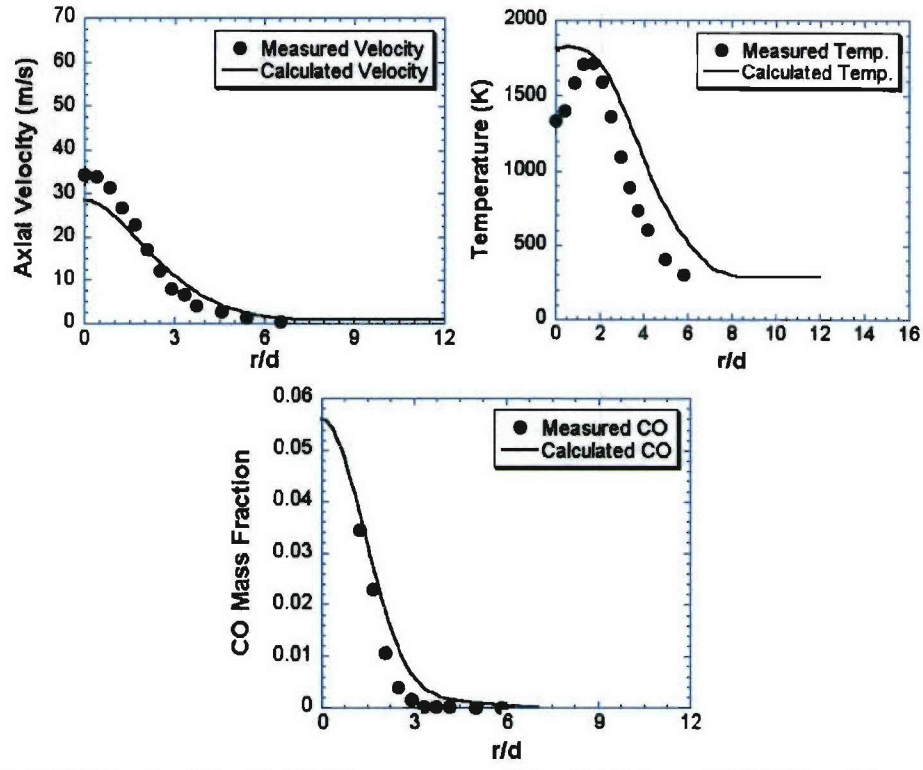

Figure 85. Axial Velocity (Top Left), Temperature (Top Right), and CO Mass Fraction (Bottom) Comparisons Between Experimental and 3D CFD Results at x/d = 30 Downstream of Burner Exit

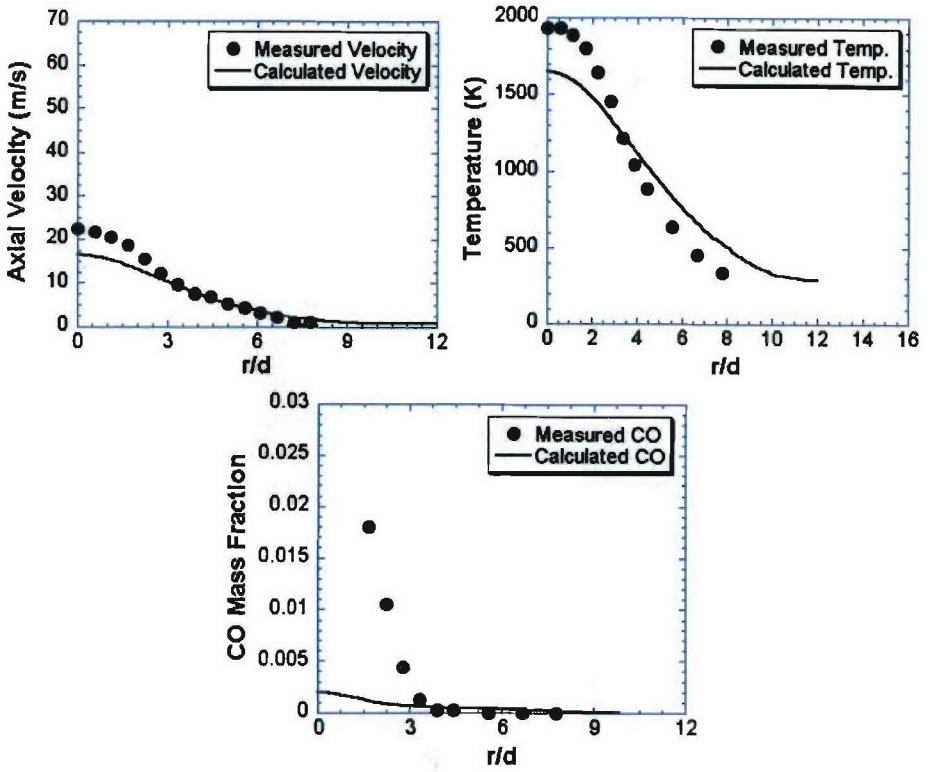

Figure 86. Axial Velocity (Top Left), Temperature (Top Right), and CO Mass Fraction (Bottom) Comparisons Between Experimental and 3D CFD Results at x/d = 45 Downstream of Burner Exit

A number of RNG k-ε turbulence model based RANS simulations, both 2D axi-symmetric and full 3D, were performed on the Sandia-D flame using multi-step chemistry. The simulations were carried out using both the 1-step mechanism as well as the multi-step assumed PDF model for turbulence-chemistry closure. Both the 3-step and 5-step mechanisms described in Section 3.4 were used. Upwind differencing was used for all spatial discretizations. The 2D axi-symmetric and the 3D RANS data were compared with the experimental data at various locations along the axis of the flame. The grid was also modified and improved from what was used in the simulation results shown previously. The grid features fine grid resolution near the centerline to capture the small center fuel jet and is adequate for both RANS and LES simulations. The grid is shown in Figure 87.

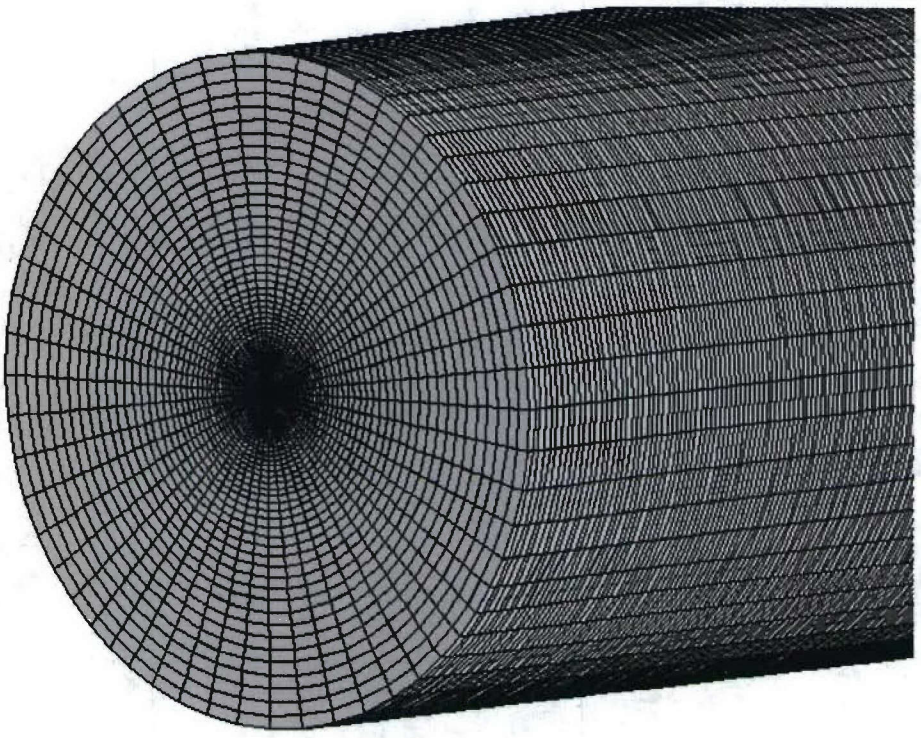

Figure 87. Grid for Both RANS and LES Simulations of the Sandia-D Flame

Plots of temperature and axial velocity for the multi-step RANS simulation are shown in Figures 88 and 89. Plots of CO and CO_2 mass fractions are shown in Figure 90 and 91. Since the measurements were taken in unconfined flow, the outer boundaries of the model were set to constant pressure exit boundaries. Table 17 shows the 5-step mechamism used for the simulation. The mechanism was generated from the GRI 3.0 detailed mechanism using a series of PSR/PFR calculations over an equivalence ratio range of 0.6 to 1.4 as described in Section 3.3

Table 17. Five-Step Methane Mechanism Accounting for CO and H_2

Reaction	ln(*A*)	E_a/R [K]	β	Reactant Order			
$2\ CH_4 + O_2 \Rightarrow 2\ CO + 4\ H_2$	34.53	35872	2.618	CH_4	1.109	O_2	1.572
$2\ H_2 + O_2 \Rightarrow 2\ H_2O$	34.53	8193	-1.421	O_2	1.363	H_2	1.063
$2\ CO + O_2 \Rightarrow 2\ CO_2$	34.53	13574	-0.098	O_2	1.601	CO	1.318
$2\ H_2O \Rightarrow 2\ H_2 + O_2$	12.01	50000	0.093	H_2O	1.242		
$2\ CO_2 \Rightarrow 2\ CO + O_2$	34.53	48202	-0.177	CO_2	1.507		

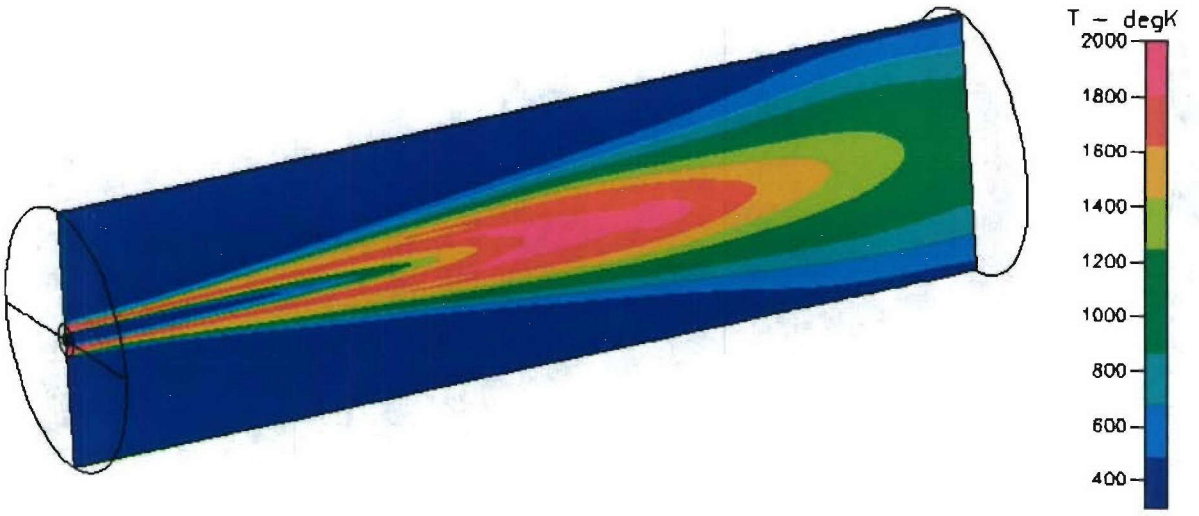

Figure 88. RANS Temperature Profiles for the Sandia-D Flame Using Multi-Step Chemistry

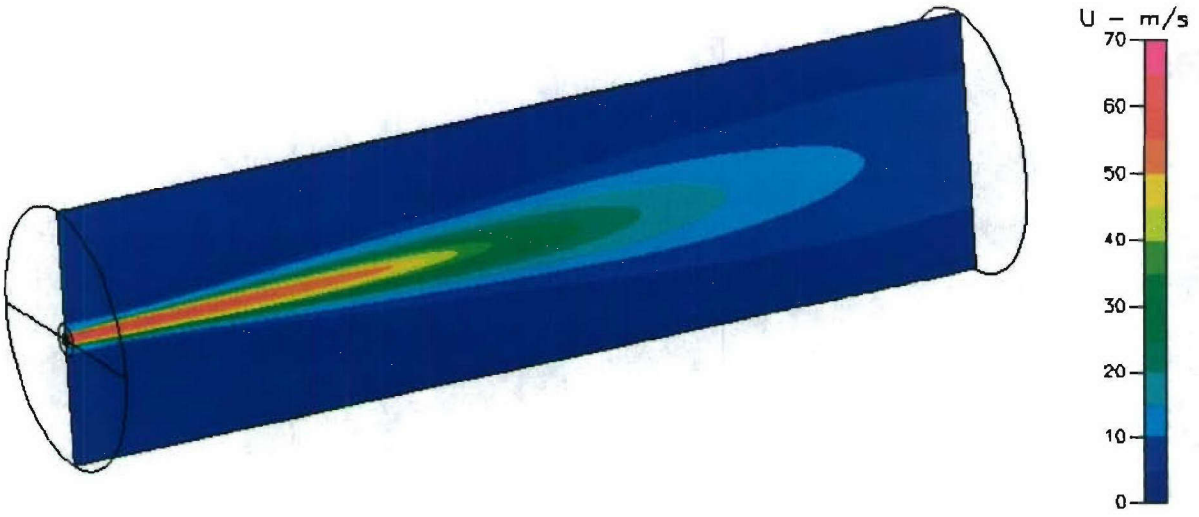

Figure 89. RANS Axial Velocity Profiles for the Sandia-D Flame Using Multi-Step Chemistry

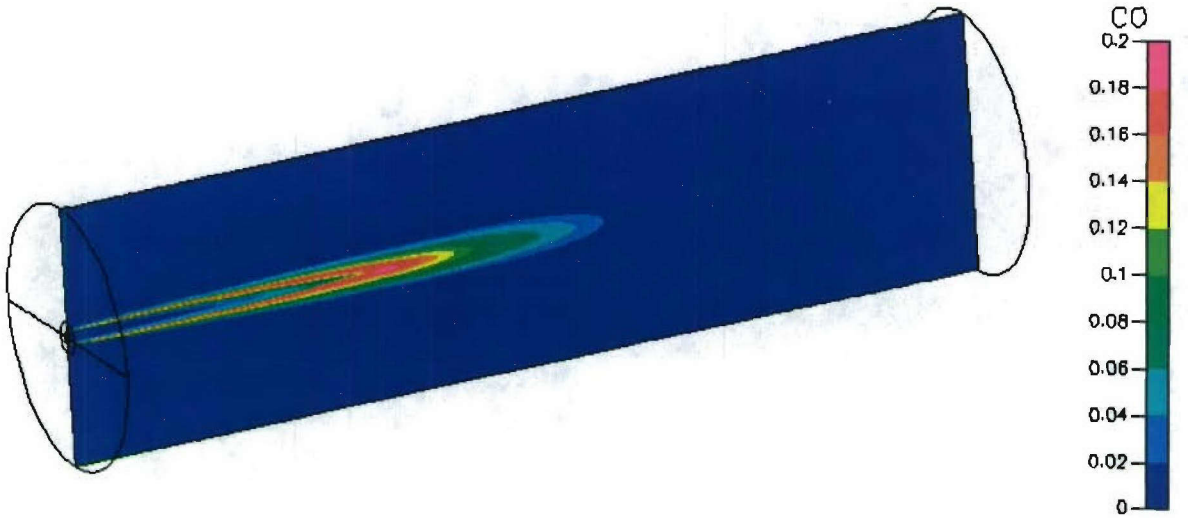

Figure 90. RANS CO Mass Fraction Profiles for the Sandia-D Flame Using Multi-Step Chemistry

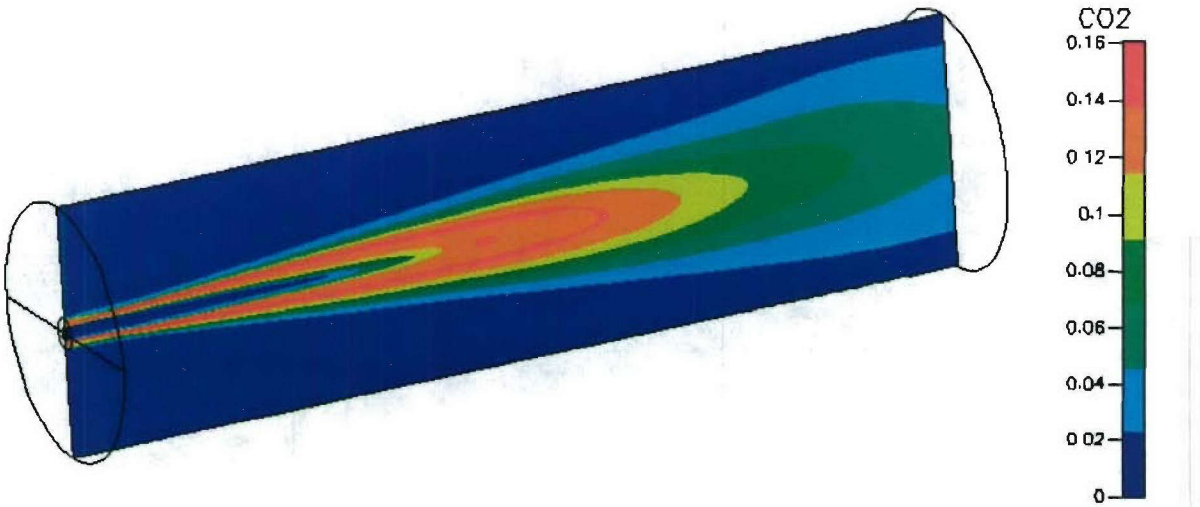

Figure 91. RANS CO_2 Mass Fraction Profiles for the Sandia-D Flame Using Multi-Step Chemistry

Figure 92 shows a comparison between the numerical and the experimental axial velocity data at four axial locations. It can be seen that among the 2D axisymmetric cases, the 5-step mechanism case compares best with experiments. As is to be expected, the 3D 5-step mechanism case comes closest to the experimental data among all the numerical cases. In Figure 92(a), the 3D 5-step mechanism case is able to resolve, to some extent, the sharp gradients in the axial velocity around $r/D = 1$. However, in Figure 92(c), at $x/D = 30$, the 3D RANS case over predicts the peak axial velocity at $r/D = 0$, even though it compares very well with the experimental data at larger radial distances.

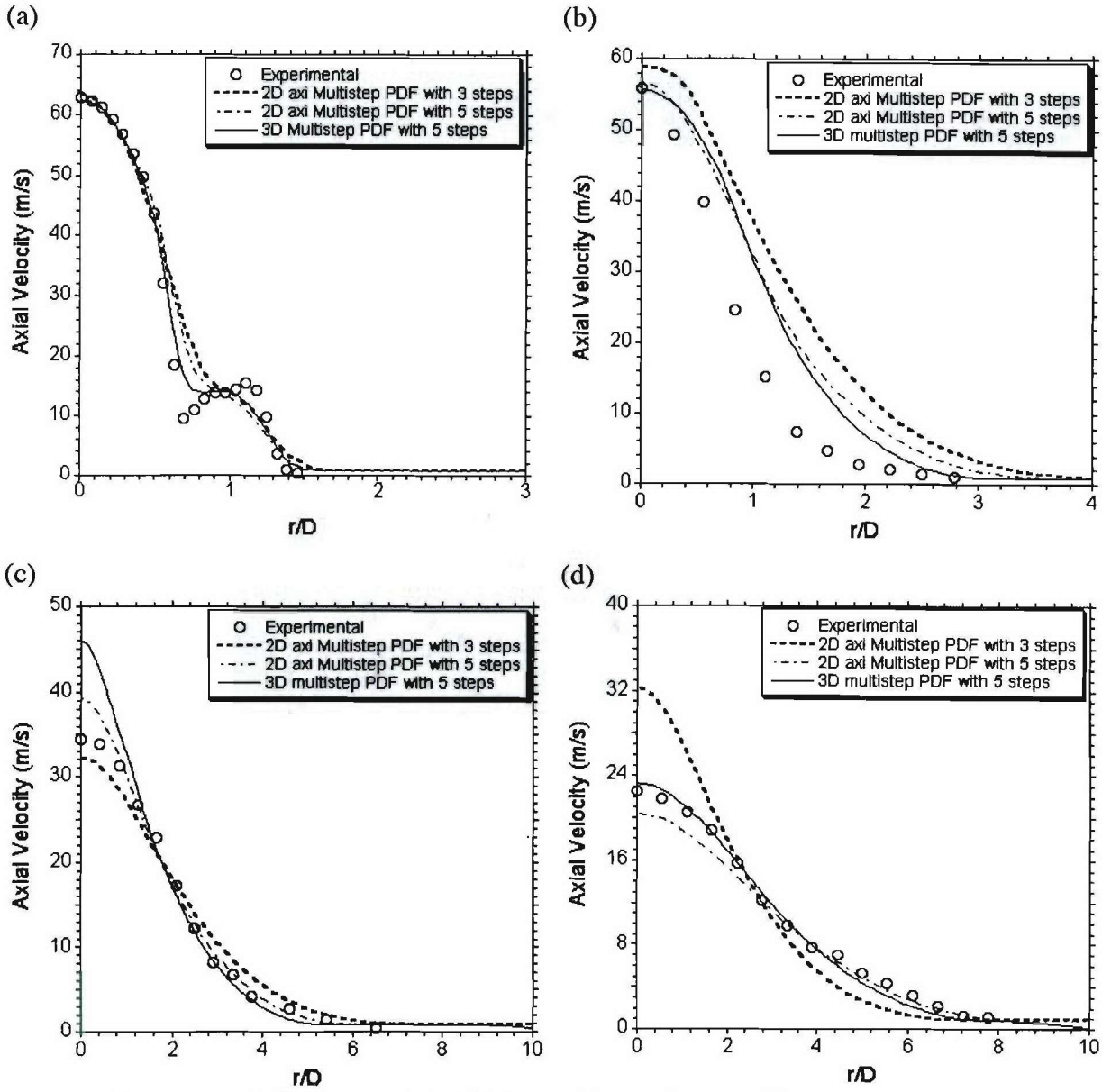

Figure 92. Sandia-D Flame Axial (u-) Velocity Comparisons at Various Axial (x-) Locations Downstream of the Burner (a) x/d = 1 (b) x/d = 15 (c) x/d = 30 (d) x/d = 45

A comparison of flame temperatures at various axial locations is shown in Figure 93. Again, the 3D 5-step RANS case does the best. The improvement in predictions compared to the corresponding 2D axisymmetric 5-step case is quite significant. At all the four axial locations, the 3D 5-step case shows remarkably good agreement with the experiments, especially the peak temperatures. Even at far downstream locations such as at $x/D = 45$, shown in Figure 93(d), the 3D case does a much better job than all the 2D cases. As is to be expected, 2D 1-step RANS case performs rather poorly in predicting both the magnitude and the radial locations of the peak temperatures at all the axial locations shown.

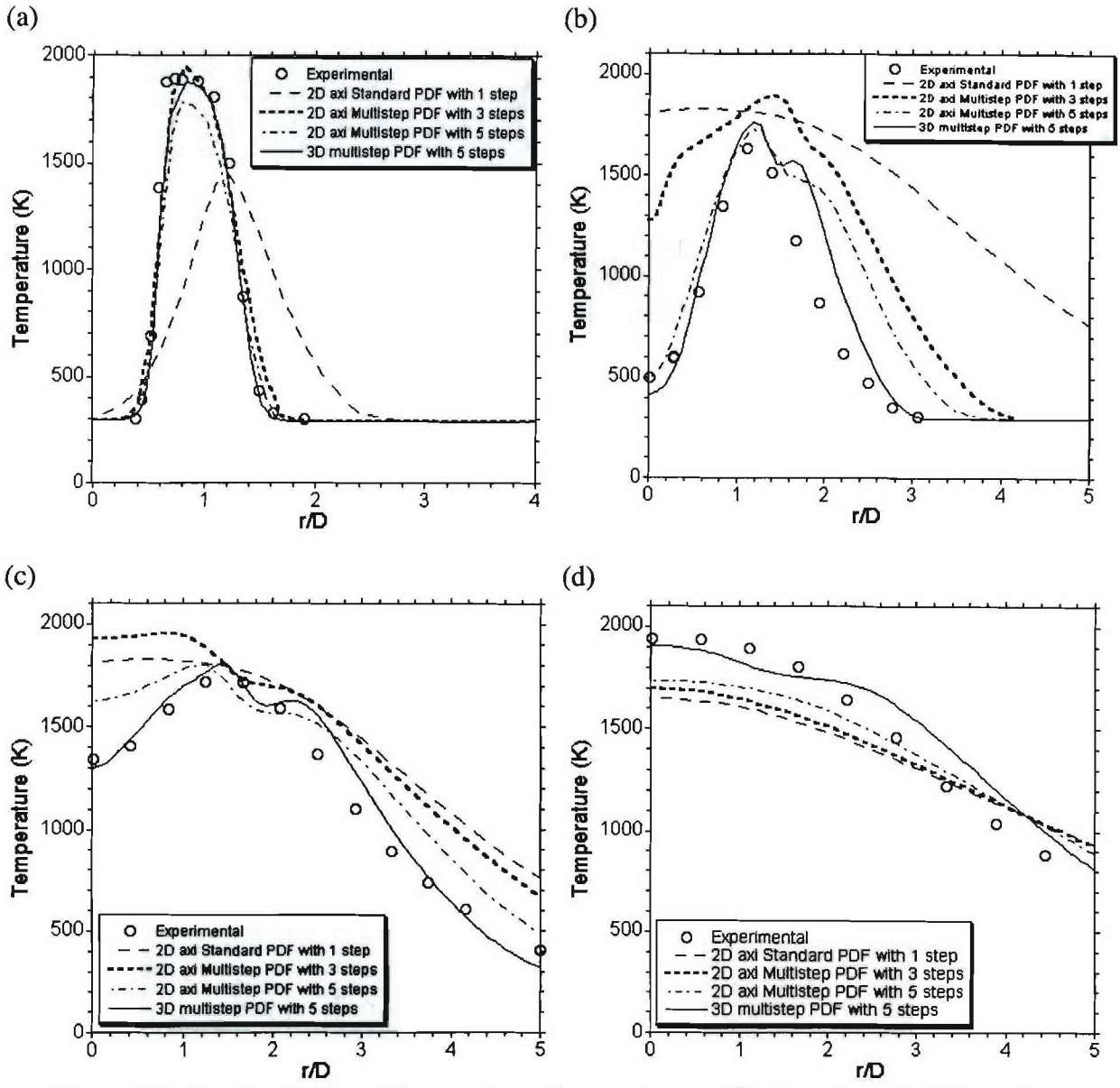

Figure 93. Sandia-D Flame Temperature Comparisons at Various Axial (x-) Locations Downstream of the Burner. (a) x/d = 1 (b) x/d = 15 (c) x/d = 30 (d) x/d = 45

The CH_4 species mass fractions are shown in Figure 94. At the first two axial locations, $x/D = 1$ and $x/D = 15$, again the 3D case compares well with the experiments, especially in predicting the peak CH_4 mass fractions. However, at subsequent downstream locations, the comparison between the 3D and the experimental data deteriorates. Both the 2D and the 3D 5-step chemistry cases indicate a near-complete burnout of CH_4 at the two farther downstream axial locations. The CO mass fraction profiles are shown in Figure 95. Here, none of the 2D or the 3D cases shows good comparison with experiments. However, in general, the multi-step chemistry cases better capture the trends in the CO concentration profiles.

Finally, the numerical and experimental data for the CO_2 mass fractions are compared in Figure 96. The multi-step chemistry cases show an improvement in predictions. In particular, the 2D and the 3D 5-step mechanism cases accurately capture the radial locations of the peak CO_2 concentrations, even though the peak magnitudes are not captured well. The 1-step mechanism case, as usual, performs the worst.

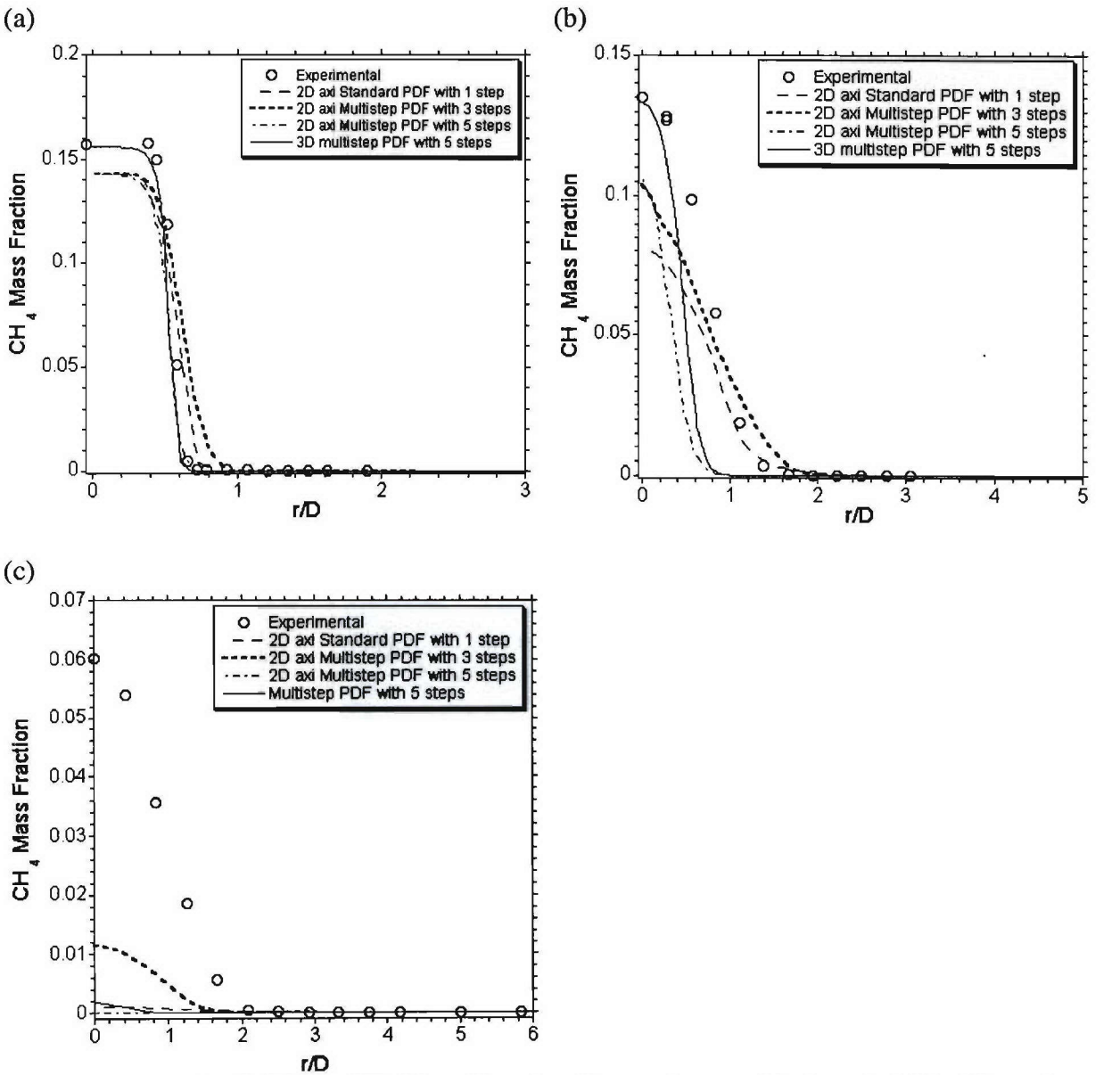

Figure 94. Sandia-D Flame CH_4 Mass Fraction Comparisons at Various Axial (x-) Locations Downstream of the Burner (a) x/d = 1 (b) x/d = 15 (c) x/d = 30

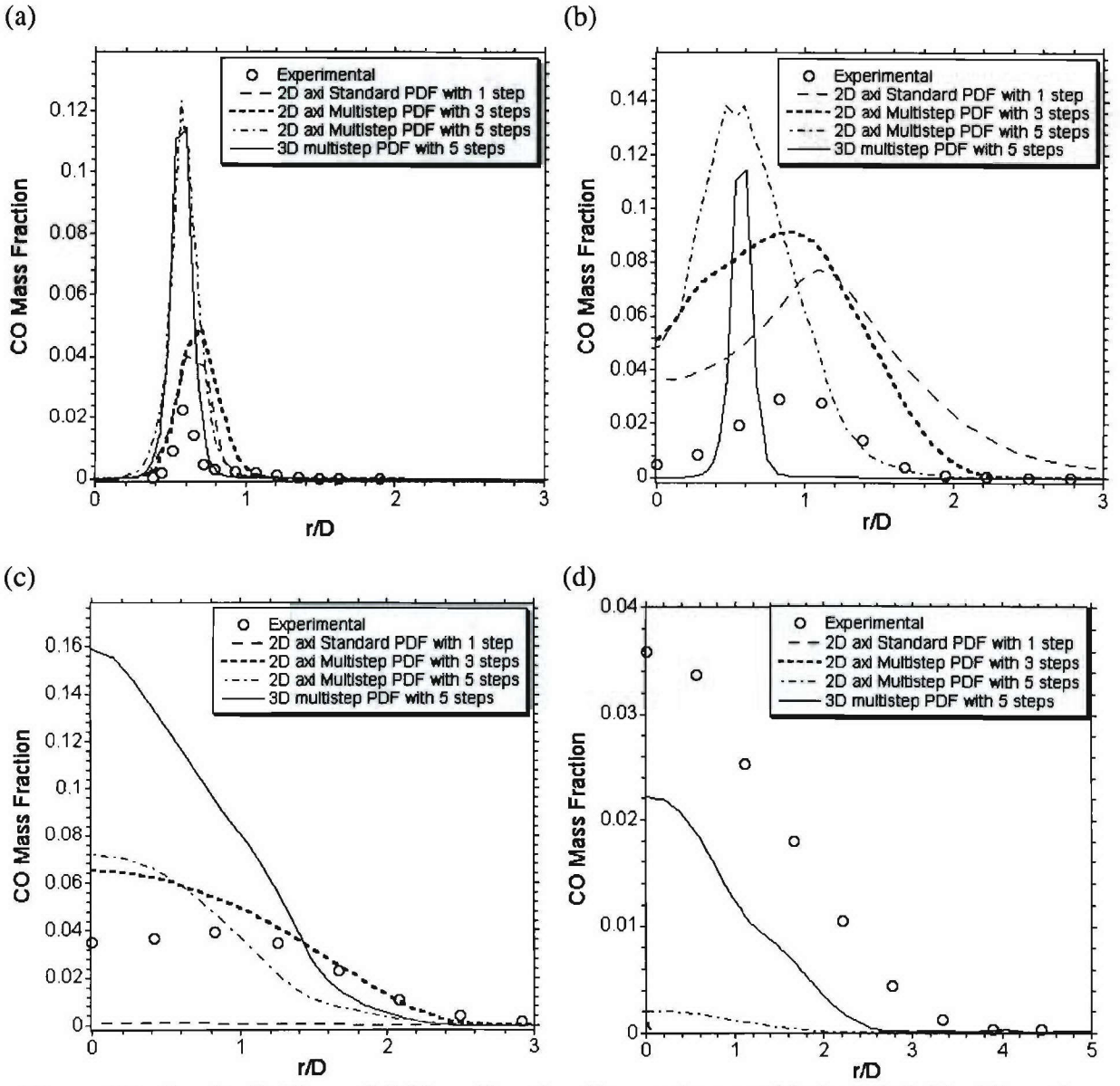

Figure 95. Sandia-D Flame CO Mass Fraction Comparisons at Various Axial (x-) Locations Downstream of the Burner (a) x/d = 1 (b) x/d = 15 (c) x/d = 30 (d) x/d = 45

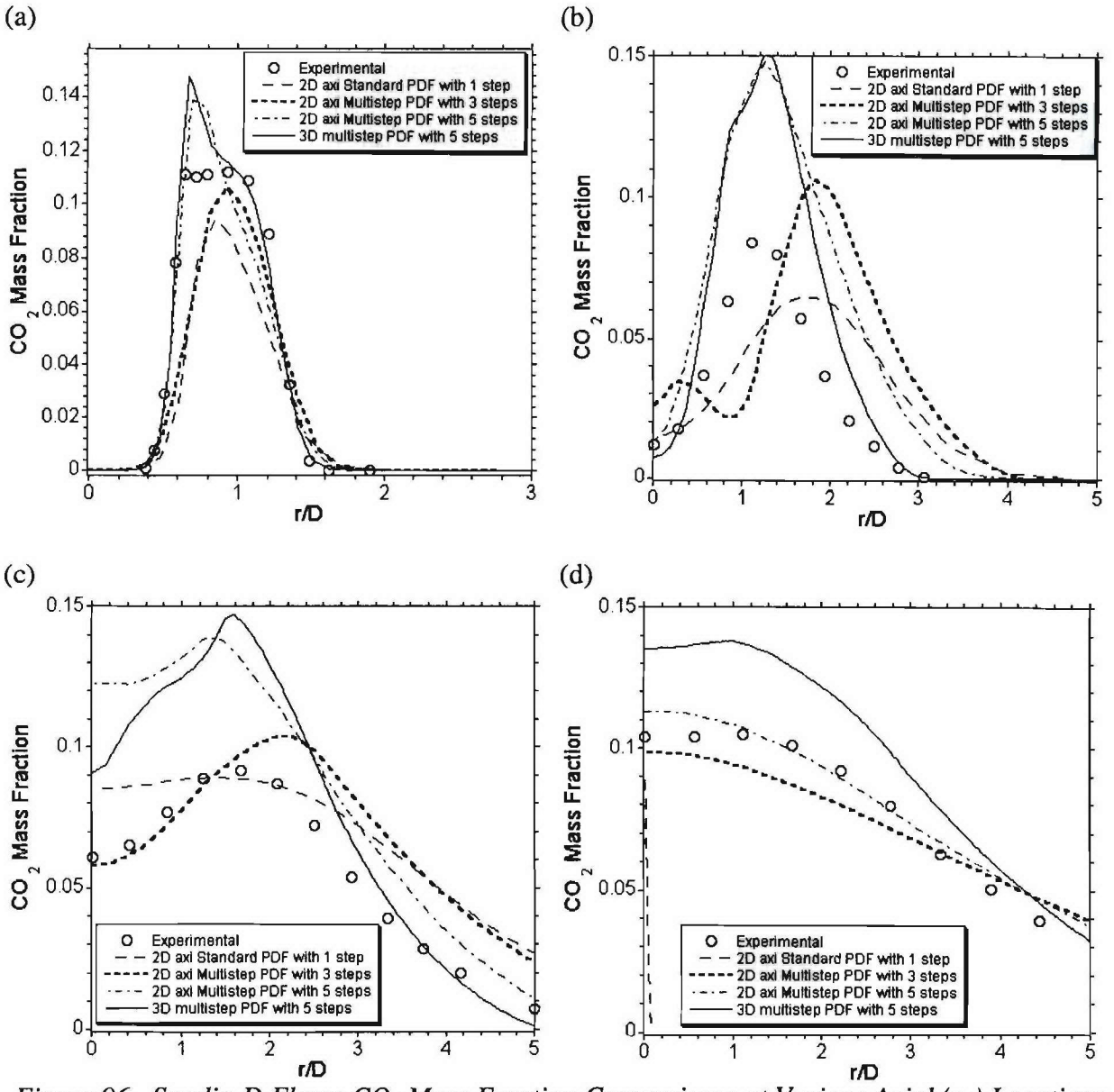

Figure 96. Sandia-D Flame CO_2 Mass Fraction Comparisons at Various Axial (x-) Locations Downstream of the Burner (a) x/d = 1 (b) x/d = 15 (c) x/d = 30 (d) x/d = 45

LES simulations of the Sandia-D flame are currently ongoing, but have not proceeded far enough for a meaningful comparison to the data. Preliminary results from this simulation are shown in Figures 97 through 99. The flame is still significantly longer than what was observed in the RANS simulations, but as the simulations proceeds toward a limit-cycle, the increase in the turbulence will tend to shorten and spread out the flame. Significant vortices are seen developing in the jet, as illustrated by the fluctuations in the radial velocity components.

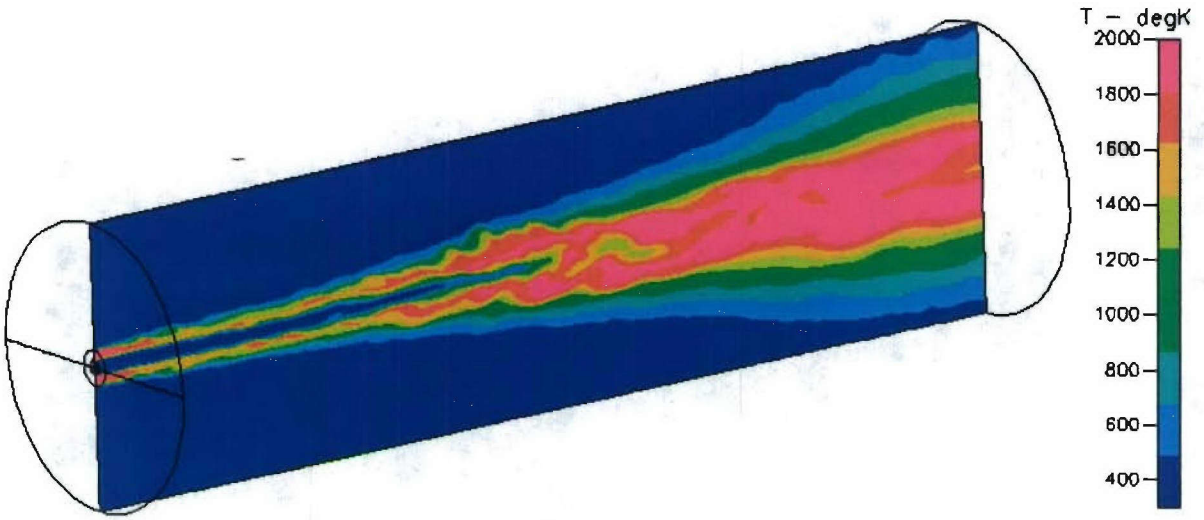

Figure 97. Preliminary Snapshot of Temperature from the Sandia-D LES Combustor Simulations

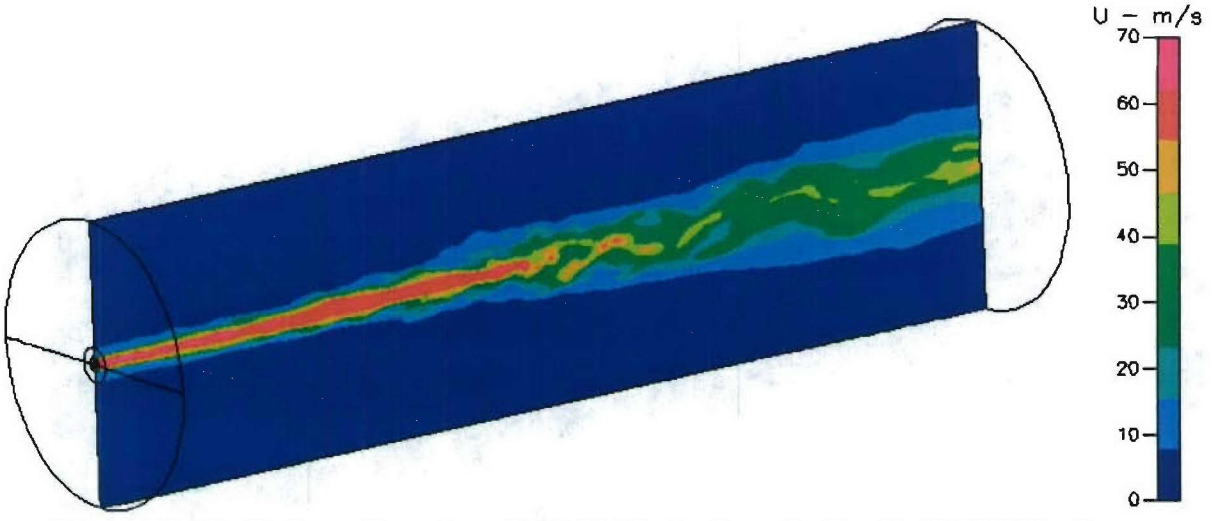

Figure 98. Preliminary Snapshot of Axial Velocity from the Sandia-D LES Combustor Simulations

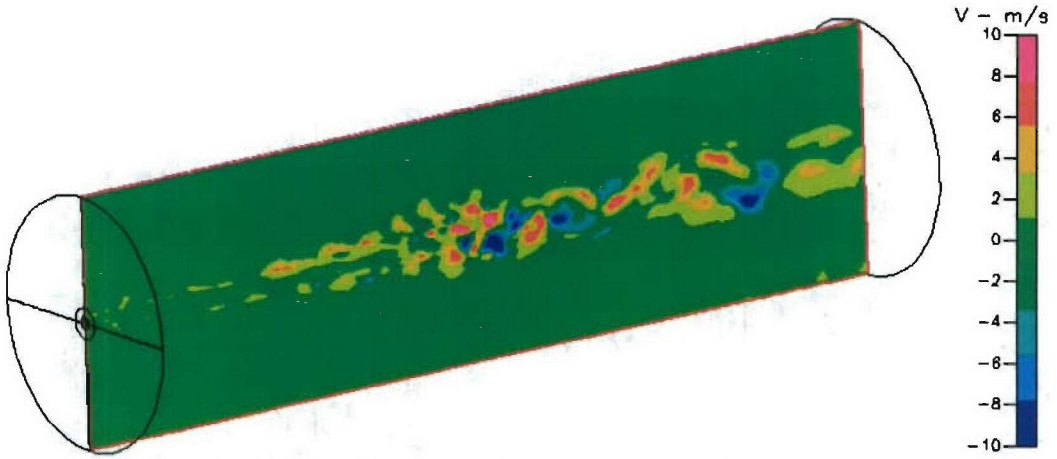

Figure 99. Preliminary Snapshot of Radial Velocity from the Sandia-D LES Combustor Simulations

3.6.4 TECFLAM Combustor – Swirling Diffusion Flame

The fourth validation case selected is the TECFLAM combustor. This case was selected to provide a more in-depth evaluation of the chemistry model for NO_x predictions. The TECFLAM consortium in Germany has collected a comprehensive set of experimental data for a swirl-stabilized combustor for validation of CFD turbulence and chemistry models. The TECFLAM combustor provides detailed measurements on NO_x formation in swirl-stabilized combustors and thus forms a good validation case for turbulence-chemistry interaction models for NOx predictions. A schematic of the TECFLAM combustor is shown in Figure 100.

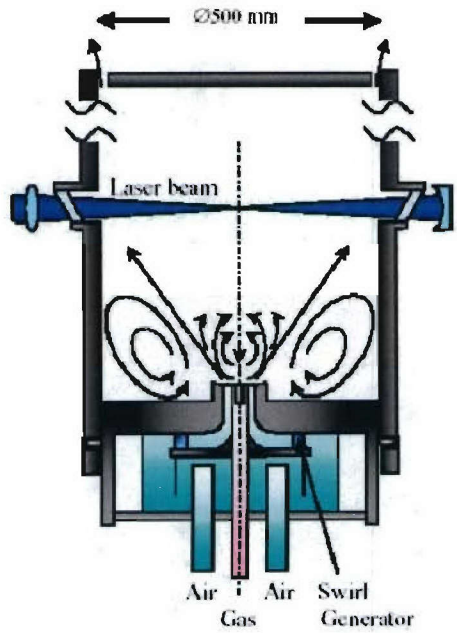

Figure 100. Schematic of the TECFLAM Combustor (Meier et al., 2000)

Natural gas and air are supplied through the annular nozzles. The inside diameter for fuel is 20 mm while the outside diameter is 26 mm. The inside diameter for air is 30 mm while the outside diameter is 60 mm. The fuel contains 96.4-98.2% methane by volume and minor admixtures of nitrogen, carbon dioxide and higher hydrocarbons. The flame has a thermal power of 150 kW, equivalence ratio of 0.833 and a swirl number of 0.9. The Reynolds number at the air inlet is 42,900 while at fuel inlet is 7900. The water cooled-combustion chamber (T_{water_in} = 65°C, T_{water_out} = 75°C) has an inner diameter of 500 mm and an axial length of 1200 mm. Figure 101 shows a picture of the TECFLAM combustor and flame.

Figure 101. TECFLAM Combustor

CFD-Model Description: The experimental data for the TECFLAM case was collected starting from 1mm downstream of the burner exit, thus providing a good boundary condition to start the calculations. Experimental profiles of the axial and tangential velocities were specified at the air inlets, while a bulk velocity of 21 m/s was specified for the fuel inlet. A constant heat flux of 50 kW was specified for the liners. The 3D grid for the CFD calculation is shown in Figure 102.

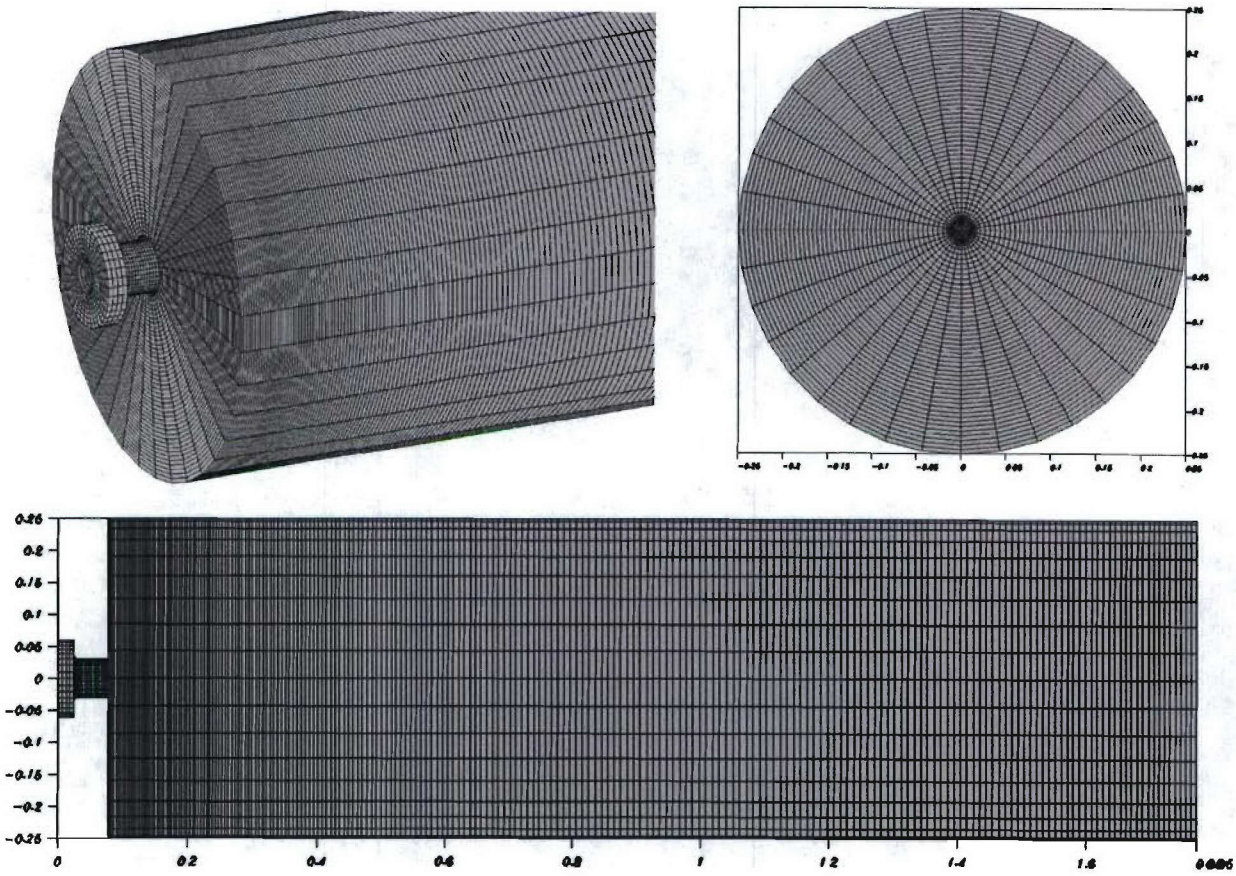

Figure 102. 3D RANS Grid, (a) Top Left: Angled View, (b) Top Right: Side View and (c) Bottom: Front View

CFD Results: The initial RANS predictions with single-step chemistry show decent velocity predictions, but the temperature predictions show a poor match. The lack of appropriate heat flux boundary conditions on the combustor liners is probably responsible for this discrepancy. Figures 103-107 show the results from the 3D reacting steady state RANS simulation. Although the axial velocity shows decent comparison with data at all axial locations compared, the tangential velocity and temperatures are very poorly predicted. RANS simulations are known to perform poorly in predicting the swirl velocity component. The temperature profiles are also mismatched due to the incorrect flow pattern that sets up because of the flow field prediction errors in RANS.

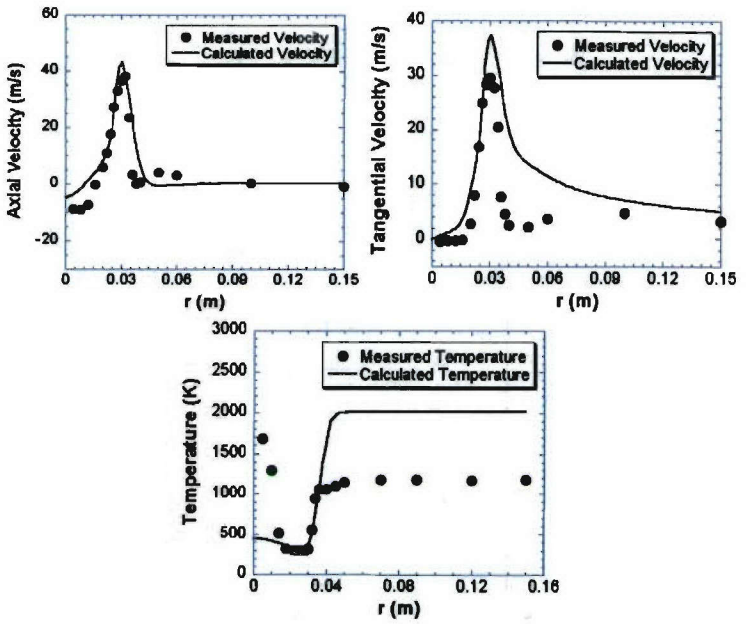

Figure 103. Comparison of 3D RANS with Experimental Data at 10 mm Downstream of the Injector (a) Top Left: Axial Velocity, (b) Top Right: Tangential Velocity, (c) Bottom: Temperature

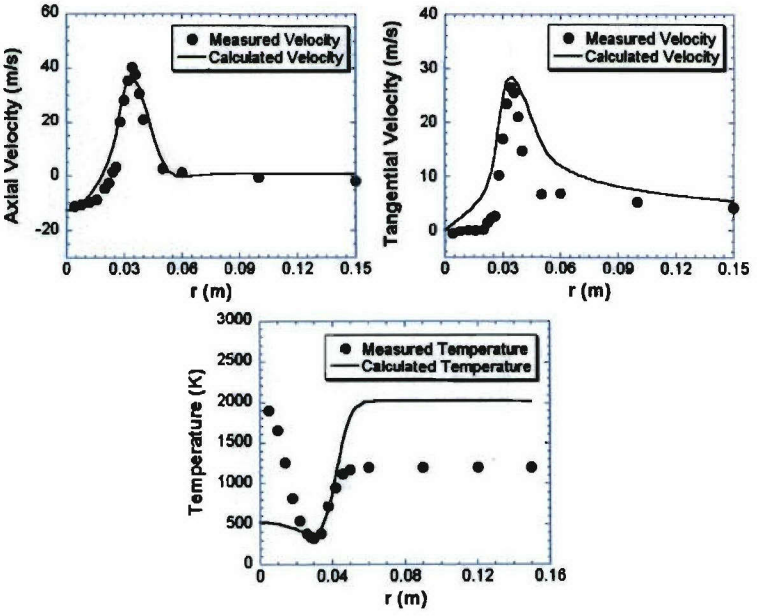

Figure 104. Comparison of 3D RANS with Experimental Data at 20 mm Downstream of the Injector (a) Top Left: Axial Velocity, (b) Top Right: Tangential Velocity, (c) Bottom: Temperature

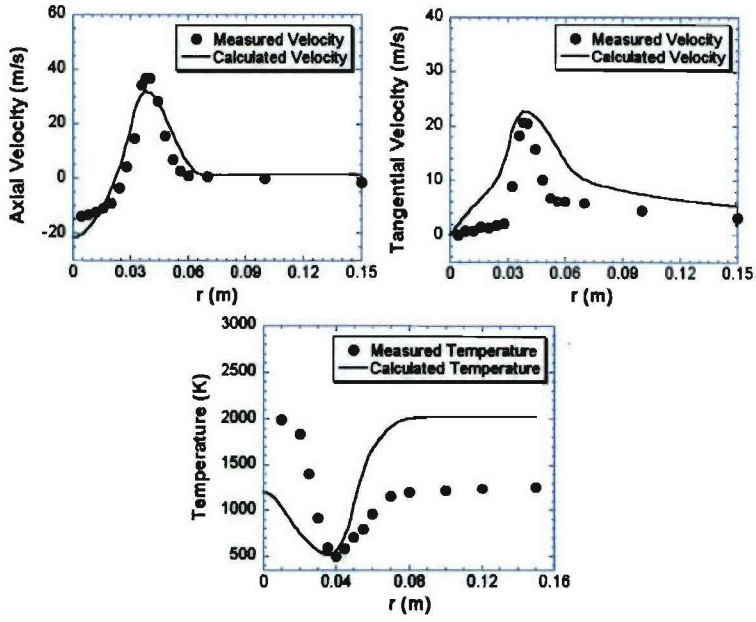

Figure 105. Comparison of 3D RANS with Experimental Data at 30 mm Downstream of the Injector for Velocities and 40mm Downstream for Temperature, (a) Top Left: Axial Velocity, (b) Top Right: Tangential Velocity, (c) Bottom: Temperature

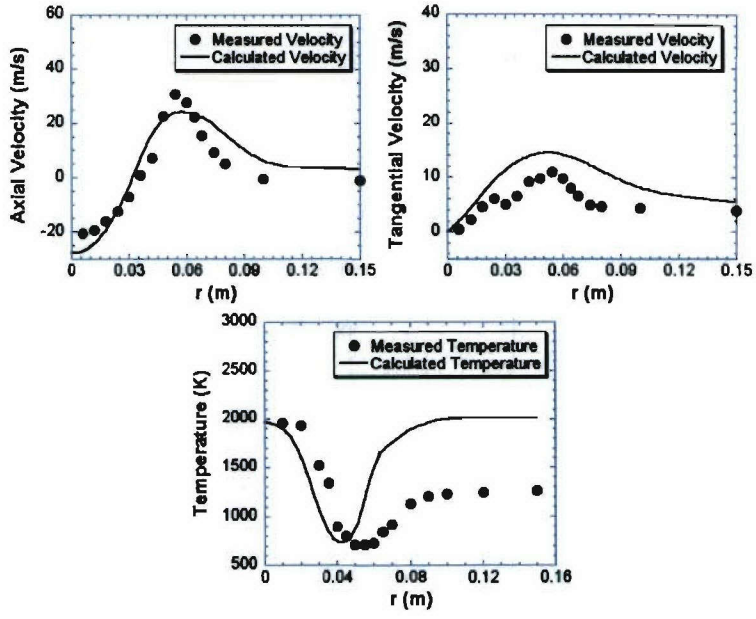

Figure 106. Comparison of 3D RANS with Experimental Data at 70 mm Downstream of the Injector for Velocities and 60mm Downstream for Temperature. (a) Top Left: Axial Velocity, (b) Top Right: Tangential Velocity, (c) Bottom: Temperature

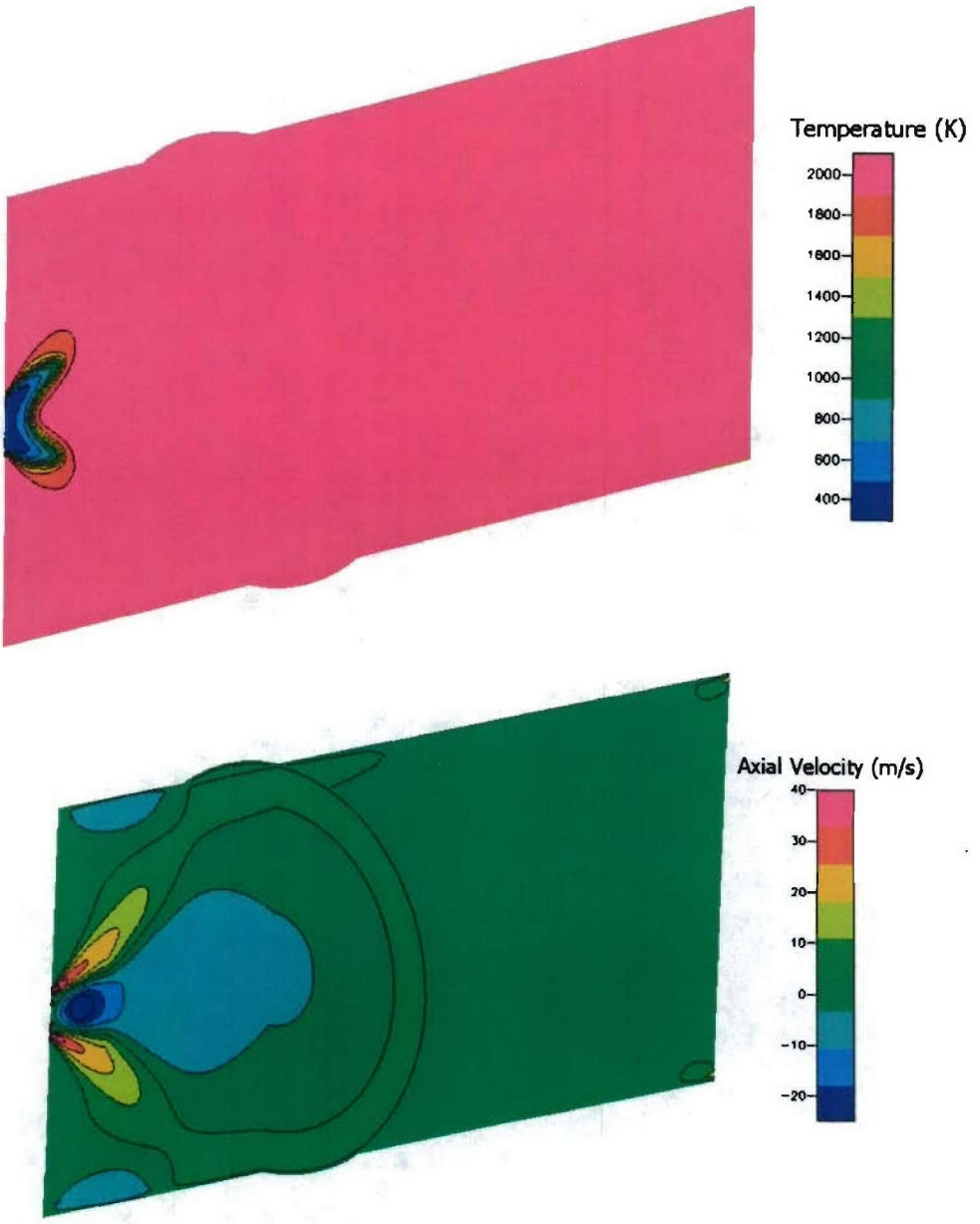

Figure 107. Snapshot of TECFLAM 3D Reacting Flow RANS Simulation

LES is known to capture the swirling flow effects better than RANS. A LES simulation was started in this phase of the program with the flow modeled just downstream of the swirl vane exit. The flow has not progressed far enough to start averaging and only instantaneous results were available. The better prediction of the swirl velocity and the temperature field is already evident from the results shown below. LES captures the much steeper gradients in the tangential velocity much better than RANS. Since the simulation is still in the initial stages, temperatures near the walls are still low in the LES result. Hot products are starting to recirculate upstream, but have not reached the front of the combustor on the centerline and in the outer recirculation zone. Plotted results are shown in Figure 108 through 111, while plots of velocity and temperature are shown in Figure 112.

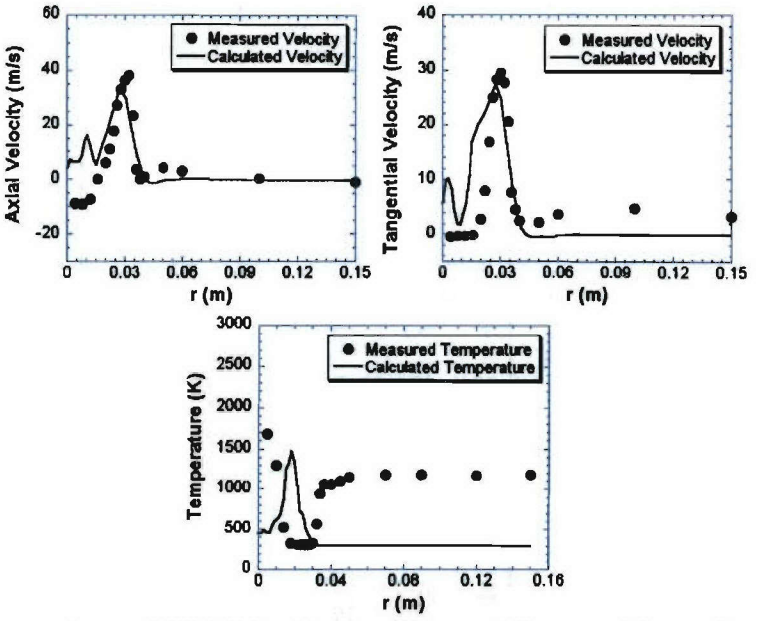

Figure 108. Comparison of 3D LES with Experimental Data at 10 mm Downstream of the Injector. (a) Top Left: Axial Velocity, (b) Top Right: Tangential Velocity, (c) Bottom: Temperature

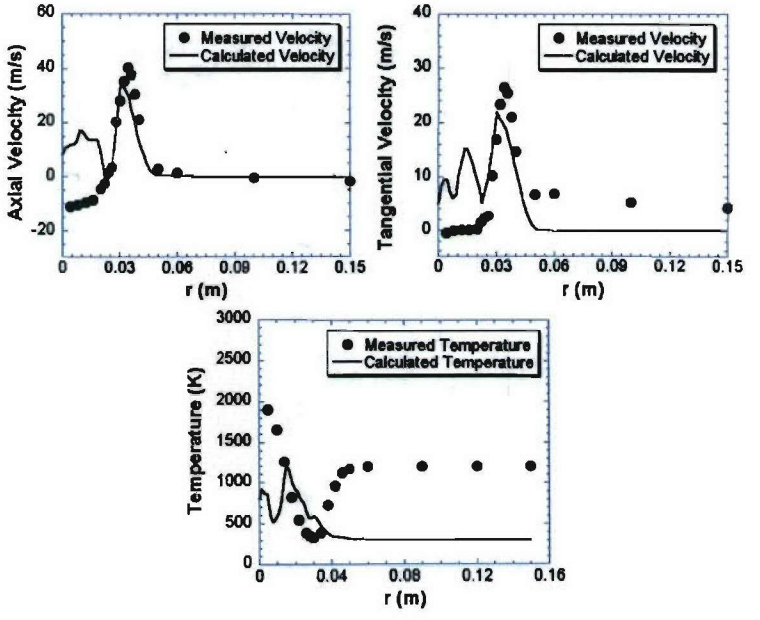

Figure 109. Comparison of 3D LES with Experimental Data at 20 mm Downstream of the Injector. (a) Top Left: Axial Velocity, (b) Top Right: Tangential Velocity, (c) Bottom: Temperature

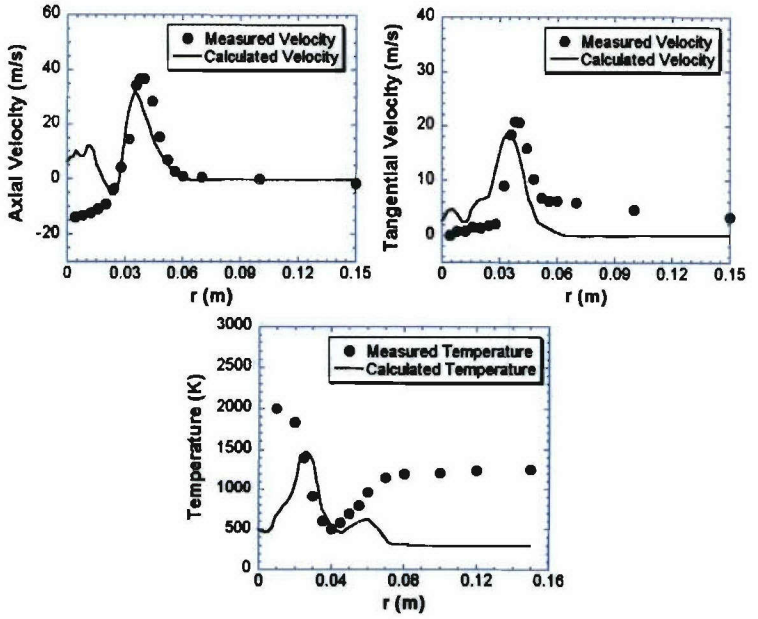

Figure 110. Comparison of 3D LES with Experimental Data at 30 mm Downstream of the Injector for Velocities and 40mm Downstream for Temperature. (a) Top Left: Axial Velocity, (b) Top Right: Tangential Velocity, (c) Bottom: Temperature

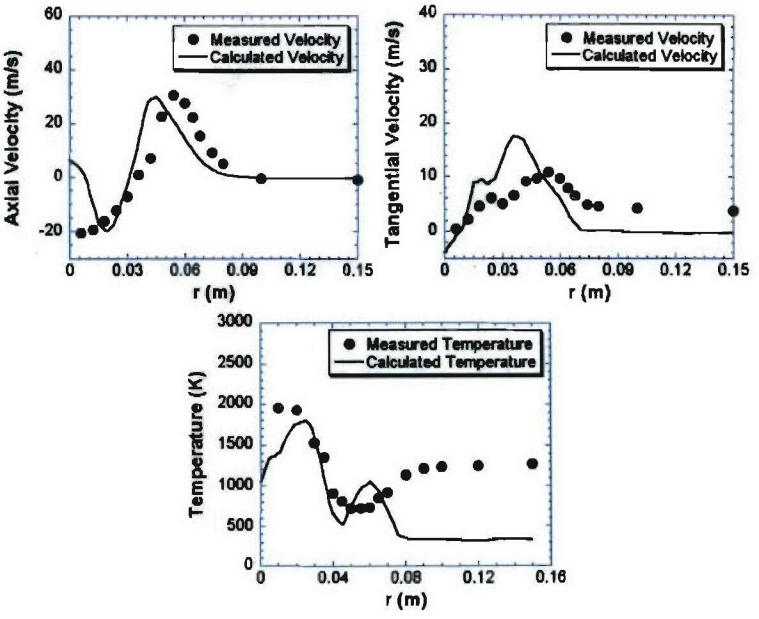

Figure 111. Comparison of 3D LES with Experimental Data at 70 mm Downstream of the Injector for Velocities and 60mm Downstream for Temperature. (a) Top Left: Axial Velocity, (b) Top Right: Tangential Velocity, (c) Bottom: Temperature

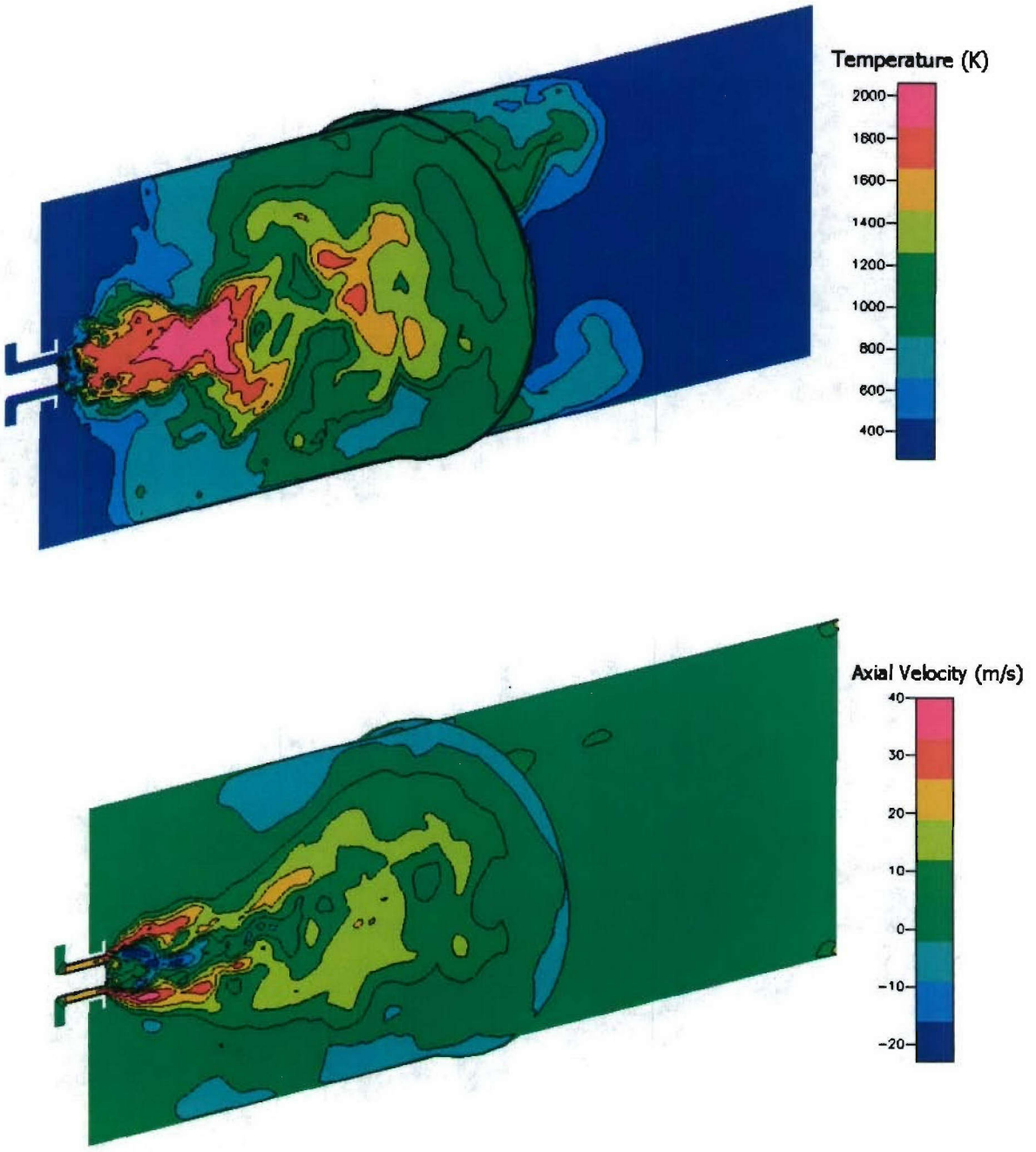

Figure 112. Snapshot of Initial TECFLAM 3D Reacting Flow LES Simulation

The extremely large volume of the combustion chamber resulted in very long computational times. The results shown above took nearly 3 months to run. Therefore, it was decided to postpone work on this case and focus on the other three selected validation cases.

3.7 JSF Combustor Simulations

During the Phase II SBIR program, RANS (Reynolds Averaged Navier Stokes) simulations of the JSF combustor geometry using both single-step and multi-step chemistry were performed. An LES simulation was also completed using single-step kinetics. An LES simulation with multi-step kinetics was started, but due to the slow convergence behavior of the solver, was not completed during the Phase II effort. Given the problem identified with the point solver solution approach in CFD-ACE+, run times with multi-step kinetics are long. A single RANS simulation requires nearly 3 weeks of run time on 16 new computers, while a single LES run would take nearly 4 months. This, and solving problems related to the use of spray with multi-step kinetics severely limited the amount of time available to perform JSF combustor simulations.

Rolls Royce provided the combustor geometry, along with exit profiles of normalized fuel/air ratio. Emissions data at the rig conditions simulated for CO and NO_x were also provided. LES results using single-step kinetics resulted in improved mixing predictions and matched the NO_x data well. CO predictions were high by about an order of magnitude. The exit profile predictions of fuel/air ratio were also improved using LES and matched the data well. RANS results with multi-step kinetics were very similar to those with single-step kinetics. However, CO predictions at the exit were essentially equilibrium, nearly two orders of magnitude less than the measured results. The reasons for this discrepancy are not clear, but could be related to problems with the 3-step mechanism used. The PFR kinetics simulations used to generate the rate profiles may not have been the best choice. It is also unknown how well the detailed mechanism used characterized CO oxidation at the high-pressure conditions of the combustor, since validation data for jet fuels at high-pressure conditions is extremely limited.

Since the details of the JSF combustor simulations are export controlled and Rolls Royce proprietary, they have not been included in this version of the final report. A separate export controlled document containing this data was provided to the project technical monitor along with this final report.

4. CONCLUSIONS

The development of the multi-step PDF model represents a significant improvement in the state-of-the-art for practical turbulent combustion modeling. The model is generally applicable to multi-step global mechanisms and results in a minimal increase in the overall computational expense. Only two additional transport equations must be solved for, regardless of the number of species of steps in the mechanism. The model was successfully tested on a wide range of validation cases. Both lean premixed and diffusion flame cases were tested to showcase the wide applicability of the newly developed turbulent combustion model. Validation cases included bluff body stabilized premixed, jet diffusion, and swirl stabilized diffusion flames. CFD simulations were also performed of the Rolls Royce JSF combustor. Along with the new combustion model, several other key improvements were made to the LES capabilities in CFD-ACE+. A dynamic coefficient approach (LDVM) was developed for the progress and mixture fraction variance equations. Boundary conditions that introduce fluctuations with a prescribed length scale were implemented to get more realistic fluctuations on inlet boundaries for LES calculations.

Although the PDF model was successfully developed and tested, improvements in the solution of the transport equations will be essential for the model to find widespread application. During the development and implementation of the combustion model in CFD-ACE+, a numerical problem was encountered that currently limits the applicability of the new model. This is especially true for transient Large Eddy Simulation (LES). The existing method for solving the species transport equations utilizes a cell-by-cell point solver. Specifically, the solver 'sweeps' over all of the computational cells in the domain solving the coupled species equations at each cell. In a sense, this method holds the solution values at all other cells constant while solving for the species fractions at a given cell. While adequate for small problems, large problems require a large number of iterations in order to assure global convergence. Steady-state problems can usually afford a large number of global iterations to achieve ample convergence. However, transient cases such as LES need to keep the number of global iteration per time step to a minimum if practical run times are to be realized.

The other variables in the CFD calculations are solved for sequentially using a field solution procedure. This method propagates boundary conditions through the solution domain very efficiently and is the standard approach for most CFD calculations. Enthalpy is solved for in this fashion and significant problems have been seen with the coupling of the species (solved for using the point solver) and enthalpy. Adopting this same strategy for the species solution is a plausible approach to achieve good coupling of the enthalpy and species and was tested. In this approach, a given species was solved over the entire computational domain while holding all the other species constant. The remaining species were then solved for in turn in a likewise manner. This procedure has the benefit of fast propagation of boundary information. However, species are highly coupled and exhibit nonlinear behavior and solutions using this methodology rarely converge.

The solution to the problem would be to combine the point solver and the field solver methods. Instead of solving for species 1 while holding species 2, 3, 4, etc. constant, all of the species would be solved simultaneously over the entire field. In the CFD-ACE+ solver, this would necessitate that the field solver handle more than current limitation of solving for only one dependent variable at a time. Using such a coupled field solution, better coupling to other flow variables, such as enthalpy, is possible. This occurs because the species information will propagate at the same rate as the enthalpy information. Also, the species will remain implicitly coupled at each cell. This solution procedure will implicitly will require more CPU time per iteration, but will converge in a fewer number of iterations. However, the implementation and development of this capability is beyond the scope of the present program.

In addition to the development of the new multi-step PDF combustion model, significant work was done on developing the capability to generate the needed multi-step mechanisms. Reduced global mechanisms with Arrhenius rates, suitable for CFD calculations, were generated from detailed mechanisms using a technique typically referred to as Chemical Reactor Modeling (CRM). CRM can be an effective method of determining global Arrhenius rate parameters. Several examples were shown, demonstrating the flexibility in this approach with regard to the number of species and the number of steps to be included in the global mechanism. The global mechanism can be fine tuned to combustor operating conditions including inlet temperature,

equivalence ratio range, and operating pressure. Also, by using multi-step global mechanisms, multi-step processes can be captured that can't be with single step kinetics. For example, multi-step kinetics can more accurately capture the conversion of CH_4 to CO and then to CO_2.

There still exist some drawbacks to the current approach for determining global rate parameters. For diffusion flame models, implementation of global mechanisms determined from CRM can be tricky because rate parameters were not curve fit for the entire range of equivalence ratios encountered. Extrapolation outside of the bounds where the rate parameters were fit, or application of the rates at conditions not considered in generated in the global rates can result in significant errors. Also, the species profiles should be included in the optimization process instead of solely relying on the temperature profile or the species net production rates (which have not proven very effective). Weighting factors should be applied to allow the user to specify different emphasis on temperature or certain species profiles. Although mechanism generation can easily be done with the tools developed, generating a mechanism that behaves realistically over a broad range of conditions and that accurately mimics the broad range of flame properties necessary (ignition delay, extinction limits, etc.) has proven very challenging and significant research in this area is still needed.

5. REFERENCES

Akhiezer, N. I., "The Classical Moment Problem," Hafner Publishing Co., New York, 1965.

Balay, S., Buschelman, K., Gropp, W. D., Kaushik, D., Knepley, M., McInnes, L. C., Smith, B. F., and Zhang, H., http://www.mcs.anl.gov/petsc, 2001.

Black, D.L., Zuo, B.F., and Smith, C.E., (2003), "Improved Turbulent-Combustion CFD Modeling for High Fuel-Air Ratio Combustor Analysis;" Final Report; CFDRC Project No.: 8496.

Bohn, E.E. and Lepers, J., (1999), "Numerical Simulation of Turbulent Premixed Combustion Using a Joint-PDF Approach Based on a Systematically Reduced Multi-Step Reaction Mechanism," ASME Paper No. 99-GT-272, presented at the International Gas Turbine and Aeroengine Congress and Exhibition, Indianapolis, IN.

Cannon, S.M., Brewster, B.S., and Smoot, L.D., (1999), "PDF Modeling of Lean Premixed Combustion Using In Situ Tabulated Chemistry," *Combustion and Flame*, Vol. 119, pp. 233-252.

Chakravarthy, V.K. and Menon, S., 1999, "Large-Eddy Simulations of Turbulent Premixed Flames in the Flamelet Regime," *Combustion Science and Technology*, Volume 162, pp. 175-222.

Chen, J.-Y., (1997), "Numerical Aspects of Reduction in Chemical Kinetics," CERMICS-ENPC Cite Descartes-Champus sur Marne, France.

Cook, A. W. and Riley, J. J., (1994), "A Subgrid Model for Equilibrium Chemistry in Turbulent Flows," Phys. Fluids 6, 2868-2870.

Chen, J.-Y. (1988), "A General Procedure for Constructing Reduced Reaction Mechanisms with Given Independent Relations," Combustion Science and Technology, Vol. 57, pp. 89-94.

Chen, J.-Y., (1997), "Numerical Aspects of Reduction in Chemical Kinetics," CERMICS-ENPC Cite Descartes-Champus sur Marne, France.

Dagaut, P. Reuillon, M., Boettner, J.-C. and Cathonnet, M., (1994), "Kerosene Combustion at Pressures Up to 40 atm: Experimental Study and Detailed Chemical Kinetic Modeling," *Proceedings of the Combustion Institute*, Vol. 25, pp. 919-926.

Dryer, F.L. and Glassman, I., (1973), *Fourteenth Symposium (International) on Combustion*, The Combustion Institute, Pittsburgh, PA, pp. 987.

Dupont, V., Pourkashanian, M., and Williams, A., (1993), "Modelling Natural Gas Fired Process Heaters," Journ. of the Inst. of Energy. Vol. 66, pp. 20-28.

Girimaji, S. S. and Zhou Y., (1996), "Analysis and Modeling of Subgrid Scalar Mixing Using Numerical Data," Phys. Fluids 8, 1224-1236.

Goodwin, D., http://rayleigh.cds.caltech.edu/~goodwin/cantera/index.html, June 14, 2004.

Goodwin, D., www.cantera.org, June, 2005.

Guo, Y.-H., He, G.-B., Hsu, A. T., Brankovic, A., Syed, S. and Liu, N.-S., "The Development of a Variable Schmidt Number Model for Jet-in-Crossflows Using Genetic Algorithms," 37th AIAA Aerospace Sciences Meeting and Exhibit, Jan. 11-14, 1999, Reno, NV.

Jones, W.P., and Lindstedt, R.P., (1988), *Combustion and Flame*, Vol. 73, pp. 233.

Kerstein, A.R., (1992), "Linear-Eddy Modelling of Turbulent Transport. Part 7. Finite-Rate Chemistry and Multi-Stream Mixing," *Journal of Fluid Mechanics*, Vol. 240, pp. 289-313.

Kim, W. and Menon, S., (1997), "Application of the Localized Dynamic Subgrid-Scale Model to Turbulent Wall-Bounded Flows," AIAA paper 97-0210.

Klein, M., Sadiki, A., Janicka, J., (2003), "A Digital Filter Based Generation of Inflow Data for Spatially Developing Direct Numerical or Large Eddy Simulations," *Journal of Computational Physics*, Vol. 186, pp. 652-665.

Libby, P. A. and William, F. A., (2000), "A Presumed PDF Analysis of Partially Premixed Turbulent Combustion," Combustion Science and Technology, Vol. 161, pp. 351-390.

Masri, A. R. And Pope, S. B., "PDF Calculations of Piloted Turbulent Nonpremixed Flames of Methane," Combustion and Flame 81: 13-29 (1990).

Mawid, M.A., Park, T.W., Sekar, B., and Arana, C., (2002) "Development and Validation of a Detailed JP8 Fuel Chemistry Mechanisms," AIAA 2002-3876, 38th AIAA/ASME/SAE/ASEE Joint Propulsion Conference and Exhibit, Indianapolis, IN.

Menon, S. and Calhoon, W., 1996, "Subgrid Mixing and Molecular Transport Modeling for Large-Eddy Simulations of Turbulent Reacting Flows," *Proceedings of the Combustion Institute*, Volume 26, pp. 59-66.

Moreau, P. and Boutier, A., 'Laser Velocimeter Measurements in a Turbulent Flame,' 16th Symposium (int.) on Combustion, 1976.

Nandula, S.P., Pitz, R.W., Barlow, R.S., and Fiechtner, G.J., (1996), "Rayleigh/Raman/LIF Measurements in a Turbulent Lean Premixed Combustor," AIAA 96-0937, 34th Aerospace Sciences Meeting and Exhibit, Reno, NV, January 15-18, 1996.

Nicol, D. G., "A Chemical Kinetic and Numerical Study of NO_x and Pollutant Formation in Low-Emission Combustion," Ph.D. Dissertation, University of Washington, 1995.

Nicol, D. G., and Malte, P. C., "A Five-Step Global Mechanism for Methane Oxidation with NO Formation For Lean-Premixed Combustion: Development of the Mechanism and Application to a Gas Turbine Combustor," WSS/CI 97S-039.

Nicol, D. G., Malte, P. C., Hamer, A., Roby, R. J., Steele, R. C., "A Five-Step Global Mechanism for Methane Oxidation with NO Formation for Lean-Premixed Combustion: Development of the Mechanism and Application to a Gas Turbine Combustor," Wss/CI 97S-039 (1997).

Pan, J.C., Vangsness, M.D., Henegham, S.P., Schmoll, W.J., and Ballal, D.R., (1991), "Laser Diagnostic Studies of Confined Turbulent Premixed Flames Stabilized by Conical Bluff Bodies: Data Set," University of Dayton, Rept. UDR-TR-91-102.

Peters, N., (1999), "Turbulent Combustion," Cambridge University Press, Cambridge.

Pierce, C. D. and Moin, P., (1998), "A Dynamic Model for Subgrid-Scale Variance and Dissipation rate of a Conserved Scalar," Phys. Fluids 10, 3041-3044.

Pope, S.B., (1997), "Computationally Efficient Implementation of Combustion Chemistry Using In Situ Adaptive Tabulation," *Combustion Theory and Modeling*, Vol. 1, pp. 41-63.

Schlüter, J.U., (2002), "Consistent Boundary Conditions for Integrated LES/RANS Simulations: LES Inflow Conditions," *Center for Turbulence Research Annual Research Briefs*.

Turns, S. R., An Introduction to Combustion: Concepts and Applications, McGraw Hill, 2000, pp. 205.

Violi, A., Yan, S., Eddings, E.G., Sarofim, A.F., Granata, S., Faravelli, T., and Ranzi, E., "Experimental Formulation and Kinetic Model for JP-8 Surrogate Mixtures", Combustion Science & Technology, 174(11-12), 399-417 (2002).

Weiss, J. M., "Calculation of Reacting Flowfields Involving Stiff Chemical Kinetics," AIAA-99-3369 (1999).

Westbrook, C.K., and Dryer, F.L., (1984), *Prog. In Energy and Combust. Science*, Vol. 10.

Zuo, B. F., Van den Bulck, E., (1998), "The Modeling, Scales and NO_x Characteristics of the Pre-Vaporized, Premixed Fuel Oil Burner Combustion," *Combustion Science and Technology*, Vol. 137, Number (1-6), pp. 149-170.

Zuo, B.F., Cannon, S.M., Smith, C.E., (2003), "A Linear Eddy Subgrid Les Combustion Model for Turbulent Reacting Flows," GT2003-38200, to be presented at ASME Gas Turbine Expo, Atlanta, GA, June 2003.

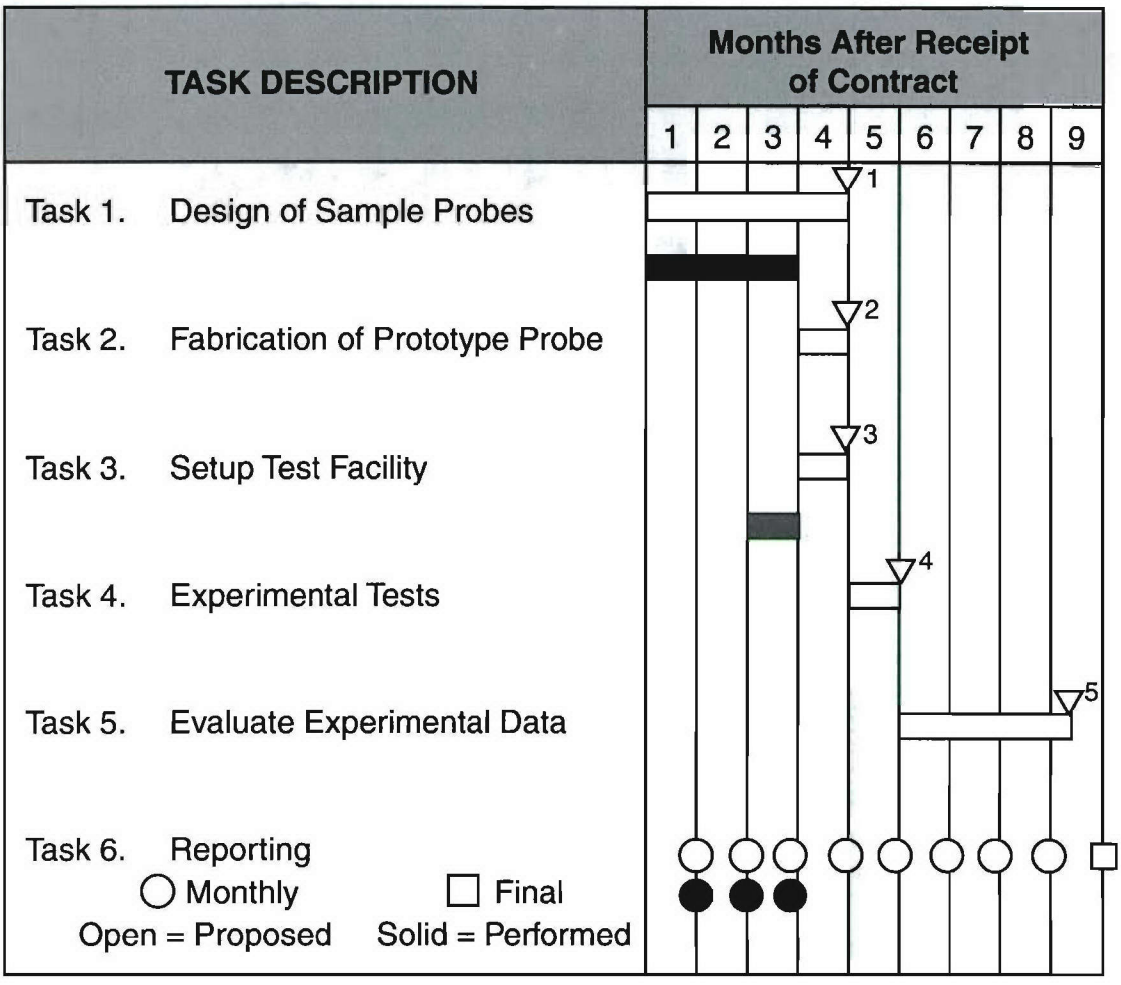

Milestones:

1. Design of Probes Completed
2. Fabrication of Probes Completed
3. Test Facility Setup Completed
4. Experimental Test Completed
5. Data Evaluation Completed